Ore Geology Reviews 91 (2017) 335–386

Contents lists available at ScienceDirect

Ore Geology Reviews

journal homepage: www.elsevier.com/locate/oregeorev

Urucum Neoproterozoic–Cambrian manganese deposits (MS, Brazil): Biogenic participation in the ore genesis, geology, geochemistry, and depositional environment

João Carlos Biondi[a,*], Michel Lopez[b]

[a] Federal University of Paraná State, Polytechnic Center, Geology Department, 81531-980 Curitiba, Brazil
[b] University of Montpellier 2, Geosciences of Montpellier, cc. 060, 34095 Montpellier, cedex 5, France

ARTICLE INFO

Keywords:
Neoproterozoic–Cambrian manganese deposits
Urucum (Brazil)
Jacadigo Group
Biogenic mediation
Depositional environment

ABSTRACT

The Urucum region (Mato Grosso do Sul, Brazil) contains Neoproterozoic–Cambrian manganese ore in the layers Mn-1, Mn-2, and Mn-3, which are interbedded with iron formations (IFs) from the Santa Cruz Formation (Jacadigo Group) and surrounded by carbonate rocks from the Bocaina and Tamengo Formations (Corumbá Group). These rocks fill an ancient graben, with sediments from the Santa Cruz Formation overlying fluvial deposits from the Urucum Formation and limestones from the Bocaina and Tamengo Formations deposited in the shallow marginal regions. As the graben deepened, it was flooded with microbe-rich seawater and hydrothermalism began. Iron and manganese precipitated within the pores in arkosic sandstones, thereby forming the clastic Lower Mn-1 ore layer. The remaining manganese was simultaneously deposited on the basin floor with clastic clay and silt from turbidity currents, thereby forming the Upper Mn-1 clastic–chemical ore layer. The sedimentation of Mn-1 and its host IFs was controlled by seawater saturation and homogeneous oxidation, which caused manganese and iron sedimentation and the death of microorganisms, generating mangano-ferriferous sediments with high P, Co and Ni contents. Mn-2 formed during periods of tectonic quiescence through water influxes that carried abundant microbes, Fe(II), Mn(II), and SiO_2. Under UV radiation, these microbes oxidized Mn(II) and Fe(II) to form hydroxides and died, thereby forming biomass that was enriched in P, Co and Ni and minor carbonate adjacent to and below the oxycline. These microbes also formed kremydilites, oblate structures that resemble manganese stromatolites, within the biomass and produced CH_4 and/or H_2 gas bubbles. During early diagenesis, wormlike organisms inhabited the biomass and probably separated iron from manganese to produce cryptomelane microbialites, which agglutinated to form manganese micronodules that coalesced to form the massive layer Mn-2. This process ended with the disappearance of microorganisms and the sedimentation of the IFs, and a new water influx generated layer Mn-3 via the same process. The final seawater upwelling precipitated IFs in the basin depocenter, whereas limestone from the Tamengo Formation was deposited along the basin's edges. The diagenesis initially transformed the manganese oxides into cryptomelane and then into hollandite.

1. Introduction

The Urucum mining district occupies an area of approximately 800 km^2 and is located in the Pantanal region of southwestern Brazil, where manganese and iron deposits have been known since 1894 (Evans, 1894). These deposits cover flat-topped elevations with altitudes slightly greater than 1000 m above sea level and approximately 850 m above the wetlands of the Pantanal. Layers of massive manganese oxides, interspersed with iron-rich chert, banded iron formations (BIFs), and massive ironstones, constitute the Santa Cruz Formation of the Jacadigo Group, totaling up to 290 m in thickness. Urban et al. (1992) estimated that the Urucum district contains more than 600 Mt of rock with high manganese content and approximately 36 Bt of iron-formations. The average contents cited by Urban et al. (1992) are: Mn-1 = 27.14% Mn and 12.85% Fe; Mn-2 = 42.44% Mn and 16.33% Fe; Mn-3a = 44.09% Mn and 15.42% Fe; Mn-3b = 31.42% Mn and 29.70% Fe; Mn-4 = 45.46% Mn and 13.48% Fe; and 58.02% Fe. As summarized by Walde and Hagemann (2007), the proposed genetic models for these rocks include (a) marine genesis, with sediments of continental origin (Door, 1945); (b) marine genesis, with sediments of marine origin (Almeida, 1946; Putzer, 1958; Haralyi, 1972); (c) volcanogenic marine genesis (Walde, 1981; Walde et al., 1981; Leonardos and Walde, 1982;

* Corresponding author.
E-mail address: biondiufpr@gmail.com (J.C. Biondi).

http://dx.doi.org/10.1016/j.oregeorev.2017.09.018
Received 27 February 2017; Received in revised form 18 September 2017; Accepted 27 September 2017
Available online 04 October 2017

O'Connor and Walde, 1985); (d) genesis in a glacial marine sedimentary environment followed by supergene enrichment (Schneider, 1984; Schreck, 1984; van Leeuwen and Graaf, 1987; Graf et al., 1994; Costa et al., 2005); (e) sedimentary genesis that occurred in a flooded graben with a contribution of hydrothermal leaching from hidden mafic rocks (Haralyi and Wald, 1986; Walde, 1988; Trompette et al., 1998); (f) SEDEX, or sedimentary exhalation (Dardenne, 1998); and (g) sedimentary genesis in an oceanic environment with a deep-sea hydrothermal contribution (Klein and Ladeira, 2004). Recently, Angerer et al. (2016) proposed a biogenic origin, in a glacio-marine environment, for the carbonate BIFs of the Santa Cruz Mine region located on the southeastern part of Santa Cruz plateau.

This study presents evidence for local submarine hydrothermal exhalation and biogenic marine mediation in the genesis of the massive, manganese ore layers in the Urucum region, based on field work, construction of stratigraphic columns for the various areas where manganese layers occur, new geochemical analyses (oxides, trace elements, and REEs) for all of the manganese ore types, and detailed scanning electron microscopy with energy-dispersive X-ray spectroscopy (SEM − EDS) microanalysis of ore samples. When relevant to discuss the genesis of manganese ore layers, new data regarding iron formations hosting manganese layers is presented. Using all these data, we propose a new genetic model for the Urucum manganese ores that includes the micro-organisms-mediation during sedimentation and diagenesis of free-carbon-rich manganiferous sediments mixed with iron hydroxides. This work is important because: (a) it presents direct evidence for the action of microorganisms in a Neoproterozoic environment during the genesis of manganese deposits related to BIFs; (b) it explains the role of these microorganisms in the genesis of the Urucum manganese deposits; (c) it describes the features, such as kremydilites and microbialites, generated by these microorganisms; and (d) for the first time, it presents direct evidence for gas production during the genesis of manganese sediments in a Neoproterozoic–Cambrian environment.

2. Geological context

The basement of the Urucum region consists essentially of hornblende–biotite granites and granodiorites. Where the granites are cut by faults they are hydrothermally altered, becoming greenish in color due to the presence of chlorite, sericite, and epidote, and ferruginous jasper infills some fractures (this work and Freitas et al., 2011). Rocks belonging to the Jacadigo Group, which comprises the Urucum and Santa Cruz formations, and the Corumbá Group, which comprises the Bocaina and Tamengo formations, overlie the basement rocks. The carbonate rocks of the Corumbá Group are exposed surrounding the plateaus formed by the iron- and manganese-bearing units of the Jacadigo Group (Fig. 1).

The Urucum Formation consists of feldspathic sandstones, locally cemented by carbonate, and conglomerates with minor siliceous shales and dolomites. The conglomerates and arkosic sandstones display channel cross-stratification and contain ferruginous, laminated, and lenticular sandstones; together, these layers total a few tens of meters in thickness (Fig. 2). These rocks are continental fanglomerates, debris-flow conglomerates, and coarse channel-fill sandstones (Fig. 2B–C). As in the granite basement, the fanglomerates locally contain ferruginous jasper infilling fractures.

Above the Urucum Formation, the Santa Cruz Formation is mainly composed of banded iron formations (BIFs), iron formations (IFs), massive and banded jasper with occurrences of *Corumbella werneri* fossil (Figs. 2–4), and ferruginous arkosic sandstones. Massive manganese layers, named Mn-1, Mn-2, and Mn-3, occur in the lower half of this formation, interlayered with BIFs and massive jasper. As previously described by Urban et al. (1992), a transition between the Urucum and Santa Cruz formations through the Mn-1 horizon was observed in all mines where Mn-1 was mined (Fig. 5). New data show that the Santa Cruz Formation in the Figueirinha and São Domingo mines (Fig. 3), adjacent to and below Mn-1, comprises arkosic sandstones and conglomerate consisting of rounded fragments of granite, hematite, and chert cemented by silica, jasper, and hematite (Fig. 3B). Locally, at the Figueirinha Mine, this conglomerate contains a carbonate boulder with stromatolites (Figs. 3B and 4A). Above these clastic, ferruginous rocks, there are typically two or more layers of Mn-1 manganese ore with meter- to decimeter-scale thicknesses, locally interlayered with clasts rich in jaspillite. In these mines, the Lower Mn-1 ore layer is sandy with detrital braunite + cryptomelane cement ± Mn–Fe-rich carbonate (Table 1, Figueirinha Mine), and the Upper Mn-1 layer is a microgranular, massive, clastic–chemical layer of manganese oxides with undulating parallel lamination (Fig. 6B) and numerous decimeter-scale oblate structures characterized by a massive core and silty clay wrap. These structures (Fig. 6C), which contain nuclei composed of manganese or iron oxides (light gray color in Fig. 6C), are present in all of the Urucum iron and manganese ores and will be referred to as amygdalites (from the Greek αμύγδαλο = amygdale or almond). The ore layer is bounded by sharp planar contacts and is typically overlain by conglomerate consisting of angular granite pebbles and an arkosic matrix (Fig. 6A). In the Figueirinha Mine, the mineralized horizon contains remnant sedimentary structures, which are generally characterized by fluvial channel cross-stratification (Fig. 6D), and layers showing gradational granulometric variations. In the Laginha, Rabicho, Tromba dos Macacos, Morro Grande, and Jacadigo mines (Fig. 3), the Mn-1 horizon contains arkosic sandstone and conglomerates with ferruginous matrix together with several decimeter-thick layers of detrital manganese oxide ore. Locally, these rocks are fractured and contain abundant concretionary and disseminated manganese oxides (Fig. 6E–F).

Above the Mn-1 horizon, massive manganese ore layers, designated Mn-2 and Mn-3 (Figs. 2–3), are interbedded with BIFs, ironstone, and massive jasper, locally with occurrences of *Corumbella werneri* (Figs. 2B and 4B–D), and overlain by BIFs, ferruginous arkose, and ironstones. Between the Mn-1, Mn-2, and Mn-3 layers, and in the upper half of the Santa Cruz Formation, there are BIFs, hematite chert, and massive IFs, with several interbedded lenses showing channel geometries and composed of ferruginous feldspathic sandstones and conglomerates. Three types of BIFs were described (Fig. 2): (a) Peloidal, stratified BIF (Fig. 13A), composed of massive red chert with intercalations of nodules and/or peloids of chert and lenses of ferroan carbonate; (b) Laminated BIF, formed by narrow bands of hematite and chert, with approximately the same widths and; (c) Banded BIF, characterized by thick layers of massive hematite interbedded with narrow layers of chert, as will be shown later in Fig. 13C. Layers Mn-2 and Mn-3 are exposed only on the Santa Cruz, Urucum, and Tromba dos Macacos plateaus. They are typically hosted between the arkosic sandstones with ferruginous matrix (Fig. 6A and G–K) and are locally overlain by conglomerate with granite pebbles, which also contains an arkosic ferruginous matrix. Layers Mn-2 and Mn-3 contain metallic manganese ore, and are massive or laminated, cryptocrystalline, and very hard, commonly containing amygdalites. However, the predominant structures are oblate, centimeter- to decimeter-scale, concentrically zoned structures, with porous manganese oxides in the core and several layers of micronodular cryptomelane ± Mn carbonate surrounding the core (Figs. 7 and 8A–B). These structures will be referred to as kremydilites (from the Greek κρεμμύδι or kremmýdi = onion) and will be described and discussed in detail later. Unlike the amygdalites, the kremydilites occur only in layers Mn-2 and Mn-3.

The vertical distance between layers Mn-1 and Mn-2 is almost constant, at approximately 70 m (Fig. 5), and the vertical distance between layers Mn-2 and Mn-3 varies little, between 40 and 45 meters. Layer Mn-4 (Urban et al., 1992), which is lenticular and discontinuous, was entirely mined, leaving only a few ore blocks with characteristics similar to the ore in layers Mn-2 and Mn-3.

In the Corumbá Group, the Bocaina Formation (Gaucher et al.,

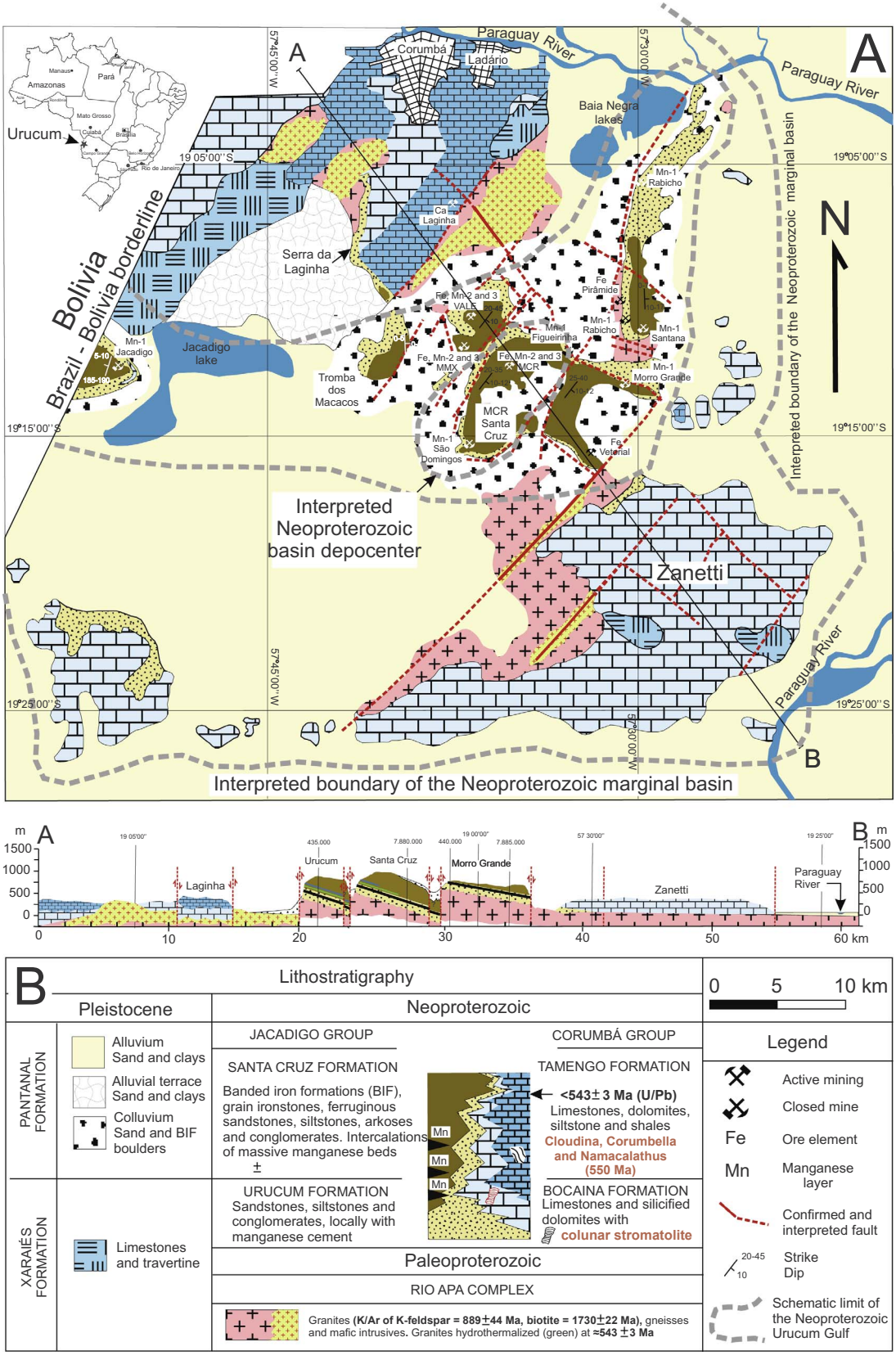

Fig. 1. (A) Geological map (modified from Urban et al., 1992) and geological cross-section. (B) Lithostratigraphy of the Urucum mining region (Corumbá, MS, Brazil). Lines with an interpretation of the probable relative depth of the depocenter of the Urucum marginal basin, and the regional distribution of hydrothermalized granites, were added to the map.

2003; Boggiani et al., 2010) consists of siliceous limestones and dolomites with numerous interbedded intraformational conglomerates. The Tamengo Formation contains limestones, dolomites, shales, and siltstones with lenses of polymictic conglomerates containing carbonate and granite pebbles. Dolomites with columnar stromatolites are typical of the Bocaina Formation, and *Corumbella werneri* and *Cloudina lucianoi*

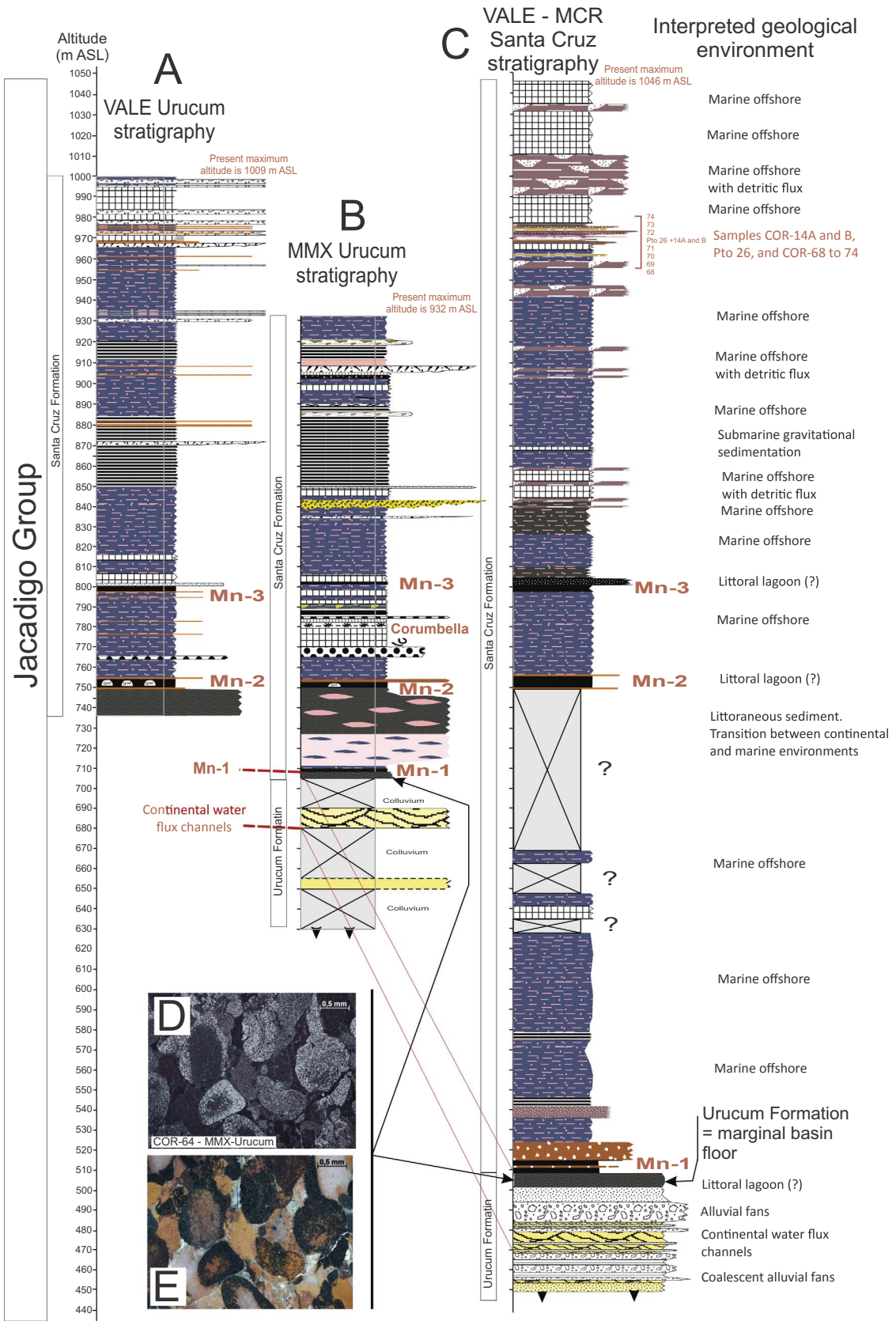

Fig. 2. Stratigraphic columns for the Jacadigo Group in the (A) VALE-Urucum Mine, (B) MMX-Urucum Mine, and (C) VALE-MCR Mine, showing the interpreted original sediments and depositional environments of each horizon. *Corumbella werneri* (Hahn et al., 1982) occur (Fig. 3) in layers of laminated BIFs, ironstone, and ferruginous sandstone between the Mn-2 and Mn-3 layers (column B). Note that in column C, because the layers are inclined, the total stratigraphic thickness of 290.3 m yields an apparent exposed thickness of 595 m spanning an elevation range from 1045 m to 450 m. The stratigraphy of the Urucum Formation in the VALE-MCR Mine is modified from Freitas et al. (2011). (D, E) Photomicrographs of ferruginous sandstone below the Lower Mn-1 ore layer. Note the rounded fragments of hematite and hematitic chert cemented by jasper and silica (RL = reflected light; D = parallel nicols (//N), E = crossed nicols (xN)). Abbreviations: qz = quartz; fk = K feldspar.

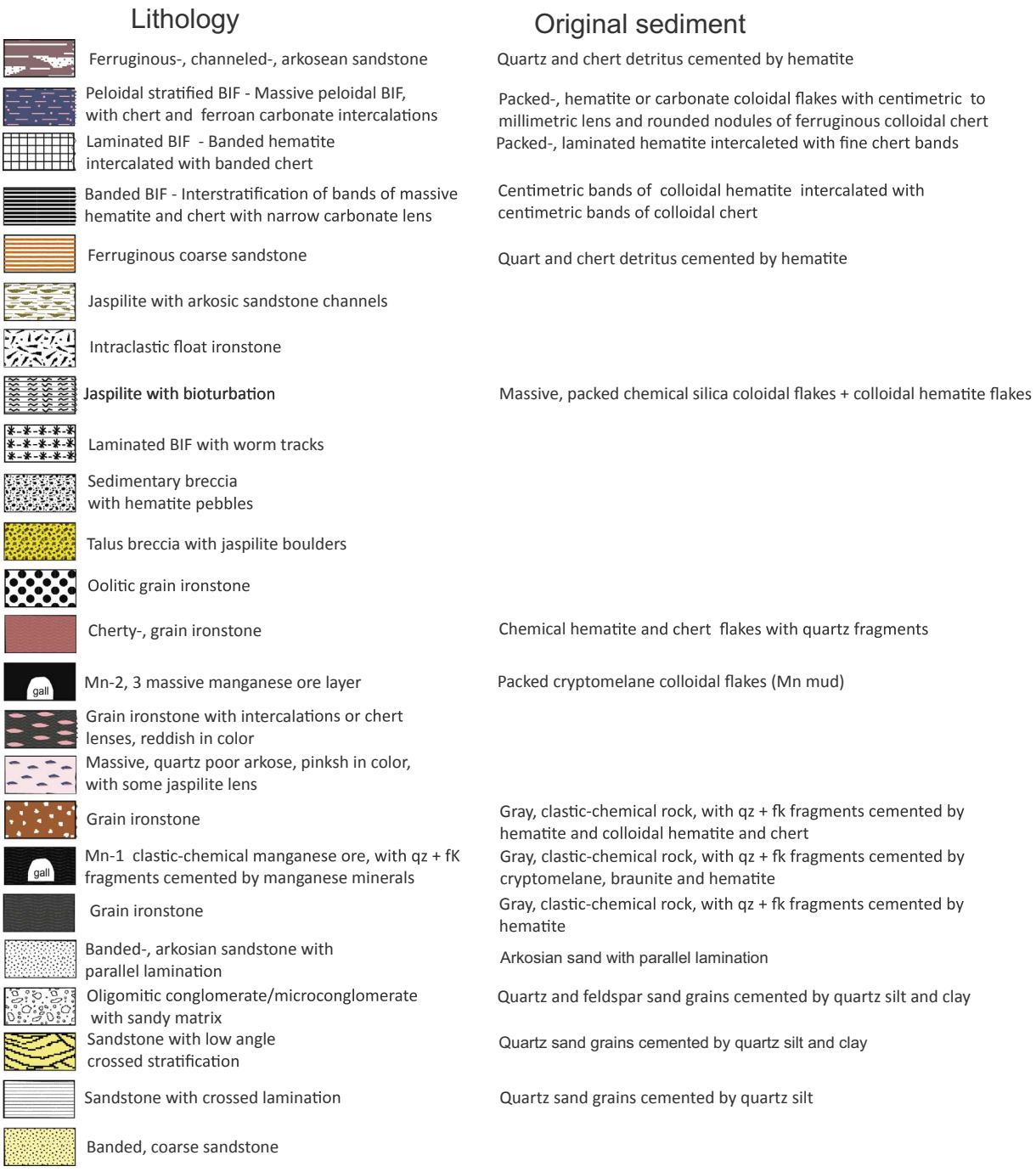

Fig. 2. (*continued*)

occur in the Tamengo Formation (Boggiani et al., 2010). Pleistocene deposits of the Xaraiés Formation, consisting of limestone and travertine, and sandy deposits and conglomerates of the Pantanal Formation (Fig. 1) overlie the basement and the Jacadigo and Corumbá Groups.

3. Age constraints

The age of the Jacadigo Group is based on the following data: (a) K-feldspar and biotite in the basement gneiss and granite were assigned K–Ar ages of 889 ± 44 Ma and 1730 ± 22 Ma, respectively (Hasui and Almeida, 1970); (b) Fossils from the Tamengo Formation, *Cloudina lucianoi* and *Corumbella werneri* (Beurlen and Sommer, 1957; Hahn et al., 1982; Zaine and Fairchild, 1985), are Ediacaran fossils whose ages were estimated at 550 Ma (Germs, 1972; Grant, 1990; Grotzinzer et al., 1995; Hofmann and Mountjoy, 2001; Bengtson, 2002); (c) Babinski et al. (2008) dated dEital zircons (U–Pb SHRIMP), from a volcanic ash layer intercalated with carbonate rocks of the Tamengo Formation, at 543 ± 3 Ma; and (d) Piacentini et al. (2013) obtained a $^{39}Ar/^{40}Ar$ age of 587 ± 7 Ma for the cryptomelane in layers Mn-1 to Mn-3 (Figs. 1–3). Piacentini et al. (2013) interpreted the $^{39}Ar/^{40}Ar$ age as a minimum age, arguing that the Ar/Ar thermochronological system was rejuvenated by tectonic warming from 547 ± 3 to 513 ± 4 Ma, indicated by the apparent recrystallization ages of braunite, which is considered to be metamorphic. Muscovite, which is also considered to be metamorphic, collected from the arkoses that are interlayered with the BIFs, was dated at 513 ± 3 Ma using the $^{39}Ar/^{40}Ar$ method. According to Piacentini et al. (2013), these ages are possibly related to

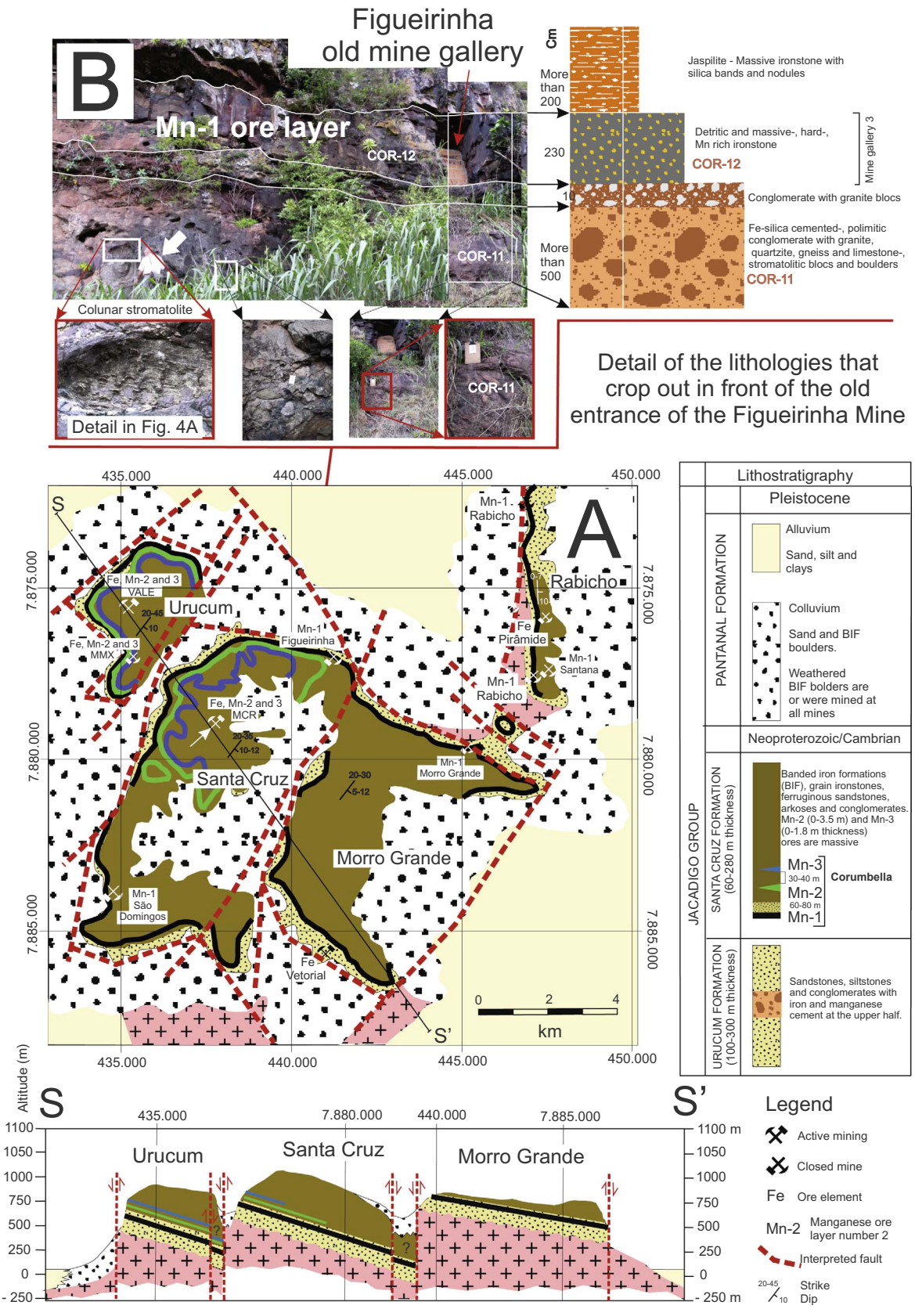

Fig. 3. (A) Map and geological section showing the positions of manganese layers Mn-1 to Mn-3 and the mines of the Urucum region (modified from Urban et al., 1992). The thicknesses of layers Mn-1 to Mn-3 are exaggerated by a factor of approximately ten. (B) Images of outcrops near the entrance to the Figueirinha Mn-1 manganese mine on the northern edge of the Santa Cruz plateau. In detail, these show a polymictic conglomerate containing a limestone boulder with columnar stromatolites (detail in Fig. 4A), and rounded blocks derived from the basement rocks. For scale, a person is indicated by the white arrow.

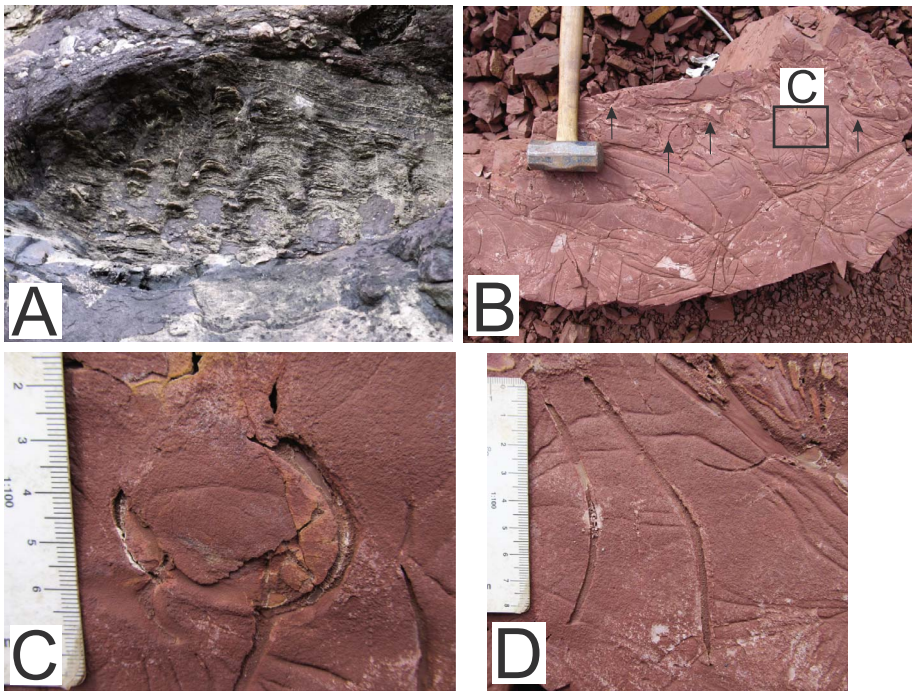

Fig. 4. (A) Detail of Fig. 3B, showing a carbonate block with columnar stromatolites; (B) Ironstone layer from the Santa Cruz Formation showing several examples of *Corumbella werneri*; (C) Detail of Fig. 4B; and (D) *Corumbella werneri* in layer of ferruginous sandstone from the Santa Cruz Formation.

disruption between the Amazon Craton and the Rio Apa cratonic fragment and they do not reflect the time of Jacadigo Group deposition, which would be greater than 590 Ma.

4. Petrography and chemistry of manganese ores and their host iron-rich rocks

4.1. Materials and methods

To avoid weathered samples, all of the manganese-rich samples were collected from the room supporting pillars and walls in old and operating underground mine galleries, and the iron-rich samples were collected from abandoned mining fronts in open pit mines, where the ore (oxidized BIFs) has already been removed. One hundred and eighteen thin sections and 96 polished sections were made and described. The thin section and polished section mineralogy was described and quantified using a ZEISS Axio Imager.A2m microscope, and the quantification was confirmed via the Rietveld analysis using a PANalytical Empyrean X-ray diffractometer with a rhodium tube operating at 60 kV and with a 60-s acquisition time. Based on their mineral compositions, textures, and structures, 80 samples from all the mines were selected and analyzed for oxides and trace elements (Table 1). The chemical analyses were performed by Actlabs in Vancouver (Canada) in accordance with procedures published online. Samples were crushed, split into fractions using a rifle splitter, and then pulverized in a mild carbon steel mill (95% passing 75 μm). Contamination during carbon steel pulverization is minor (< 0.2% Fe; traces of C, Mn, Si, Cr, Co). Cross-contamination between samples was minimized by repeated silica washes. Forty-one elements were analyzed using the analytical methods listed in Table 1, in order to determine the geochemical abundance by using the most appropriate method for each element. Loss of ignition (LOI) was determined at 1000°C. Actlabs includes certified reference materials and duplicates in the analyzed batch for quality control. Chemical analyses of rocks totaling less than 99% oxides (Table 1) usually occur when the rock contains minerals with high concentrations of cations with more than one valence, such as for the Urucum massive manganese ores containing cryptomelane and hollandite. Obeying the practice adopted by all laboratories, Actlabs express the Mn content as MnO, i.e., considering all of the Mn as Mn(II), which minimizes the sum value of all oxides in samples with high manganese contents. By means of SEM – EDS, 44 images of micrometer-scale structures were obtained and compositions were estimated for 210 points. The results are shown in tables next to the images in Figs. 9–11. Optical and SEM – EDS analyses were performed at the LAMIR (Laboratório de Análises de Minerais e Rochas), of the Geology Department in the Federal University of Paraná, using a SEM – EDS JEOL JSM – 6010LA apparatus operate as SEM (scanning electron microscope) in a vacuum at 20 kV and with a 15-s for images acquisition. The EDS analyzes were performed with an acquisition time of 60 s. The samples were polished and analyzed without metallization. When the EDS detector does not detect any element, the element content for the analyzed point is < 0.1, which is the lower limit of detection. The minimum free carbon content, shown in the columns titled “free C > ” in the tables in Figs. 9–11 was calculated assuming all the divalent cations are incorporated in carbonate crystals. To form carbonate crystals, each mole of carbon binds to one mole of a divalent cation (Ca, Mg, Fe, Mn, Ba, or Sr). Thus, the minimum wt% content of free carbon at the analyzed point = [number of moles of C − (number of moles of Ca + Mg + Fe + Mn + Ba + Sr)]/12.011. Therefore, whenever the calculated free C result was greater than zero, it was considered that the sample contained “carbonaceous matter” at the analyzed point. Reacting the sample with hydrochloric acid heated to 60°C tested for the presence of carbonate in all samples with high C content and, if the reaction was positive, the presence of carbonate was reported in the “Identification” column of Table 1. The interference of Ba over Eu when REEs are analyzed by ICP-MS in Ba-rich samples (Jarvis et al., 1989; Dulski, 1994) was evaluated by plotting the Ba versus Eu contents of Fe- and Mn-rich samples (Table 1). The diagram showed that Ba overlap is small to 1000 ppm Ba in iron-rich samples, and unimportant even up to 15,000, in manganese-rich samples, suggesting that the correlation between Ba and Eu levels is weak or non-existent in the analyzed samples. It is therefore valid to work with the analyzed Eu contents and to calculate anomaly values of this element.

4.2. Layer Mn-1

The Figueirinha and São Domingos mines are the main locations mining Mn-1 in the Urucum region (Fig. 3). In these mines, the Lower

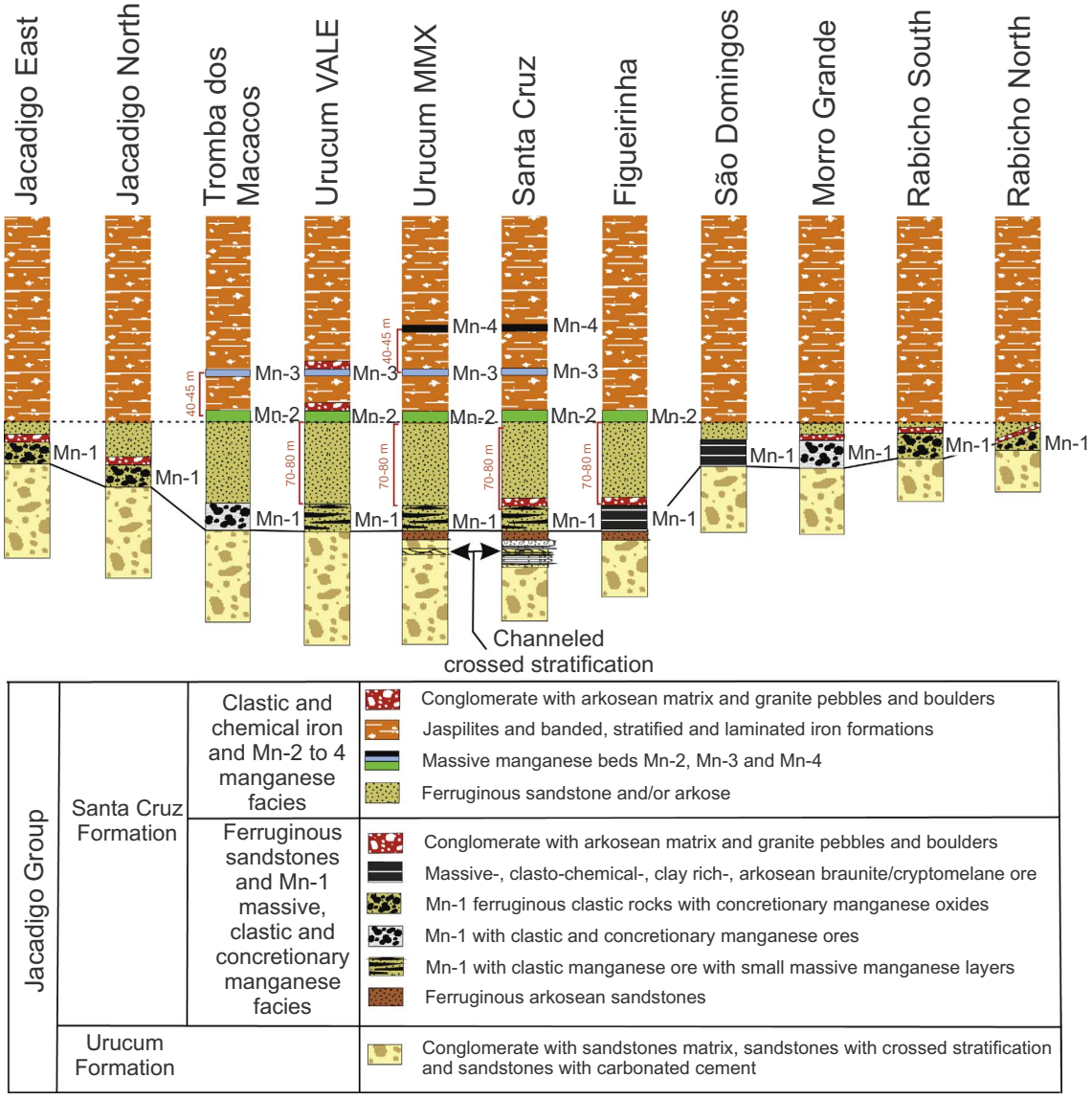

Fig. 5. Stratigraphic columns for the Jacadigo Group, arranged according to distance from the Santa Cruz plateau, where the Figueirinha and São Domingos mines are located (modified from Urban et al., 1992). The column elevations are normalized to the stratigraphic position of layer Mn-2 or, where this layer is absent, to the IF base.

Mn-1 ore layer is characterized by sandstone with fragments of quartz, feldspar, apatite, chert, and hematite cemented by manganese oxides. In the Figueirinha Mine, the Upper Mn-1 ore layer is devoid of hematite and consists of 30–75 vol% braunite, 3–15 vol% quartz, 5–10 vol% feldspar, and 1–5 vol% association of clay minerals–apatite–chlorite. Locally, the matrix contains 10–30 vol% Fe-dolomite or siderite + manganoan dolomite (Table 1). The only place in the Urucum region where the manganese ore has a high content of braunite is the Mn-1 ore layer in the Figueirinha Mine. In the São Domingos Mine, the Upper Mn-1 ore layer is laminated and contains amygdalites (Fig. 6C), and consists of 40–75 vol% cryptomelane–hollandite, 10–30 vol% quartz, and 10–15 vol% association of hematite (7–11% Fe_2O_3)–apatite–clay minerals. It contains no braunite, feldspar, or carbonate. Locally in this mine, the Lower Mn-1 ore layer displays parallel banding and contains 75 vol% cryptomelane (+pyrolusite?), 10–12 vol % hematite, and 10–13 vol% quartz–chert, which is similar in composition to the upper layer.

The composition of the amygdalite cores in the Upper Mn-1 layer, estimated optically from polished sections, consist of 60–90 vol% cryptomelane (+hollandite?), 0–10 vol% quartz, 10–15 vol% hematite–clay minerals and pores. Massive cryptomelane, containing a few clasts and then becoming a clastic zone composed of quartz, hematite, chamosite, and cryptomelane, surrounds the cores (Fig. 6H and I). Therefore, there is a transition from the metallic manganese core to the detrital granular wrap.

The Lower Mn-1 layer overlies conglomerates with a ferruginous arkosic matrix or ferruginous arkosic sandstone whose composition is 20–87 vol% hematite (10–75% Fe_2O_3), 5–50 vol% quartz–chert, 10–30 vol% feldspar, and 0–5 vol% braunite–apatite–clay minerals–hematite fragments (Fig. 6J–K). The matrix of these rocks comprises hematite and ferruginous chert.

Surrounding the Santa Cruz plateau, the Mn-1 layer in all the other mines contains detrital, concretionary, or breccia- or earth-like ores. In the VALE-Urucum and MMX-Urucum mines, located on the Urucum plateau, and in the Rabicho Mine (Figs. 3 and 5), the ore comprises an arkosic sandstone cemented by hollandite (± cryptomelane)–quartz–feldspar–hematite, with 30–40% MnO, 30–35% SiO_2, 5–10% Fe_2O_3, 3–7% Al_2O_3, 1.5–2.5% K_2O, and 1.0–2.5% Ba. In the Rabicho and Morro Grande mines (Fig. 6E–F), the layered dETRital ore consists of 60–70 vol% pyrolusite, 15–25 vol% hematite, and 15–25 vol% quartz; and the concretionary ore contains 70–80 vol% cryptomelane and 20–30 vol% pyrolusite. These ores are hosted in ferruginous

Table 1
Chemical compositions and mineralogy of rocks and ores from the Urucum manganese and iron deposits.

Analyte Symbol				% SiO2	% Al2O3	% TiO2	% Fe2O3(T)	% Fe	% FeO	% MnO	% Mn	% MgO	% CaO	% Ba	% Na2O
Detection Limit				0.01	0.01	0.001	0.01	0.01	0.1	0.001	0.01	0.01	0.01	3 ppm	0.01
Analysis Method				FUS-ICP	FUS-ICP	FUS-ICP	Calculated	FUS-ICP	TITR	Calculated	FUS-XRF	FUS-ICP	FUS-ICP	FUS-ICP	FUS-ICP
Sample	Mine	Layer-Figure loc.	Minerals												
COR 74W	MCR-VALE	Fe, Fig.2C		10.7	1.93	0.057	86.85	60.73		0.02	0.02	0.04	0.01	0.014	0.03
COR 73W	MCR-VALE	Fe, Fig.2C		10.04	0.1	0.028	89.96	62.91		0.01	0.01	0.02	0.12	0.005	< 0.01
COR 72W	MCR-VALE	Fe, Fig.2C		34.09	0.11	0.023	64.56	45.15		0.01	0.01	0.01	0.07	0.016	< 0.01
COR 71W	MCR-VALE	Fe, Fig.2C		30.03	0.12	0.022	69.89	48.87		0.01	0.01	0.01	0.09	0.016	0.03
COR 70W	MCR-VALE	Fe, Fig.2C		39.72	0.09	0.019	59.35	41.50		0.01	0.01	0.01	0.07	0.014	< 0.01
COR 74D	MCR-VALE	Fe, Fig.2C		1.74	0.91	0.09	96.51	67.49	< 0.1	< 0.01	< 0.01	< 0.01	< 0.01	0.005	< 0.01
COR 73D	MCR-VALE	Fe, Fig.2C		7.89	0.04	0.03	90.89	63.56	< 0.1	< 0.01	< 0.01	< 0.01	0.03	0.007	< 0.01
COR 72D	MCR-VALE	Fe, Fig.2C		8.69	0.18	0.03	90.57	63.34	< 0.1	< 0.01	< 0.01	< 0.01	0.02	0.009	< 0.01
COR 71D	MCR-VALE	Fe, Fig.2C		10.66	0.08	0.03	88.01	61.55	0.1	< 0.01	< 0.01	< 0.01	0.02	0.018	< 0.01
COR 70D	MCR-VALE	Fe, Fig.2C		12.76	0.01	0.03	86.52	60.50	< 0.1	< 0.01	< 0.01	< 0.01	0.02	0.012	< 0.01
COR 14A	MCR-VALE	Fe, Fig.2C	12 gth + 88 qz	82.63	0.08	0.003	13.09	9.15	< 0.1	0.07	0.05	0.06	0.07	0.002	< 0.01
COR 74	MCR-VALE	Fe, Fig.2C		2.64	1.01	0.09	95.54	66.81	< 0.1	< 0.01	< 0.01	< 0.01	< 0.01	0.006	< 0.01
COR 73	MCR-VALE	Fe, Fig.2C		8.11	0.05	0.03	90.80	63.49	< 0.1	< 0.01	< 0.01	< 0.01	0.04	0.007	< 0.01
COR 72	MCR-VALE	Fe, Fig.2C		12.50	0.17	0.03	86.67	60.61	< 0.1	< 0.01	< 0.01	< 0.01	0.03	0.010	< 0.01
COR 71	MCR-VALE	Fe, Fig.2C		13.57	0.09	0.03	85.29	59.64	0.1	< 0.01	< 0.01	< 0.01	0.03	0.018	0.01
COR 70	MCR-VALE	Fe, Fig.2C		18.15	0.03	0.03	81.09	56.70	< 0.1	< 0.01	< 0.01	< 0.01	0.03	0.013	< 0.01
COR 14	MCR-VALE	Fe, Fig.2C	89 hmt + 11 qz	11.02	0.47	0.03	88.09	61.60	0.2	< 0.01	< 0.01	0.01	0.04	0.007	< 0.01
COR 69	MCR-VALE	Fe, Fig.2C		43.95	0.11	0.021	55.15	38.57		0.01	0.01	0.02	0.07	0.007	< 0.01
COR 68	MCR-VALE	Fe, Fig.2C		45.62	0.44	0.031	53.41	37.35		0.01	0.01	0.02	0.05	0.014	< 0.01
COR 67	MCR-VALE	Fe, Fig.2C		27.46	3.03	0.22	67.95	47.52		< 0.01	< 0.01	0.03	< 0.01	0.021	< 0.01
COR 66	MCR-VALE	Fe, Fig.2C	hmt + qz	44.72	1.83	0.223	52.51	36.72		0.26	0.20	0.08	0.04	0.045	0.01
Pto 26W	MCR-VALE	Fe, Fig.2C	hmt + qz	28.38	0.14	0.024	70.77	49.49		0.03	0.02	0.02	0.1	0.005	< 0.01
Pto 26D	MCR-VALE	Fe, Fig.2C	hmt + qz	12.37	< 0.01	0.04	86.48	60.48	0.1	< 0.01	< 0.01	< 0.01	0.03	0.005	< 0.01
Pto 18W	MCR-VALE	Mn-3, Fig. 7	27 hmt + 63 qz	45.13	0.2	0.028	54.55	38.15		0.02	0.01	0.01	0.05	0.018	< 0.01
Pto 18D	MCR-VALE	Mn-3, Fig. 7	67 hmt + 33 qz	18.02	0.1	0.04	80.21	56.09		< 0.01	< 0.01	< 0.01	< 0.01	0.005	< 0.01
COR 21	MCR-VALE	Mn-3, Fig. 7	hmt + chert	9.2	2.29	0.353	85.75	59.97		0.45	0.35	0.02	< 0.01	0.130	0.06
COR 22	MCR-VALE	Mn-3, Fig. 7	38 hmt + 9 hol + 53 qz	52.36	0.76	0.16	35.85	25.07		8.71	6.75	< 0.01	< 0.01	0.345	< 0.01
COR 20	MCR-VALE	Mn-3, Fig. 7	53 hmt + 47 cry	0.2	1.06	0.19	49.79	34.82		38.08	29.50	< 0.01	0.06	0.413	0.01
COR 16P	MCR-VALE	Mn-3, Fig. 7	19 hmt + 81 cry + holl	0.55	1	0.26	16.66	11.65		60.94	47.20	< 0.01	0.09	1.040	0.04
COR 16M	MCR-VALE	Mn-3, Fig. 7	25 hmt + 75 cry	< 0.01	0.38	0.23	23.71	16.58		55.90	43.30	< 0.01	0.12	0.691	0.01
COR 17	MCR-VALE	Mn-3, Fig. 7	33 hmt + 67 cry+hol	0.56	1.84	0.28	31.08	21.73		48.15	37.30	< 0.01	0.04	0.826	< 0.01

(*continued on next page*)

Table 1 (*continued*)

Analyte Symbol				% SiO2	% Al2O3	% TiO2	% Fe2O3(T)	% Fe	% FeO	% MnO	% Mn	% MgO	% CaO	% Ba	% Na2O
Detection Limit				0.01	0.01	0.001	0.01	0.01	0.1	0.001	0.01	0.01	0.01	3 ppm	0.01
Analysis Method				FUS-ICP	FUS-ICP	FUS-ICP	Calculated	FUS-ICP	TITR	Calculated	FUS-XRF	FUS-ICP	FUS-ICP	FUS-ICP	FUS-ICP
COR 48L	Urucum-VALE	Mn-3, Fig. 7	91 cry + 9 bra	1.73	0.48	0.14	12.24	8.56		64.81	50.20	< 0.01	0.44	0.296	0.5
COR 48P	Urucum-VALE	Mn-3, Fig. 7	95 cry + 9 bra	0.27	0.37	0.18	8.7	6.08		67.39	52.20	0.02	0.36	0.439	0.71
COR 47W	Urucum-VALE	Fe/Mn-3, Fig. 7	56 hmt + 44 qz	33.51	0.46	0.036	64.17	44.87		0.04	0.03	0.02	0.05	0.008	< 0.01
COR 47D	Urucum-VALE	Fe/Mn-3, Fig. 7	58 hmt + 42 qz	32.65	0.24	0.04	66.46	46.48	< 0.1	< 0.01	< 0.01	< 0.01	< 0.01	0.009	< 0.01
COR 46W	Urucum-VALE	Fe/Mn-3, Fig. 7	65 hmt + 35 qz	26.68	0.23	0.039	73.23	51.21		0.01	0.01	0.02	< 0.01	0.008	< 0.01
COR 46D	Urucum-VALE	Fe/Mn-3, Fig. 7	61 hmt + 39 qz	29.13	0.27	0.04	70.6	49.37	< 0.1	< 0.01	< 0.01	< 0.01	< 0.01	0.007	< 0.01
COR 45	Urucum-VALE	Mn-2, Fig. 7	hmt + qz	20.36	4.65	0.273	68.3	47.76		1.78	1.38	0.02	0.07	0.026	0.02
COR 37	Urucum-VALE	Mn-2, Fig. 7	hmt + qz	51.03	0.09	0.16	47.56	33.26		0.40	0.31	< 0.01	< 0.01	0.019	< 0.01
COR 44	Urucum-VALE	Mn-2, Fig. 7	21 hmt + 79 cry	1.05	3.19	0.17	20.94	14.64		55.00	42.60	< 0.01	< 0.01	0.256	0.17
COR 41	Urucum-VALE	Mn-2, Fig. 7	15 hmt + 85 holl	< 0.01	0.69	0.14	13.89	9.71		63.90	49.50	< 0.01	0.03	0.116	0.22
COR 36a	Urucum-VALE	Mn-2, Fig. 7	77 cry +23 holl	0.09	0.49	0.13	9.1	6.36		66.49	51.50	0.02	0.08	0.231	0.15
COR 43	Urucum-VALE	Mn-2, Fig. 7	9 hmt + 91 cry + ?holl	0.54	0.9	0.16	13.4	9.37		64.29	49.80	0.01	0.1	0.068	0.65
COR 36b	Urucum-VALE	Mn-2, Fig. 7	96 cry + 4 holl	0.01	0.38	0.16	7.57	5.29		67.26	52.10	0.02	0.08	0.296	0.18
COR-75	Urucum-VALE	Mn-2, Fig. 7		< 0.01	1.24	0.16	16.18	11.31		62.10	48.10	0.15	0.74	0.071	0.53
COR 42	Urucum-VALE	Mn-2, Fig. 7	19 hmt + 81 holl	< 0.01	< 0.01	0.16	19.42	13.58		60.94	47.20	< 0.01	< 0.01	0.071	0.13
COR 40	Urucum-VALE	Mn-2, Fig. 7	34 hmt + 53 holl + 13 cht	2.89	2.03	0.29	37.03	25.90		42.47	32.90	< 0.01	< 0.01	0.349	0.2
COR 39	Urucum-VALE	Mn-2, Fig. 7	hmt + qz	45.9	1.96	0.13	49.12	34.35		1.81	1.40	0.04	0.06	0.012	0.01
COR 38	Urucum-VALE	Mn-2, Fig. 7	hmt + qz	41.12	2.13	0.234	53.9	37.69		1.49	1.15	0.07	0.08	0.098	< 0.01
COR 76	Urucum-MMX	Fe, Fig. 7	hmt	1.2	0.41	0.04	98.19	68.66		< 0.01	< 0.01	< 0.01	< 0.01	0.015	< 0.01
COR 77	Urucum-MMX	Fe, Fig. 7	hmt + qz	10.02	0.25	0.04	88.32	61.76		< 0.01	< 0.01	< 0.01	< 0.01	0.018	< 0.01

(*continued on next page*)

Table 1 (*continued*)

Analyte Symbol				% SiO2	% Al2O3	% TiO2	% Fe2O3(T)	% Fe	% FeO	% MnO	% Mn	% MgO	% CaO	% Ba	% Na2O
Detection Limit				0.01	0.01	0.001	0.01	0.01	0.1	0.001	0.01	0.01	0.01	3 ppm	0.01
Analysis Method				FUS-ICP	FUS-ICP	FUS-ICP	Calculated	FUS-ICP	TITR	Calculated	FUS-XRF	FUS-ICP	FUS-ICP	FUS-ICP	FUS-ICP
COR 63W	Urucum-MMX	Mn-2, Fig. 7	88 hmt + 12 kao	4.74	4.01	0.324	85.02	59.45		2.15	1.66	0.03	0.07	0.030	0.01
COR 63D	Urucum-MMX	Mn-2, Fig. 7	88 hmt + 12 kao	4.92	3.87	0.31	85.33	59.67		2.53	1.96	< 0.01	< 0.01	0.035	< 0.01
COR 78	Urucum-MMX	Mn-2, Fig. 7		3.23	4.54	0.28	20.77	14.52		51.51	39.90	< 0.01	0.66	0.283	0.29
COR 62	Urucum-MMX	Mn-2, Fig. 7	81cry + 19 bra + holl	2.08	0.2	0.29	14.5	10.14		63.90	49.50	0.14	0.1	1.130	0.18
COR 61L	Urucum-MMX	Mn-2, Fig. 7	90 cry+ 10 hmt	1.35	0.08	0.13	12.97	9.07		65.20	50.50	< 0.01	0.36	0.041	0.5
COR 61P	Urucum-MMX	Mn-2, Fig. 7	93 cry + 7 hmt	0.89	0.5	0.13	9.44	6.60		68.04	52.70	0.03	0.54	0.065	0.6
COR 60	Urucum-MMX	Mn-2, Fig. 7	hmt + cry	4.22	5.04	0.29	23.76	16.62		47.25	36.60	0.02	0.66	0.303	0.3
COR 59	Urucum-MMX	Mn-2, Fig. 7	hmt + cry- + holl	2.94	3.94	0.334	36.65	25.63		41.76	32.35	0.08	0.39	0.486	0.35
COR 79	Urucum-MMX	Fe, Fig. 7	hmt + qz	47	1.23	0.106	51.31	35.88		0.26	0.20	0.03	0.05	0.008	< 0.01
COR 07	Figueirinha	Mn-1, Fig. 15	63 bra (clastic) + 4 qz + 10 ab + 10 kao + 13 dol	30.59	3.4	0.34	11.21	7.84		42.60	33.00	2.52	0.86	0.095	3.23
COR 06	Figueirinha	Mn-1, Fig. 15	cry + holl	10.9	1.52	0.37	5.15	3.60		66.62	51.60	0.19	0.6	1.290	< 0.01
Pto 51	Figueirinha	Mn-1, Fig. 15	65 bra (clastic)+ 4 kao + 32 ply	33.57	4.01	0.37	11.74	8.21		37.44	29.00	2.93	1.17	0.133	3.99
COR 04	Figueirinha	Mn-1, Fig. 15	87 hmt + 13 qz	14.01	1.78	0.16	74.51	52.10		5.64	4.37	0.44	0.77	0.124	0.36
COR 02	Figueirinha	Mn-1, Fig. 15	24 hmt + 42 qz + 25 mc + 8 alb	46.79	5.36	0.303	32.11	22.45		7.87	6.09	0.38	0.93	0.165	1.15
COR 09a	Figueirinha	Mn-1, Fig. 15	60 cry + 40 holl	1.02	0.77	0.2	2.25	1.57		70.88	54.90	0.02	0.14	0.833	< 0.01
COR 09b	Figueirinha	Mn-1, Fig. 15	75 bra (clastic)+ 25 mc	18.36	3.03	0.33	14.67	10.26		49.06	38.00	0.22	0.92	1.040	< 0.01
COR 10	Figueirinha	Mn-1, Fig. 15	32 bra (clastic)+ 37 qz + 26 mcc + 2 ank	39.17	3.11	0.27	19.44	13.59		31.11	24.10	0.01	0.62	0.432	1.11

(*continued on next page*)

Table 1 (*continued*)

Analyte Symbol				% SiO2	% Al2O3	% TiO2	% Fe2O3(T)	% Fe	% FeO	% MnO	% Mn	% MgO	% CaO	% Ba	% Na2O
Detection Limit				0.01	0.01	0.001	0.01	0.01	0.1	0.001	0.01	0.01	0.01	3 ppm	0.01
Analysis Method				FUS-ICP	FUS-ICP	FUS-ICP	Calculated	FUS-ICP	TITR	Calculated	FUS-XRF	FUS-ICP	FUS-ICP	FUS-ICP	FUS-ICP
COR 12	Figueirinha	Mn-1, Fig. 15	hmt + qz- + kao + -mc	49.48	4.57	0.273	26.64	18.63		9.11	7.06	0.96	0.72	0.504	0.07
COR 35	São Domingos	Mn-1, Fig. 15	hmt + qz	40.2	5.33	0.36	48.05	33.60		1.32	1.02	0.06	0.17	0.013	< 0.01
COR 32	São Domingos	Mn-1, Fig. 15	12 hmt + 60 holl + 28 qz	17.09	3.3	0.35	10.38	7.26		50.99	39.50	0	0	0.153	0.35
COR 33	São Domingos	Mn-1, Fig. 15	9 hmt + 43 cry + 9 bra (clastic)+ 11qz + 28 mc	23.73	3.61	0.33	9.51	6.65		46.35	35.90	< 0.01	0.01	0.135	0.31
COR 31	São Domingos	Mn-1, Fig. 15	hmt + qz	37.66	5.16	0.33	34.02	23.79		15.46	11.98	0.02	0.05	0.112	0.06
COR 30	São Domingos	Mn-1, Fig. 15	12 hmt + 75 hol + 13 qz + ? pyr	12.3	0.73	0.16	7.69	5.38		59.64	46.20	0.74	0.05	0.030	0.81
COR 65	MMX	Mn-1, Fig. 15	hmt + cry- + holl + q-z	32.26	6.49	0.87	7.77	5.43		36.15	28.00	0.11	0.01	2.510	< 0.01
COR 23	Rabicho	Mn-1, Fig. 15	19 hmt + 63 pyr + 17 qz	2.74	3.82	0.47	15.29	10.69		56.93	44.10	< 0.01	< 0.01	0.720	< 0.01
COR 26	Rabicho	Mn-1, Fig. 15	cry + pyr- + qz	32.55	3.55	0.47	19.04	13.31		31.11	24.10	0.29	0.1	0.731	< 0.01
Pto 48	Rabicho	Mn-1, Fig. 15	65 hmt + 34 qz	15.21	0.17	0.04	84.1	58.81		< 0.01	< 0.01	< 0.01	0.01	0.023	< 0.01
Pto 50	Rabicho	Mn-1, Fig. 15		48.73	2.55	0.22	38.93	27.22		5.68	4.40	< 0.01	< 0.01	0.041	< 0.01
COR 28	Jacadigo	Mn-1, Fig. 15		0.42	0.32	0.04	0.83	0.58		75.65	58.60	0.01	0.35	0.112	< 0.01

Analyte Symbol				ppm Zr	ppm Cu	ppm Pb	ppm Zn	ppm Co	ppm Ni	ppm Y	ppm La	ppm Ce	ppm Pr	ppm Nd	ppm Sm
Detection Limit				5	10	5	30	1	20		0.1	0.1	0.05	0.1	0.1
Analysis Method				FUS-MS	FUS-MS	FUS-MS	FUS-MS	FUS-MS	FUS-MS		FUS-MS	FUS-MS	FUS-MS	FUS-MS	FUS-MS
Sample	Mine	Layer-Figure loc.	Minerals												
COR 74W	MCR-VALE	Fe, Fig.2C		14	< 10	< 5	< 30	15	< 20	< 2	17.5	29.6	4.46	17.5	3.5
COR 73W	MCR-VALE	Fe, Fig.2C		11	< 10	< 5	< 30	41	< 20	< 2	10.9	18.3	2.87	11.4	2.4
COR 72W	MCR-VALE	Fe, Fig.2C		23	< 10	< 5	< 30	43	< 20	< 2	18	28.7	4.71	19.5	4.3
COR 71W	MCR-VALE	Fe, Fig.2C		24	< 10	< 5	< 30	53	< 20	< 2	15.3	23.7	4.4	17.9	3.7
COR 70W	MCR-VALE	Fe, Fig.2C		33	< 10	< 5	< 30	59	< 20	< 2	22.3	36.4	6.69	26.6	5.5
COR 74D	MCR-VALE	Fe, Fig.2C		28	< 10	< 5	< 30	9	< 20	9	4.5	8	1.36	6	1.3

(*continued on next page*)

Table 1 (*continued*)

Analyte Symbol				% SiO2	% Al2O3	% TiO2	% Fe2O3(T)	% Fe	% FeO	% MnO	% Mn	% MgO	% CaO	% Ba	% Na2O
Detection Limit				0.01	0.01	0.001	0.01	0.01	0.1	0.001	0.01	0.01	0.01	3 ppm	0.01
Analysis Method				FUS-ICP	FUS-ICP	FUS-ICP	Calculated	FUS-ICP	TITR	Calculated	FUS-XRF	FUS-ICP	FUS-ICP	FUS-ICP	FUS-ICP
COR 73D	MCR-VALE	Fe, Fig.2C		25	< 10	< 5	< 30	44	< 20	14	11.8	19.1	3.05	12.4	2.5
COR 72D	MCR-VALE	Fe, Fig.2C		28	< 10	< 5	< 30	37	< 20	13	10.8	19.5	2.95	12.7	3.2
COR 71D	MCR-VALE	Fe, Fig.2C		22	< 10	< 5	< 30	47	< 20	23	11.5	20.3	3.49	14.2	3.2
COR 70D	MCR-VALE	Fe, Fig.2C		28	< 10	< 5	< 30	39	< 20	15	11.2	20.5	3.67	15.1	3.4
COR 14A	MCR-VALE	Fe, Fig.2C	12 gth + 88 qz	8	< 10	< 5	< 30	63	< 20	5	29.3	56	6.85	28.6	6.2
COR 74	MCR-VALE	Fe, Fig.2C		11	< 10	< 5	< 30	10	< 20	7	5.8	10.2	1.7	7.2	1.5
COR 73	MCR-VALE	Fe, Fig.2C		24	< 10	< 5	< 30	44	< 20	12	11.7	19.0	3.0	12.3	2.5
COR 72	MCR-VALE	Fe, Fig.2C		29	< 10	< 5	< 30	38	< 20	11	11.9	20.9	3.2	13.7	3.4
COR 71	MCR-VALE	Fe, Fig.2C		28	< 10	< 5	< 30	48	< 20	12	12.1	20.8	3.6	14.8	3.3
COR 70	MCR-VALE	Fe, Fig.2C		27	< 10	< 5	< 30	43	< 20	17	13.4	23.7	4.3	17.4	3.8
COR 14	MCR-VALE	Fe, Fig.2C	89 hmt + 11 qz	24	< 10	< 5	< 30	72	< 20	< 2	9.9	18	2.82	11.2	2.5
COR 69	MCR-VALE	Fe, Fig.2C		17	< 10	< 5	< 30	61	< 20	< 2	8	12.6	2.33	9.7	2
COR 68	MCR-VALE	Fe, Fig.2C		33	< 10	< 5	< 30	57	< 20	12	14.8	21.2	5.04	21.1	4
COR 67	MCR-VALE	Fe, Fig.2C		40	20	< 5	< 30	24	< 20	< 2	39.3	62.3	10.9	41	6.8
COR 66	MCR-VALE	Fe, Fig.2C	hmt + qz	88	< 10	< 5	< 30	157	50	< 2	44	93.1	14.2	58.8	11.5
Pto 26W	MCR-VALE	Fe, Fig.2C	hmt + qz	15	< 10	< 5	< 30	36	< 20	15	7.1	13.1	1.81	7.6	1.4
Pto 26D	MCR-VALE	Fe, Fig.2C	hmt + qz	21				33	< 20	15	7.4	14.8	2.15	9.4	1.9
Pto 18W	MCR-VALE	Mn-3, Fig. 7	27 hmt + 63 qz	17	< 10	< 5	< 30	48	< 20	< 2	14.1	27.3	4.89	22.6	4.9
Pto 18D	MCR-VALE	Mn-3, Fig. 7	67 hmt + 33 qz	16	< 10	< 5	< 30	32	< 20	20	8.2	16.9	2.64	11.9	2.7
COR 21	MCR-VALE	Mn-3, Fig. 7	hmt + chert	55	< 10	< 5	< 30	57	< 20	< 2	14.9	29.7	8.12	45.9	15.3
COR 22	MCR-VALE	Mn-3, Fig. 7	38 hmt + 9 hol + 53 qz	31	20	< 5	< 30	112	< 20	13	8.4	20.4	2.14	8.3	1.6
COR 20	MCR-VALE	Mn-3, Fig. 7	53 hmt + 47 cry	48	40	6	40	189	70	25	15.9	38.9	3.66	15.7	3.6
COR 16P	MCR-VALE	Mn-3, Fig. 7	19 hmt + 81 cry + holl	44	70	< 5	50	229	20	24	29	159	9.45	35.2	8.3
COR 16M	MCR-VALE	Mn-3, Fig. 7	25 hmt + 75 cry	27	60	< 5	40	228	< 20	22	24.5	118	8.62	34.4	8.3
COR 17	MCR-VALE	Mn-3, Fig. 7	33 hmt + 67 cry + hol	42	40	< 5	40	200	< 20	19	38.8	201	12.1	46.9	10.9
COR 48L	Urucum-VALE	Mn-3, Fig. 7	91 cry + 9 bra		30	6	40	230	30	17	20.2	44.7	4.32	15.4	2.7
COR 48P	Urucum-VALE	Mn-3, Fig. 7	95 cry + 9 bra		10	< 5	< 30	216	30	11	16.5	5.7	2.41	7.8	1.3
COR 47W	Urucum-VALE	Fe/Mn-3, Fig. 7	56 hmt + 44 qz	5	10	< 5	< 30	29	< 20	< 2	8.7	16.2	2.13	9	2.1

(*continued on next page*)

Table 1 (*continued*)

Analyte Symbol				% SiO2	% Al2O3	% TiO2	% Fe2O3(T)	% Fe	% FeO	% MnO	% Mn	% MgO	% CaO	% Ba	% Na2O
Detection Limit				0.01	0.01	0.001	0.01	0.01	0.1	0.001	0.01	0.01	0.01	3 ppm	0.01
Analysis Method				FUS-ICP	FUS-ICP	FUS-ICP	Calculated	FUS-ICP	TITR	Calculated	FUS-XRF	FUS-ICP	FUS-ICP	FUS-ICP	FUS-ICP
COR 47D	Urucum-VALE	Fe/Mn-3, Fig. 7	58 hmt + 42 qz	7	< 10	< 5	< 30	34	< 20	7	6.6	12.5	1.65	7.4	1.9
COR 46W	Urucum-VALE	Fe/Mn-3, Fig. 7	65 hmt + 35 qz	8	< 10	< 5	< 30	31	< 20	< 2	8.4	16.9	2.61	12.6	3
COR 46D	Urucum-VALE	Fe/Mn-3, Fig. 7	61 hmt + 39 qz	9	< 10	< 5	< 30	29	< 20	9	6.5	12.8	1.79	8.4	2
COR 45	Urucum-VALE	Mn-2, Fig. 7	hmt + qz	122	< 10	< 5	< 30	108	70	< 2	11.5	24	4.1	17.1	3.4
COR 37	Urucum-VALE	Mn-2, Fig. 7	hmt + qz	85	< 10	< 5	< 30	100	50	11	19.7	39.1	6.14	28.9	7.5
COR 44	Urucum-VALE	Mn-2, Fig. 7	21 hmt + 79 cry	36	50	6	40	486	< 20	96	14.5	25.6	3.41	12.5	2.7
COR 41	Urucum-VALE	Mn-2, Fig. 7	15 hmt + 85 holl	29	20	< 5	40	477	30	50	19.4	29.5	5.07	19.1	3.8
COR 36a	Urucum-VALE	Mn-2, Fig. 7	77 cry +23 holl	6	30	< 5	60	371	40	24	33.1	38.5	5.94	20.8	3.9
COR 43	Urucum-VALE	Mn-2, Fig. 7	9 hmt + 91 cry + ?holl	31	10	< 5	50	418	< 20	15	18.8	24.4	4.06	15.2	3.1
COR 36b	Urucum-VALE	Mn-2, Fig. 7	96 cry + 4 holl	8	20	< 5	40	414	40	14	25	28.9	3.88	13.5	2.3
COR-75	Urucum-VALE	Mn-2, Fig. 7		38	20	< 5	60	512	40	35	21.8	27.7	4.64	17.6	3.6
COR 42	Urucum-VALE	Mn-2, Fig. 7	19 hmt + 81 holl	24	10	< 5	< 30	399	< 20	13	20.5	22.9	4.19	15.1	2.6
COR 40	Urucum-VALE	Mn-2, Fig. 7	34 hmt + 53 holl + 13 cht	90	< 10	5	< 30	188	60	19	29.6	47.3	6.73	24.6	4.1
COR 39	Urucum-VALE	Mn-2, Fig. 7	hmt + qz	120	< 10	< 5	< 30	102	40	< 2	11.2	19.6	2.88	11.4	2.3
COR 38	Urucum-VALE	Mn-2, Fig. 7	hmt + qz	80	< 10	< 5	< 30	50	< 20	< 2	9.1	16.9	2.18	8.4	1.5
COR 76	Urucum-MMX	Fe, Fig. 7	hmt	10	< 10	< 5	< 30	17	< 20	11	13.3	21.6	3.46	14.1	2.9
COR 77	Urucum-MMX	Fe, Fig. 7	hmt + qz	9	< 10	< 5	< 30	19	< 20	15	17.6	26.9	4.56	19	3.9
COR 63W	Urucum-MMX	Mn-2, Fig. 7	88 hmt + 12 kao	82	< 10	7	< 30	80	90	< 2	11.5	22.3	3.23	13	2.4
COR 63D	Urucum-MMX	Mn-2, Fig. 7	88 hmt + 12 kao	72	< 10	29	< 30	92	90	10	10.3	19.2	3.14	12.6	2.4
COR 78	Urucum-MMX	Mn-2, Fig. 7		96	70	< 5	60	372	60	25	43.1	99.4	9.45	35.4	5.8

(*continued on next page*)

Table 1 (*continued*)

Analyte Symbol				% SiO2	% Al2O3	% TiO2	% Fe2O3(T)	% Fe	% FeO	% MnO	% Mn	% MgO	% CaO	% Ba	% Na2O
Detection Limit				0.01	0.01	0.001	0.01	0.01	0.1	0.001	0.01	0.01	0.01	3 ppm	0.01
Analysis Method				FUS-ICP	FUS-ICP	FUS-ICP	Calculated	FUS-ICP	TITR	Calculated	FUS-XRF	FUS-ICP	FUS-ICP	FUS-ICP	FUS-ICP
COR 62	Urucum-MMX	Mn-2, Fig. 7	81cry + 19 bra + holl	39	60	74	70	346	60	15	24.2	62.3	5.64	22	4.1
COR 61L	Urucum-MMX	Mn-2, Fig. 7	90 cry+ 10 hmt	15	30	< 5	60	456	40	19	23.6	31	5.52	20.7	3.9
COR 61P	Urucum-MMX	Mn-2, Fig. 7	93 cry + 7 hmt	24	30	< 5	60	430	40	21	22.1	26.7	4.96	18.5	3.5
COR 60	Urucum-MMX	Mn-2, Fig. 7	hmt + cry	73	50	< 5	60	351	70	25	41.2	57.4	7.54	28	5.1
COR 59	Urucum-MMX	Mn-2, Fig. 7	hmt + cry- + holl	57	30	< 5	70	215	60	15	26.7	56.1	5.35	21.2	4.8
COR 79	Urucum-MMX	Fe, Fig. 7	hmt + qz	61	< 10	< 5	< 30	59	< 20	< 2	14.4	21.6	4.12	17.1	3.1
COR 07	Figueirinha	Mn-1, Fig. 15	63 bra (clastic) + 4 qz + 10 ab + 10 kao + 13 dol	71	20	7	50	> 1000	160	21	22.9	41.6	4.99	18.7	3.5
COR 06	Figueirinha	Mn-1, Fig. 15	cry + holl	17	70	8	40	> 1000	110	31	39.3	41.1	7.45	27.5	5.3
Pto 51	Figueirinha	Mn-1, Fig. 15	65 bra (clastic)+ 4 kao + 32 ply	104	30	9	70	> 1000	230	14	19.8	44	4.68	16.9	3.2
COR 04	Figueirinha	Mn-1, Fig. 15	87 hmt + 13 qz	53	30	6	40	484	380	36	20.7	44.1	5.54	23.6	4.9
COR 02	Figueirinha	Mn-1, Fig. 15	24 hmt + 42 qz + 25 mc + 8 alb	86	30	11	< 30	378	150	14	28.4	49.6	6.38	25	4.9
COR 09a	Figueirinha	Mn-1, Fig. 15	60 cry + 40 holl		70	< 5	70	899	190	12	31.4	51.6	4.44	15.3	2.7
COR 09b	Figueirinha	Mn-1, Fig. 15	75 bra (clastic)+ 25 mc	92	100	27	30	> 1000	140	22	16.5	22.3	4.91	19.9	4.1
COR 10	Figueirinha	Mn-1, Fig. 15	32 bra (clastic)+ 37 qz + 26 mcc + 2 ank	71	50	9	< 30	549	120	16	10.9	27.4	3.31	14.2	2.8
COR 12	Figueirinha	Mn-1, Fig. 15	hmt + qz- + kao + - mc	98	< 10	23	90	409	260	9	17.6	43.9	5.13	20.4	3.9
COR 35	São Domingos	Mn-1, Fig. 15	hmt + qz	125	< 10	< 5	< 30	148	30	36	24.3	41.5	8.05	33.8	7.4
COR 32	São Domingos	Mn-1, Fig. 15	12 hmt + 60 holl + 28 qz	35	20	6	< 30	> 1000	20	15	34.3	47.4	5.6	19	3

(*continued on next page*)

Table 1 (*continued*)

Analyte Symbol				% SiO2	% Al2O3	% TiO2	% Fe2O3(T)	% Fe	% FeO	% MnO	% Mn	% MgO	% CaO	% Ba	% Na2O
Detection Limit				0.01	0.01	0.001	0.01	0.01	0.1	0.001	0.01	0.01	0.01	3 ppm	0.01
Analysis Method				FUS-ICP	FUS-ICP	FUS-ICP	Calculated	FUS-ICP	TITR	Calculated	FUS-XRF	FUS-ICP	FUS-ICP	FUS-ICP	FUS-ICP
COR 33	São Domingos	Mn-1, Fig. 15	9 hmt + 43 cry + 9 bra (clastic)+ 11qz + 28 mc	58	10	6	30	> 1000	70	22	36	64.3	7.79	29.7	5.9
COR 31	São Domingos	Mn-1, Fig. 15	hmt + qz	103	20	9	< 30	427	150	21	18.7	34.4	5.25	21.7	4.8
COR 30	São Domingos	Mn-1, Fig. 15	12 hmt + 75 hol + 13 qz + ? pyr		< 10	< 5	< 30	952	60	4	7.1	9.3	1.41	4.9	1.1
COR 65	MMX	Mn-1, Fig. 15	hmt + cry- + holl + q-z	103	180	32	60	514	590	34	24.3	118	8.7	34.9	8.2
COR 23	Rabicho	Mn-1, Fig. 15	19 hmt + 63 pyr + 17 qz	69	110	15	60	517	680	60	38.1	74.8	9.18	33.8	7.1
COR 26	Rabicho	Mn-1, Fig. 15	cry + pyr- + qz	220	390	6	110	> 1000	2110	146	22.6	112	8.73	39.8	12.8
Pto 48	Rabicho	Mn-1, Fig. 15	65 hmt + 34 qz	8	< 10	< 5	< 30	37	< 20	26	12.1	23.7	3.55	15	3
Pto 50	Rabicho	Mn-1, Fig. 15		75	30	13	40	224	130	16	19.5	41.5	5.6	22.8	4.4
COR 28	Jacadigo	Mn-1, Fig. 15			110	13	40	326	420	26	8.9	18.6	2.26	10.1	2.5

Analyte Symbol	% K2O	% P2O5	% Cr2O3	% C-Total	% LOI	% Total	ppm Zr	ppm Cu	ppm Pb	ppm Zn	ppm Co	ppm Ni	ppm Y	ppm La	ppm Ce
Detection Limit	0.01	0.01	0.005	0.01	T = 1000°C		5	10	5	30	1	20		0.1	0.1
Analysis Method	FUS-ICP	FUS-ICP	FUS-XRF	CS			FUS-MS	FUS-MS	FUS-MS	FUS-MS	FUS-MS	FUS-MS		FUS-MS	FUS-MS
Sample															
COR 74W	0.24	0.06		0.01	0.87	100.81	14	< 10	< 5	< 30	15	< 20	< 2	17.5	29.6
COR 73W	< 0.01	0.12		< 0.01	0.25	100.66	11	< 10	< 5	< 30	41	< 20	< 2	10.9	18.3
COR 72W	< 0.01	0.09		< 0.01	0.25	99.23	23	< 10	< 5	< 30	43	< 20	< 2	18	28.7
COR 71W	< 0.01	0.11		< 0.01	0.27	100.60	24	< 10	< 5	< 30	53	< 20	< 2	15.3	23.7
COR 70W	< 0.01	0.1		< 0.01	0.27	99.65	33	< 10	< 5	< 30	59	< 20	< 2	22.3	36.4
COR 74D	0.06	0.07	< 0.01	< 0.01	0.5	99.89	28	< 10	< 5	< 30	9	< 20	9	4.5	8
COR 73D	0.01	0.16	< 0.01	0.01	0.28	99.34	25	< 10	< 5	< 30	44	< 20	14	11.8	19.1
COR 72D	< 0.01	0.15	< 0.01	< 0.01	0.24	99.90	28	< 10	< 5	< 30	37	< 20	13	10.8	19.5
COR 71D	< 0.01	0.17	< 0.01	< 0.01	0.27	99.27	22	< 10	< 5	< 30	47	< 20	23	11.5	20.3
COR 70D	< 0.01	0.16	< 0.01	< 0.01	0.28	99.80	28	< 10	< 5	< 30	39	< 20	15	11.2	20.5
COR 14A	< 0.01	0.07	< 0.01	< 0.01	4.44	100.51	8	< 10	< 5	< 30	63	< 20	5	29.3	56
COR 74	0.078	0.07	< 0.01	< 0.01	0.54	99.99	11	< 10	< 5	< 30	10	< 20	7	5.8	10.2
COR 73	< 0.01	0.16	< 0.01	< 0.01	0.28	99.48	24	< 10	< 5	< 30	44	< 20	12	11.7	19.0
COR 72	< 0.01	0.14	< 0.01	< 0.01	0.24	99.80	29	< 10	< 5	< 30	38	< 20	11	11.9	20.9
COR 71	< 0.01	0.16	< 0.01	< 0.01	0.27	99.47	28	< 10	< 5	< 30	48	< 20	12	12.1	20.8

(*continued on next page*)

Table 1 (*continued*)

Analyte Symbol	% K2O	% P2O5	% Cr2O3	% C-Total	% LOI	% Total	ppm Zr	ppm Cu	ppm Pb	ppm Zn	ppm Co	ppm Ni	ppm Y	ppm La	ppm Ce
Detection Limit	0.01	0.01	0.005	0.01	T = 1000°C		5	10	5	30	1	20		0.1	0.1
Analysis Method	FUS-ICP	FUS-ICP	FUS-XRF	CS			FUS-MS	FUS-MS	FUS-MS	FUS-MS	FUS-MS	FUS-MS		FUS-MS	FUS-MS
COR 70	< 0.01	0.15	< 0.01	< 0.01	0.28	99.77	27	< 10	< 5	< 30	43	< 20	17	13.4	23.7
COR 14	< 0.01	0.17	< 0.01	< 0.01	0.33	100.18	24	< 10	< 5	< 30	72	< 20	< 2	9.9	18
COR 69	< 0.01	0.08			0.25	99.67	17	< 10	< 5	< 30	61	< 20	< 2	8	12.6
COR 68	0.08	0.06			0.26	99.99	33	< 10	< 5	< 30	57	< 20	12	14.8	21.2
COR 67	0.55	0.12	< 0.01		1.04	100.43	40	20	< 5	< 30	24	< 20	< 2	39.3	62.3
COR 66	0.49	0.07			0.71	100.98	88	< 10	< 5	< 30	157	50	< 2	44	93.1
Pto 26W	< 0.01	0.09			0.3	99.85	15	< 10	< 5	< 30	36	< 20	15	7.1	13.1
Pto 26D	0.03	0.14	< 0.01		0.35	99.45	21				33	< 20	15	7.4	14.8
Pto 18W	< 0.01	0.09			0.24	100.33	17	< 10	< 5	< 30	48	< 20	< 2	14.1	27.3
Pto 18D	0.02	0.11	< 0.01		0.39	98.90	16	< 10	< 5	< 30	32	< 20	20	8.2	16.9
COR 21	0.1	0.25			1.38	99.98	55	< 10	< 5	< 30	57	< 20	< 2	14.9	29.7
COR 22	0.48	0.303	< 0.005		1.93	100.90	31	20	< 5	< 30	112	< 20	13	8.4	20.4
COR 20	1.64	0.475	< 0.005	< 0.01	6.02	97.95	48	40	6	40	189	70	25	15.9	38.9
COR 16P	2.59	0.533	< 0.005	< 0.01	10.1	93.81	44	70	< 5	50	229	20	24	29	159
COR 16M	1.85	0.5	< 0.005	< 0.01	9.64	93.02	27	60	< 5	40	228	< 20	22	24.5	118
COR 17	2.17	0.499	< 0.005	< 0.01	9.4	94.85	42	40	< 5	40	200	< 20	19	38.8	201
COR 48L	1.68	0.526	< 0.005	< 0.01	10.94	93.25		30	6	40	230	30	17	20.2	44.7
COR 48P	2.13	0.625	< 0.005	< 0.01	11.55	92.74		10	< 5	< 30	216	30	11	16.5	5.7
COR 47W	0.03	0.05			0.39	98.76	5	10	< 5	< 30	29	< 20	< 2	8.7	16.2
COR 47D	0.03	0.09	< 0.01		0.39	99.92	7	< 10	< 5	< 30	34	< 20	7	6.6	12.5
COR 46W	0.01	0.08			0.29	100.60	8	< 10	< 5	< 30	31	< 20	< 2	8.4	16.9
COR 46D	0.02	0.07	< 0.01		0.41	100.55	9	< 10	< 5	< 30	29	< 20	9	6.5	12.8
COR 45	0.09	0.06			2.43	98.08	122	< 10	< 5	< 30	108	70	< 2	11.5	24
COR 37	0.01	0.07	< 0.01		0.4	99.74	85	< 10	< 5	< 30	100	50	11	19.7	39.1
COR 44	1.99	0.674	< 0.005		11.66	95.10	36	50	6	40	486	< 20	96	14.5	25.6
COR 41	3.08	0.537	< 0.005		9.49	92.10	29	20	< 5	40	477	30	50	19.4	29.5
COR 36a	3.54	0.326	< 0.005	0.66	10.85	91.50	6	30	< 5	60	371	40	24	33.1	38.5
COR 43	1.83	0.397	< 0.005	< 0.01	10.55	92.91	31	10	< 5	50	418	< 20	15	18.8	24.4
COR 36b	3.74	0.271	< 0.005		9.9	89.87	8	20	< 5	40	414	40	14	25	28.9
COR-75	0.5	0.397	< 0.005		12.46	94.53	38	20	< 5	60	512	40	35	21.8	27.7
COR 42	2.81	0.304	< 0.005	< 0.01	8.91	92.75	24	10	< 5	< 30	399	< 20	13	20.5	22.9
COR 40	2.51	0.199	< 0.005		7.05	95.03	90	< 10	5	< 30	188	60	19	29.6	47.3
COR 39	0.06	0.04			1.39	100.53	120	< 10	< 5	< 30	102	40	< 2	11.2	19.6
COR 38	0.46	0.06			1.16	100.80	80	< 10	< 5	< 30	50	< 20	< 2	9.1	16.9
COR 76	< 0.01	0.12	< 0.01	< 0.01	0.36	100.34	10	< 10	< 5	< 30	17	< 20	11	13.3	21.6
COR 77	0.01	0.12	< 0.01		0.44	99.22	9	< 10	< 5	< 30	19	< 20	15	17.6	26.9
COR 63W	0.08	0.04			2.71	99.21	82	< 10	7	< 30	80	90	< 2	11.5	22.3
COR 63D	0.11	0.08	< 0.01		2.82	100.01	72	< 10	29	< 30	92	90	10	10.3	19.2
COR 78	1.86	0.701	< 0.005		12.31	96.43	96	70	< 5	60	372	60	25	43.1	99.4
COR 62	1.68	0.265	< 0.005		9.58	94.06	39	60	74	70	346	60	15	24.2	62.3
COR 61L	1.12	0.523	< 0.005	0.09	11.23	93.50	15	30	< 5	60	456	40	19	23.6	31
COR 61P	1.08	0.495	< 0.005	0.2	12.27	94.08	24	30	< 5	60	430	40	21	22.1	26.7
COR 60	1.59	0.62	< 0.005	< 0.01	12.15	96.20	73	50	< 5	60	351	70	25	41.2	57.4
COR 59	1.67	0.63			9.62	98.85	57	30	< 5	70	215	60	15	26.7	56.1
COR 79	0.19	0.05		< 0.01	0.59	100.82	61	< 10	< 5	< 30	59	< 20	< 2	14.4	21.6
COR 07	2.34	0.242	< 0.005		2.68	100.11	71	20	7	50	> 1000	160	21	22.9	41.6
COR 06	1.25	0.203	< 0.005	0.02	5.85	93.95	17	70	8	40	> 1000	110	31	39.3	41.1
Pto 51	2.86	0.229	< 0.005		2.06	100.50	104	30	9	70	> 1000	230	14	19.8	44
COR 04	1.4	0.6	< 0.01		0.33	100.14	53	30	6	40	484	380	36	20.7	44.1

(*continued on next page*)

Table 1 (*continued*)

Analyte Symbol	% K2O	% P2O5	% Cr2O3	% C-Total	% LOI	% Total	ppm Zr	ppm Cu	ppm Pb	ppm Zn	ppm Co	ppm Ni	ppm Y	ppm La	ppm Ce
Detection Limit	0.01	0.01	0.005	0.01	T = 1000°C		5	10	5	30	1	20		0.1	0.1
Analysis Method	FUS-ICP	FUS-ICP	FUS-XRF	CS			FUS-MS	FUS-MS	FUS-MS	FUS-MS	FUS-MS	FUS-MS		FUS-MS	FUS-MS
COR 02	1.81	0.74			2.26	99.86	86	30	11	< 30	378	150	14	28.4	49.6
COR 09a	4.86	0.26	< 0.005	< 0.01	8.38	89.62		70	< 5	70	899	190	12	31.4	51.6
COR 09b	1.27	0.195	< 0.005	< 0.01	6.45	95.56	92	100	27	30	> 1000	140	22	16.5	22.3
COR 10	1.18	0.377	< 0.005		2.86	99.70	71	50	9	< 30	549	120	16	10.9	27.4
COR 12	1.47	0.3			4.24	98.34	98	< 10	23	90	409	260	9	17.6	43.9
COR 35	0.28	0.7	< 0.01		2.55	99.05	125	< 10	< 5	< 30	148	30	36	24.3	41.5
COR 32	4	0.241	< 0.005		7.76	94.63	35	20	6	< 30	> 1000	20	15	34.3	47.4
COR 33	3.72	0.282	< 0.005	< 0.01	7.34	95.33	58	10	6	30	> 1000	70	22	36	64.3
COR 31	0.95	0.22	< 0.01		4.85	98.90	103	20	9	< 30	427	150	21	18.7	34.4
COR 30	3.96	0.139	< 0.005		8.09	94.35		< 10	< 5	< 30	952	60	4	7.1	9.3
COR 65	2.11	0.549	< 0.005		8.83	97.70	103	180	32	60	514	590	34	24.3	118
COR 23	1.18	0.596	0.026		12.44	94.21	69	110	15	60	517	680	60	38.1	74.8
COR 26	1.22	0.271	< 0.005	0.01	10.98	100.35	220	390	6	110	> 1000	2110	146	22.6	112
Pto 48	0.01	0.13	< 0.01		0.38	100.08	8	< 10	< 5	< 30	37	< 20	26	12.1	23.7
Pto 50	0.37	0.18	< 0.01		2.7	99.41	75	30	13	40	224	130	16	19.5	41.5
COR 28	2.81	0.267	< 0.005		10.71	91.55		110	13	40	326	420	26	8.9	18.6

Analyte Symbol	ppm Eu	ppm Gd	ppm Tb	ppm Dy	ppm Ho	ppm Er	ppm Tm	ppm Yb	ppm Lu	Sum REE	Ce/Ce*	LaN/CeN	Eu/Eu*	Zn/Co	Y/Ho
Detection Limit	0.05	0.1	0.1	0.1	0.1	0.1	0.05	0.1	0.01						
Analysis Method	FUS-MS	FUS-MS	FUS-MS	FUS-MS	FUS-MS	FUS-MS	FUS-MS	FUS-MS	FUS-MS						
Sample															
COR 74W	0.67	2.4	0.4	2.1	0.4	1.2	0.18	1.3	0.21	81.42	0.78	1.27	1.05		
COR 73W	0.5	2	0.3	1.9	0.4	1.3	0.2	1.4	0.23	54.1	0.70	1.35	1.11		
COR 72W	1	3.9	0.5	3.1	0.6	1.6	0.24	1.6	0.26	88.01	0.68	1.32	1.04		
COR 71W	0.81	3.4	0.5	3.3	0.7	2	0.3	2	0.32	78.33	0.72	1.33	1.08		
COR 70W	1.13	4.6	0.7	3.8	0.7	2	0.29	1.9	0.32	112.93	0.72	1.22	1.12		
COR 74D	0.29	1.1	0.2	1.1	0.3	0.9	0.15	1.1	0.19	26.49	0.75	1.28	1.11		30
COR 73D	0.58	2.4	0.4	2.1	0.4	1.3	0.19	1.2	0.21	57.63	0.65	1.39	1.05		35
COR 72D	0.75	3	0.4	2.5	0.5	1.3	0.2	1.3	0.22	59.32	0.70	1.21	0.97		26
COR 71D	0.67	3.1	0.5	3.4	0.7	2.2	0.31	2.3	0.37	66.24	0.76	1.19	1.03		33
COR 70D	0.81	3.5	0.5	2.7	0.5	1.5	0.23	1.6	0.25	65.46	0.71	1.18	1.07		30
COR 14A	1.59	9.3	2	16.3	4.4	15.9	2.74	19.4	3.25	201.83	0.89	1.13	1.10		1
COR 74	0.3	1.2	0.2	1.2	0.3	0.9	0.2	1.1	0.2	31.98	0.72	1.23	1.10		23
COR 73	0.6	2.4	0.4	2.1	0.4	1.3	0.2	1.2	0.2	57.28	0.73	1.33	1.08		30
COR 72	0.8	3.1	0.4	2.6	0.5	1.3	0.2	1.3	0.2	63.62	0.75	1.23	1.11		21
COR 71	0.7	3.1	0.5	3.4	0.7	2.2	0.3	2.3	0.4	68.05	0.71	1.25	0.99		17
COR 70	0.9	3.7	0.5	2.9	0.5	1.6	0.2	1.7	0.3	74.95	0.70	1.22	1.06		31
COR 14	0.58	2.7	0.4	2.7	0.5	1.6	0.23	1.6	0.27	55	0.78	1.19	1.02		
COR 69	0.43	1.8	0.3	1.6	0.4	1.1	0.17	1.2	0.2	41.83	0.65	1.37	1.04		
COR 68	0.86	3.1	0.4	1.8	0.3	0.8	0.11	0.8	0.13	74.44	0.54	1.50	1.11		40
COR 67	1.45	5.2	0.6	3.1	0.5	1.3	0.17	1.1	0.18	173.9	0.71	1.36	1.11		
COR 66	2.32	8.6	1.1	5.6	0.9	2	0.25	1.6	0.22	244.19	0.82	1.17	0.94		
Pto 26W	0.33	1.8	0.3	2	0.5	1.4	0.21	1.4	0.24	39.19	0.81	1.08	0.96		30
Pto 26D	0.42	2.1	0.3	2.3	0.5	1.4	0.22	1.5	0.23	44.62	0.68	1.11	1.06		30
Pto 18W	1.07	4.8	0.7	3.8	0.7	2	0.28	1.9	0.31	89.35	0.77	1.05	1.01		
Pto 18D	0.64	2.8	0.5	2.9	0.6	1.9	0.28	1.9	0.3	54.16	0.45	1.08	1.06		33

(*continued on next page*)

Table 1 (*continued*)

Analyte Symbol	% K2O	% P2O5	% Cr2O3	% C-Total	% LOI	% Total	ppm Zr	ppm Cu	ppm Pb	ppm Zn	ppm Co	ppm Ni	ppm Y	ppm La	ppm Ce
Detection Limit	0.01	0.01	0.005	0.01	T = 1000°C		5	10	5	30	1	20		0.1	0.1
Analysis Method	FUS-ICP	FUS-ICP	FUS-XRF	CS			FUS-MS	FUS-MS	FUS-MS	FUS-MS	FUS-MS	FUS-MS		FUS-MS	FUS-MS
COR 21	4.51	25.1	4.2	20.1	2.1	3.4	0.36	2	0.28	175.97	1.12	0.89	1.01		
COR 22	0.34	1.4	0.3	2	0.5	1.5	0.21	1.3	0.18	48.57	1.13	0.88	1.04	0.36	26
COR 20	0.97	5	1.1	7.5	1.4	3.5	0.51	3.6	0.52	101.86	2.27	0.39	1.02		18
COR 16P	1.79	6.1	1	5.5	1.1	3.2	0.52	3.7	0.61	264.47	1.83	0.45	1.14		22
COR 16M	1.73	6	0.9	5.4	1	2.9	0.47	3.6	0.61	216.43	2.15	0.42	1.11		22
COR 17	2.26	7.4	1	5.3	0.9	2.9	0.46	3.2	0.48	333.6	1.15	0.97	1.14		21
COR 48L	0.54	2.3	0.4	2.6	0.6	2.1	0.35	2.5	0.42	99.13	0.22	6.24	0.99		28
COR 48P	0.23	1	0.2	1.3	0.3	1.3	0.21	1.6	0.26	40.11	0.84	1.16	0.92		37
COR 47W	0.53	2.6	0.4	2.2	0.4	1	0.14	0.9	0.14	46.44	0.82	1.14	1.03		
COR 47D	0.46	2.2	0.3	1.8	0.3	0.7	0.1	0.7	0.1	36.71	0.74	1.07	1.02		23
COR 46W	0.72	2.9	0.4	2	0.3	0.9	0.13	0.8	0.13	51.79	0.79	1.09	1.12		
COR 46D	0.47	2.5	0.4	1.9	0.3	0.8	0.12	0.8	0.13	38.91	0.77	1.03	0.95	0.00	30
COR 45	0.69	2.8	0.4	2.1	0.4	1.2	0.2	1.4	0.23	69.52	0.74	1.09	1.02		
COR 37	1.77	6.4	0.8	4.1	0.6	1.3	0.15	1	0.15	117.61	0.87	1.22	1.17	0.40	18
COR 44	0.61	3.5	0.7	6.2	2	11.3	4.01	44.6	10.4	142.03	0.70	1.42	0.90	0.08	48
COR 41	0.75	3.3	0.5	3.7	1.3	4.7	0.74	5.3	0.93	98.09	0.66	1.85	0.97	0.13	38
COR 36a	0.78	3.7	0.7	5.4	1.1	2.9	0.42	2.7	0.4	120.34	0.66	1.66	0.94		22
COR 43	0.65	2.8	0.5	3.1	0.7	2.2	0.38	2.9	0.45	79.24	0.69	1.86	1.01		21
COR 36b	0.48	2.2	0.4	3.1	0.7	1.9	0.28	2	0.3	84.94	0.65	1.70	0.98		20
COR-75	0.89	4.5	0.8	5.5	1.2	4	0.65	4.6	0.73	98.21	0.59	1.93	1.00		29
COR 42	0.55	2.3	0.4	2.5	0.6	1.9	0.35	3.2	0.58	77.67	0.80	1.35	1.03		22
COR 40	0.82	3.1	0.4	2.8	0.7	2.2	0.36	2.6	0.39	125.7	0.80	1.23	1.05		27
COR 39	0.47	2.2	0.3	2.1	0.5	1.6	0.26	1.9	0.33	57.04	0.89	1.16	0.96		
COR 38	0.31	1.5	0.3	1.9	0.4	1.5	0.25	1.8	0.28	46.32	0.72	1.33	0.95		
COR 76	0.62	2.7	0.4	1.8	0.3	0.9	0.13	1	0.16	63.37	0.67	1.41	1.01		37
COR 77	0.81	3.8	0.5	2.5	0.4	1.3	0.2	1.4	0.23	83.1	0.83	1.11	0.96		38
COR 63W	0.47	2	0.3	1.8	0.4	1	0.15	1	0.15	59.7	0.77	1.16	0.98		
COR 63D	0.47	2	0.3	1.9	0.4	1.1	0.16	1	0.16	55.13	1.16	0.93	0.98		25
COR 78	1.16	4.6	0.7	4.4	0.9	3	0.48	3.5	0.58	212.47	1.24	0.84	1.03		28
COR 62	0.92	3.4	0.5	3	0.6	1.7	0.27	1.9	0.29	130.82	0.64	1.64	1.13		25
COR 61L	0.79	3.7	0.6	3.5	0.7	2.1	0.32	2.2	0.37	99	0.60	1.78	0.95	0.65	27
COR 61P	0.72	3.3	0.5	3.3	0.7	2.1	0.34	2.5	0.42	89.64	0.76	1.55	0.97	0.19	30
COR 60	1.05	4.3	0.6	3.8	0.8	2.5	0.37	2.7	0.44	155.8	1.08	1.03	1.03	0.17	31
COR 59	1.1	4.8	0.8	5.4	1.1	3.6	0.54	3.6	0.57	135.66	0.63	1.44	1.05		14
COR 79	0.72	2.7	0.3	1.6	0.2	0.6	0.06	0.4	0.06	66.96	0.92	1.19	1.14		
COR 07	0.74	3.6	0.6	3.7	0.7	2.2	0.35	2.3	0.37	106.25	0.57	2.06	0.95		30
COR 06	1.12	4.8	0.8	5.1	1.1	3.3	0.5	3.4	0.55	141.32	1.10	0.97	1.02		28
Pto 51	0.68	2.9	0.5	2.9	0.6	1.9	0.31	2.2	0.35	100.92	0.91	1.01	1.02		23
COR 04	1.13	5.4	0.9	5.4	1.1	3.4	0.51	3.8	0.64	121.12	0.85	1.23	1.00		33
COR 02	1.04	4.3	0.7	4.3	0.9	2.8	0.43	2.9	0.45	132.1	1.02	1.31	1.04		16
COR 09a	0.63	2.4	0.4	2.4	0.5	1.5	0.24	1.8	0.29	115.6	0.56	1.59	1.13		24
COR 09b	1	3.9	0.6	3.6	0.7	2	0.29	1.9	0.32	82.02	1.00	0.86	1.14	0.00	31
COR 10	0.69	3	0.5	2.5	0.5	1.5	0.21	1.4	0.22	69.13	1.06	0.86	1.09	0.19	32
COR 12	0.91	3.6	0.5	3.4	0.7	2.1	0.34	2.3	0.37	105.15	0.65	1.26	1.11		13
COR 35	1.52	7.5	1.1	6.7	1.3	3.4	0.47	3.1	0.46	140.6	0.82	1.56	0.93	0.00	28
COR 32	0.64	2.7	0.4	2.5	0.5	1.7	0.25	1.7	0.26	119.95	0.90	1.21	1.03		30
COR 33	1.12	4.8	0.7	4.2	0.8	2.4	0.36	2.3	0.37	160.74	0.78	1.17	0.96		28
COR 31	1.01	4.7	0.7	3.8	0.7	2.1	0.31	2.2	0.34	100.71	0.71	1.65	0.97		30
COR 30	0.23	0.9	0.2	1	0.2	0.7	0.11	0.8	0.13	28.08	0.83	1.02	1.06		20

(*continued on next page*)

Table 1 (*continued*)

Analyte Symbol	% K2O	% P2O5	% Cr2O3	% C-Total	% LOI	% Total	ppm Zr	ppm Cu	ppm Pb	ppm Zn	ppm Co	ppm Ni	ppm Y	ppm La	ppm Ce
Detection Limit	0.01	0.01	0.005	0.01	T = 1000°C		5	10	5	30	1	20		0.1	0.1
Analysis Method	FUS-ICP	FUS-ICP	FUS-XRF	CS			FUS-MS	FUS-MS	FUS-MS	FUS-MS	FUS-MS	FUS-MS		FUS-MS	FUS-MS
COR 65	1.93	7	1.2	6.7	1.3	4	0.64	4.7	0.77	222.34	1.82	0.44	1.17	0.14	26
COR 23	1.48	5	0.8	6.2	2.5	10.9	1.95	14.5	2.04	208.35	0.95	1.10	1.13		24
COR 26	3.34	15.3	2.8	18.5	4.5	16	2.72	19.8	3.28	282.17	1.64	0.43	1.08		32
Pto 48	0.68	3	0.5	3	0.6	2.1	0.31	2.1	0.37	70.01	0.80	1.10	1.04		43
Pto 50	0.86	3.5	0.5	2.9	0.6	1.8	0.3	2.3	0.39	106.95	0.90	1.01	1.00		27
COR 28	0.55	2.8	0.5	3.4	0.8	2.6	0.44	3.2	0.54	57.19	0.90	1.03	0.95		33

Sample names-COR.....W = White, or silicious part; COR.....D = Dark or ferruginous part; COR.....L = Laminated rock; COR.....P = Porous; COR....M = Massive.
Abbreviations: hmt = hematite; qz = quartz, pyr = pyrolusite; cry = cryptomelane; hol = hollandite; bra = braunite, kao = kaolinite; cht = chert; ab = albite,; ply = palygorskite; dol = dolomite, gth = goethite; mc = muscovite; FUS-ICP = Fusion -Induced coupled plasma; TITR = titration; FUS-XRF = Fusion-X-ray fluorescence; FUS-MS = fusion - Mass Spectrometer; CS = Organic carbon and sulfur.

sandstones consisting of 30–40 vol% hematite, 60–70 vol% quartz, and 1–5 vol% clay minerals. In the Jacadigo Mine, massive pyrolusite concretions in the ores consist of 60–76% MnO, 0.5–1% Fe_2O_3, 0.2–0.5% SiO_2, 1–3% Na_2O, 0.1–0.3% K_2O, and 0.11% Ba.

The conglomerate that commonly overlies the Upper Mn-1 ore layer is polymictic and contains primarily granite clasts with dimensions ranging from millimeter- to meter-scale (Fig. 6A), with subordinate amounts of gneiss, quartzite, and felsic volcanic rock clasts (Fig. 6G). The matrix is arkosic ferruginous, with angular fragments of rock, quartz, limpid plagioclase and microcline, hematite, and chert, and is cemented by hematite.

4.3. Layers Mn-2 and Mn-3

Layers Mn-2 and Mn-3 consist of massive manganese ore hosted in clastic and clastic–chemical ferruginous rocks. Their compositions, textures, and structures are similar (Fig. 7), and they contain numerous kremydilites with diameters ranging between 5 and 20 cm. The host iron-rich layers (Fig. 7) are laminated, with parallel or wavy laminations, and contain numerous amygdalites. Host rock textures range between conglomerate and chert, and they contain predominantly quartz fragments with lesser feldspar and chert. In rocks with grain sizes ranging between silt and coarse sand, and in the sandy, arkosic conglomerate matrix, the grains are supported by the matrix, which consists of 10–70 vol% hematite and 20–70 vol% red chert that is typically recrystallized to white quartz (Fig. 8C–D). The proportion of fragments varies between 2 and 60 vol%, and the rock composition is 50–86% Fe_2O_3, 9–45% SiO_2, 0–2% MnO, 2–5% Al_2O_3, and 0.2–0.4% TiO_2 (Table 1).

The manganese ore is micronodular (Figs. 8E–F and 9A–I) comprising spherical, massive (Figs. 8E–F and 9C–D) or zoned (Fig. 9A–B, I, and 10.6A) micronodules with diameters between 10 and 300 μm and cemented by a cryptocrystalline matrix. Where the ore is laminated, the nodules are amalgamated and/or amalgamated and flattened (Fig. 10.1A). The individual micronodules tend to be near the kremydilite cores (Fig. 9A, B, F, and G). The nodules are typically composed solely of cryptomelane and are cemented by cryptomelane–hematite (Fig. 9C–E). The millimeter-scale nodules are composed of amalgamated micrometric, massive or zoned nodules (Fig. 9G–I), giving the appearance that the larger (millimeter-scale) nodules are massive.

Near the kremydilite cores, the composition is 40–70% MnO, 9–21% Fe_2O_3, 0–3% Al_2O_3, and 0–2% SiO_2; whereas, outside the kremydilites, the ore compositions are 8–50% MnO and 8–35% Fe_2O_3 grading to 90–99% Fe_2O_3 and 1–10% SiO_2 in the wall rocks. All of the manganese ores contain iron and very little silica.

The textures of the kremydilites range from massive metallic (Figs. 10A and 11A) to microgranular porous (Fig. 12A). They typically contain various proportions of pore spaces and translucent, non-reflective, microcrystalline mineral clusters (dark spots under RL, Figs. 11B–I and 12E–I), which are particularly visible under RL with crossed nicols (white dots, Fig. 12B). The kremydilites are zoned structures (Fig. 8B, 10A, 11A, and 12A) consisting of 5 to 20 concentric zones comprising micronodules of cryptomelane (± hollandite ± carbonate) in an iron-manganiferous matrix. The thicknesses of these zones range from millimeters to centimeters, and the matrix volume varies between 0–1 vol%, where the nodules are flattened and amalgamated (e.g., zones 15 and 17; Fig. 10.1A), and 10–30 vol% (e.g., zone 14; Fig. 10.1A), where there are many individual nodules. Many of the kremydilites display pre-diagenetic discontinuities (Figs. 10A and 11A).

The massive (Figs. 9C–D and 10.4A) and zoned (Fig. 9E–I and 10.6A) micronodules are composed of cryptomelane and minor hollandite, with compositions of 79–84% MnO, 2–5% K_2O, and 1.0–2.5% BaO. The micronodule matrix consists of cryptocrystalline hematite and cryptomelane (Figs. 8E–F and 9D–E) in varying proportions. Rhodochrosite microcrystals and silica-rich carbonaceous matter infilling pore spaces are present in most layers as black dots (Fig. 10A, 11A, and 12A).

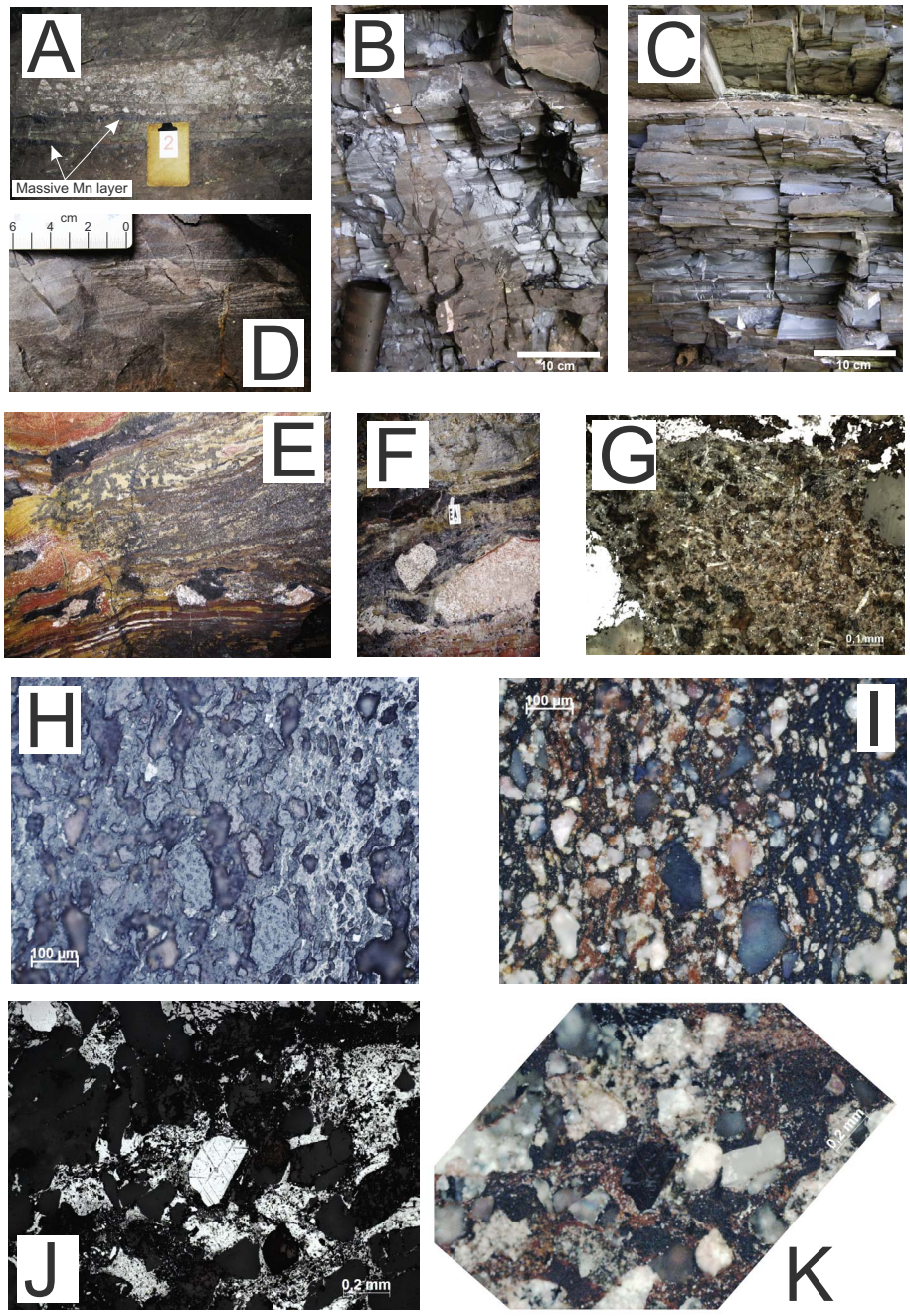

Fig. 6. Characteristics of layer Mn-1 in various mines. (A) Conglomerate with angular granite clasts overlying layer Mn-1 in the São Domingos Mine Upper Mn-1 layer. The contact is abrupt and flat. (B) Clastic–chemical, clayey, soft, laminated manganese ore from the São Domingos Upper Mn-1 layer. (C) Upper Mn-1 layer with amygdalites in the São Domingos Mine. (D) Fluvial channel cross-stratification preserved in the Lower Mn-1 (clastic–chemical ore) layer in the Figueirinha Mine. (E, F) Rocks and concretionary ores from the Rabicho and Morro Grande mines. (G) Fragment of volcanic rock from conglomerate overlying the Upper Mn-1 layer. (H-I) Photomicrographs of rock surrounding the amygdalites. The fragments are quartz and cryptomelane cemented by hematite and chert. (J, K) Photomicrographs of arkosic clastic–chemical rock located near and below the Lower Mn-1 layer. Note the fragments of twinned hematite (in the center of the images) and ferruginous chert, quartz, and feldspar cemented by hematite and chert. H, J under RL and //N; I, K under RL and xN.

Microcrystals of calcium, magnesium, and manganese carbonate are present in roughly rounded structures with ring-like sections (Fig. 10.1A–D) and merge with translucent microcrystalline clusters composed of silica-rich carbonaceous matter. Only in pores' carbonate were preserved from diagenesis, and the total carbonate content in the ore varies between 1 and 15%. (Figs. 10–12). Its composition is 1–35% Ca, 1–20% Mg, and 2–60% Mn, consistent with that of rhodochrosite (e.g. Fig. 10) and manganiferous calcite or dolomite (Fig. 10.1C), which always occur together with high concentrations of carbonaceous matter. The composition of the microcrystalline microclusters is 40–55% C, 30–41% SiO_2, and 5–25% MnO, and calcium, magnesium, and alumina are absent (points 2 and 3, Fig. 10.1D). Locally, they are devoid of silica and contain as much as 65% C and 35% Mn, also devoid of calcium, magnesium, and alumina (point 5, Fig. 10.1D).

After diagenesis, the kremydilites contain 1–3 vol% pore space, most in the core. The pores are cavities and holes with irregular or cylindrical shapes (Fig. 10.3A–B and 10.5A) that formed in a silico-manganiferous matrix whose composition is compatible with that of hausmannite and/or bixbyite (Fig. 10.4, points 5–8). They are discontinuously coated by clusters of rhodochrosite needles and meshs mixed with carbonaceous matter (Fig. 10.3A–D). Locally, inside the pores, there are groups of twisted objects resembling tubeworms, with lengths between 50 and 500 µm and diameters between 5 and 10 µm (Fig. 10.4A and 10.5A, 10.5C–D). Their composition is 60–92% C,

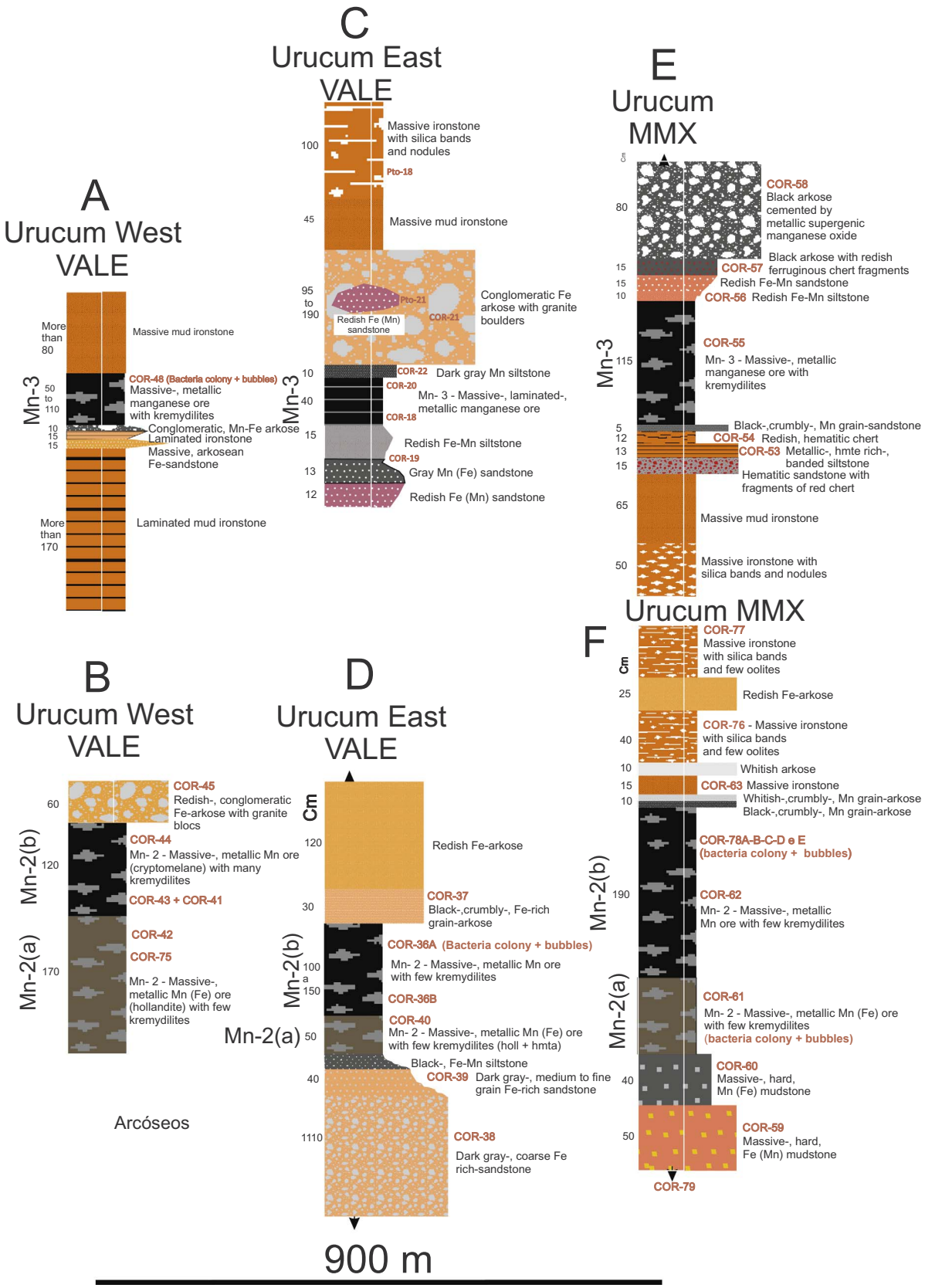

Fig. 7. Simplified stratigraphic columns for layers Mn-2 (lower part) and Mn-3: (A, B) on the west side of the VALLE-Urucum Mine; (C, D) on the east side of the VALE-Urucum Mine; and (E, F) in the MMX-Urucum Mine. The distance between the columns shown in (A) and (B) and those shown in (E) and (F) is 900 m.

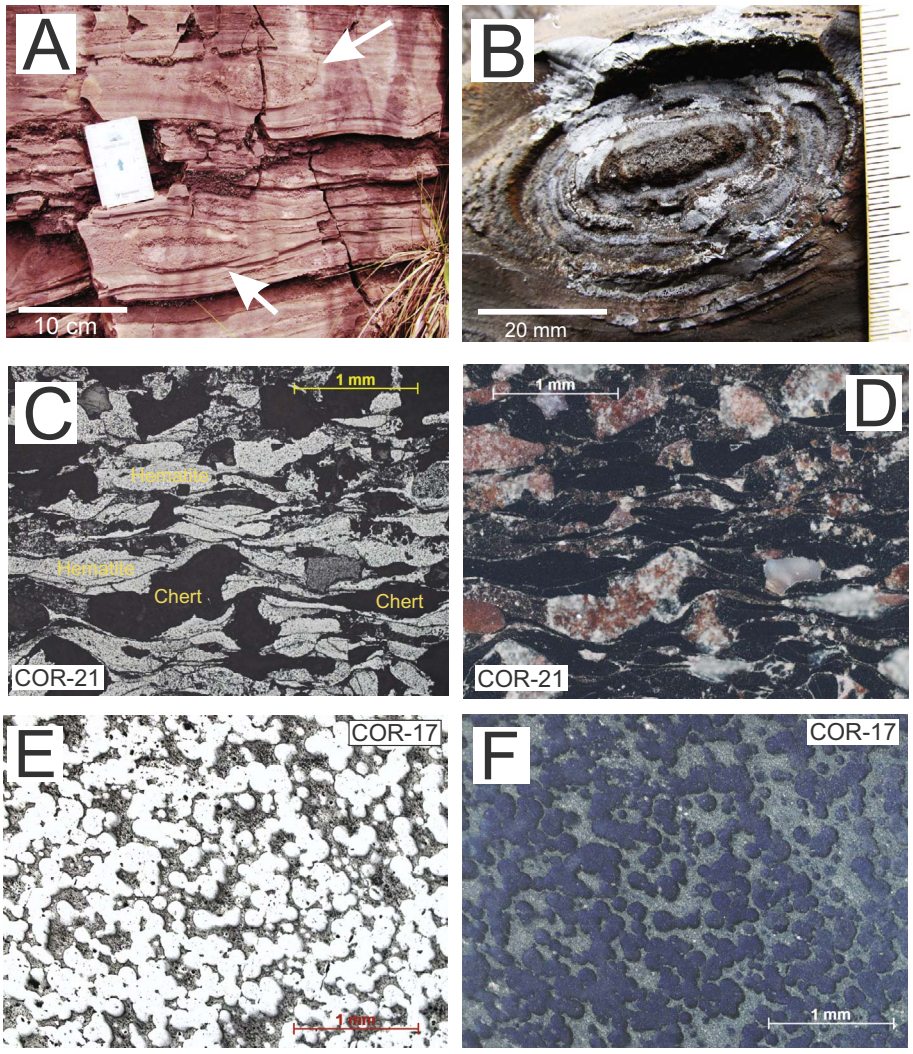

Fig. 8. Characteristics of massive manganese ore layers Mn-2 and Mn-3. (A) Amygdalites in layer Mn-2 (VALE-Urucum Mine). (B) Kremydilites in layer Mn-3 (VALE-Urucum Mine). (C, D) Photomicrographs of ferruginous chert hosting layers Mn-2 and Mn-3, consisting of micro-lenses of chert and hematite with irregular shapes. (E, F) Photomicrograph of micronodular massive ore in layer Mn-3 (MCR Mine). Photomicrographs in RL; C, E under //N; and D, F under xN.

4–38% MnO, and 1–15% SiO_2. Around the worm-like objects, there are also concentrations of rhodochrosite prismatic crystallite, 1–10 μm in length (Fig. 10.5C–E, points 1, 2, 5–8; and Fig. 11F), mesh-like structures, and spherical micronodules, with diameters of < 5 μm, composed of rhodochrosite, carbonaceous matter and cryptomelane with traces of hollandite (Fig. 10.4A and 10.6A, points 1–4). Although smaller, these micronodules are similar to those found in the interiors of the massive cryptomelane micronodules (Fig. 9F–I) constituting the massive ore.

The kremydilites are metallic and commonly contain internodular and/or intergranular gas bubble-shaped structures with diameters between 5 and 15 mm, either grouped close to the nucleus (Fig. 11A) or far apart but in the same stratigraphic horizon (Fig. 12A). The wrap surrounding the nucleus is metallic, massive, and consists of coalesced micronodules (Fig. 11G) of cryptomelane and contain little hollandite (Fig. 11B–C and G–I). Generally, they display microclusters of translucent rhodochrosite crystals (Fig. 11E–F) and are locally gray and porous (Fig. 11I). Inside the bubbles, the metallic portion is composed almost entirely of cryptomelane and carbonaceous matter (Fig. 11C, G, H, and I) with minor hollandite. Microclusters are locally phosphorus and aluminous, which is compatible with eosphorite [$MnAl(PO)_4(OH)_2$] (Fig. 11D–E). Some groups contain prismatic microcrystals (Fig. 11F and I–J), similar to the microbialites described above (Fig. 10.5E), and whose compositions are consistent with those of crandallite [$CaAl_3(PO_4)_2(OH)_5H_2O$]. These microcrystals are surrounded by hollandite and Ba-rich rhodochrosite (Fig. 11F). In the non-metallic portions (Fig. 11I–J, dark part) they are surrounded by carbonaceous matter.

On the west side of the VALE-Urucum Mine, the ore from layer Mn-2 contains granular, metallic, and porous kremydilites with bubbles positioned far from their nuclei but in the same stratigraphic horizon (Fig. 12A). The bubble wrap consists of metallic and massive cryptomelane (Fig. 12B–C, F, and J). Inside the bubble, pores contain microcrystalline clusters of silica-rich carbonaceous matter with various amounts of manganese and iron (Fig. 12B–D, points 1–4 and 9; 12F, point 6; 12G, point 4; and 12K, point 3) or carbon and manganese (Fig. 12F, points 1–4 and 7–8; 12G, points 2, 3, and 5; and 12H, points 1–7). The mineral compositions in the microcrystalline clusters are compatible with bixbyite and hausmannite (Fig. 11D, points 10–11 and 13), rhodochrosite (Fig. 12J, points 5–8; and 12K, points 7–8 and 11–12), manganite (γ-MnOOH), and oxidized pyrochroite [$(Mn(OH)_2$].

4.4. Iron-rich rocks hosting massive manganese ore layers

Jaspilite and massive, iron-rich jasper are the most common rocks (Figs. 2 and 13A), and are the protores of the main iron ore type (Fig. 13B) mined in the Urucum region. The jaspilite are nodular, contain oval silica nodules and microlenses, and consist of 55–60 vol% hematite and 35–40 vol% chert (65–75 wt% Fe_2O_3, 25–30 wt% SiO_2). The peloidal stratified and the banded BIFs (Fig. 13C) with amygdalites are the main BIFs of the Urucum region. They are gray and brown-red in color, cryptocrystalline, locally sandy or arkosic (Fig. 8D–E, Table 1), and consist of 55–88 vol% hematite and 10–45 vol% iron-rich chert (10–45 wt% Fe_2O_3, 3–45 wt% SiO_2, and 0–3 wt% MnO). The jaspilite are composed of a mosaic of hematite and chert microclusters with very

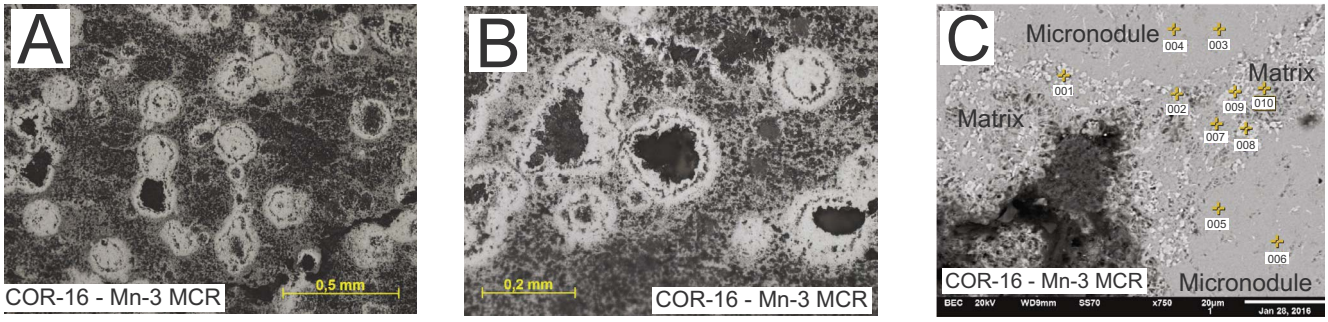

Figure	Point nº	Identification	Analyzed element (%)								
			Cryptomelane micronodules amid amorphous matrix with Fe + Mn oxides								
			C	Free C >	Si	Al	Na	K	Mn	Fe	Ba
9C	1	Fe+Mn amorphous matrix	7.3		<0.1	0.0	<0.1	1.8	23.4	46.2	0.7
	2	Fe+Mn amorphous matrix	5.3		<0.1	0.3	<0.1	2.2	31.8	37.8	1.7
	3	Fe-rich cryptomelane	5.3		<0.1	0.3	<0.1	4.2	63.1	4.9	1.2
	4	Fe-rich cryptomelane	6.7		<0.1	0.3	<0.1	4.2	61.9	4.5	1.7
	5	Fe-rich cryptomelane	4.9		<0.1	0.4	<0.1	4.7	63.4	3.4	2.2
	6	Fe-rich cryptomelane	6.2		<0.1	0.2	<0.1	4.8	61.9	4.7	1.7
	7	Fe-rich cryptomelane	6.5		<0.1	0.3	<0.1	5.1	63.1	3.0	1.2
	8	Fe+Mn amorphous matrix	8.4		<0.1	0.1	<0.1	1.0	12.7	56.9	0.6
	9	Fe+Mn amorphous matrix	7.1		<0.1	0.0	<0.1	0.9	11.1	60.3	0.1
	10	Fe-rich cryptomelane	9.1		<0.1	0.4	<0.1	5.1	60.7	3.0	1.7

Figure	Point nº	Identification	C	Free C>	Si	Al	Na	K	Mn	Fe	Ba
9D	1	Cryptomelane	6.7		<0.1	0.4	<0.1	4.1	58.1	<0.1	<0.1
	2	Cryptomelane	6.8		<0.1	0.8	<0.1	3.7	56.7	<0.1	<0.1
	3	Cryptomelane and carbonaceous matter	13.7		<0.1	<0.1	<0.1	4.3	63.2	<0.1	<0.1
	4	Rhodochrosite and carbonaceous matter	39.4	33.2	<0.1	0.8	<0.1	1.7	24.8	3.6	<0.1
	5	Rhodochrosite and carbonaceous matter	32.3	23.4	<0.1	0.7	<0.1	3.2	40.7	<0.1	<0.1
	6	Rhodochrosite and carbonaceous matter	25.6	15.5	<0.1	0.6	<0.1	3.2	46.0	<0.1	<0.1
	7	Hematite	6.0		<0.1	<0.1	<0.1	<0.1	2.4	64.7	<0.1
	8	Cryptomelane	6.0		<0.1	1.0	<0.1	4.1	60.2	<0.1	<0.1
	9	Mn+Fe amorphous matrix	5.0		<0.1	1.2	<0.1	2.9	45.1	13.4	<0.1
	10	Fe-rich cryptomelane	5.3		<0.1	0.7	<0.1	4.5	57.3	<0.1	<0.1

Fig. 9. Micronodular manganese ore from layer Mn-3. (A, B) Optical images of zoned micronodules (RL, //N). (C–E) SEM images and EDS compositions of micrometer-scale micronodules of massive cryptomelane (± hollandite) in a matrix of cryptomelane and hematite. Points 4–6 in Image D show that the matrix is carbonaceous. (F–I) Images showing that the millimeter-scale micronodules are composed of amalgamated micrometric micronodules of cryptomelane/hollandite. RL, xN; H and I are SEM images. In Figs. 9–12, the names of the Mn mine and Mn layer from which the sample was collected are shown within the image and in Fig. 7. The mine locations are shown in Figs. 1 and 3.

irregular shapes (Fig. 13E–F). Across the transition with layer Mn-2 or Mn-3, the jaspilite (Fig. 13D, part A) mix gradually with layers of manganese oxides (Fig. 13D, part B and other gray portions) to form a layer of massive manganese oxide. Massive and banded IFs containing lenses of massive, microgranular hematite with some quartz fragments (Fig. 13G–H) overlie the Santa Cruz Formation (Fig. 2).

5. Major, trace and rare earth elements geochemistry

5.1. Major and trace elements

Based on their Si, Fe, and Mn contents, the Urucum manganese ores can be classified into three groups, shown by plotting them on a SiO_2–Mn–$Fe_{(TOTAL)}$ ternary diagram (Fig. 14A). Group A consists of layer Mn-2 and Mn-3 manganese ores, characterized by low silica concentrations; Group B consists of layer Mn-1 ores, containing chert and detritic clay mineral and quartz; and Group C consists of massive IFs hosting manganese layers, characterized by variable silica concentrations, which are mined as iron ores.

In Mn ores from the Figueirinha, São Domingos, and Rabicho mines, which mine the Mn-1 ore layer, the Mn content decreases proportionally to K_2O (Fig. 14B), and K_2O concentrations are inversely proportional to Ba concentrations (Fig. 14C). Fig. 14D shows a lack of correlation between the Y/Ho ratio and Al_2O_3 concentration.

Fig. 15 shows several geochemical patterns. (a) In the layers where the manganese content is high, the silica content is low. The SiO_2 content is < 4% in layers Mn-2 and Mn-3, and < 30% in layer Mn-1. (b) The Co concentrations are high in all of the manganese-rich layers, i.e., always greater than in the adjacent iron-rich layers. The concentrations are > 1000 ppm in layer Mn-1 and decrease stratigraphically upward, ranging from 400 to 500 ppm in layer Mn-2 and from 150 to 300 ppm in layer Mn-3. (c) At the Urucum region, all the Mn-rich layer are enriched in Co, but their Co concentrations decrease upward from Mn-1 to Mn-3 (Fig. 15), in contrast to the hosting IFs, in which the Co concentrations are much lower. (d) The distribution and the Co, P and Ni contents chemically differentiate the Mn-1 unit layers of the Mn-2 and Mn-3. Mn-2 and Mn-3 concentrate simultaneously P, Co and Ni, and the IFs that host them are devoid of these elements (Fig. 15). In São Domingos and Figueirinha, the manganese-rich Mn-1 layers have very high Co (and Cu) and low P and Ni contents, and the IFs that host them have very high contents of P and Ni, contrasting with the IFs that host Mn-2 and Mn-3. (d) The phosphorous concentrations separate the manganese- and iron-rich layers into two distinct groups: (Group 1) Below layer Mn-2, P concentrations are low (< 1500 ppm) in the manganese layer and high (between 1400 and 3500 ppm) in the iron layer; (Group 2) Above layer Mn-1, this relation is reversed and the P concentrations are high (between 1100 and 3000 ppm) in manganese-rich layers and low (< 750 ppm) in iron-rich layers. (e) The nickel content of the manganese ores exceeds the background concentration (≈ 40 ppm) only in layer Mn-1 in the Figueirinha, Rabicho, and Jacadigo mines, and in the iron-rich rocks from the MMX and Figueirinha mines.

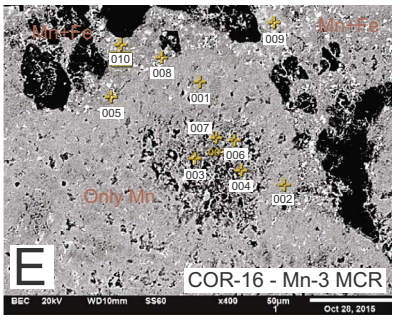

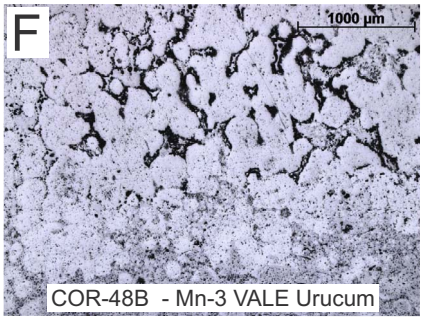

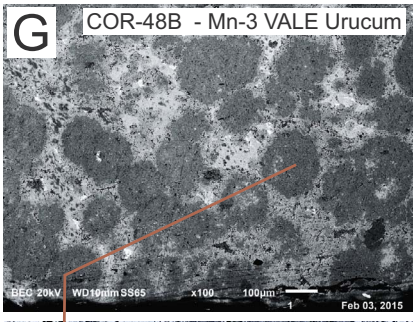

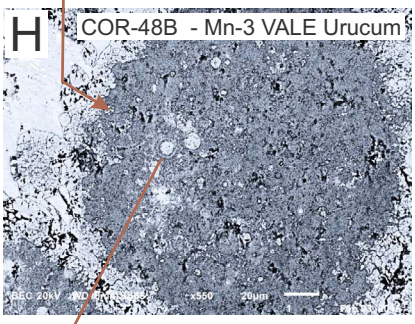

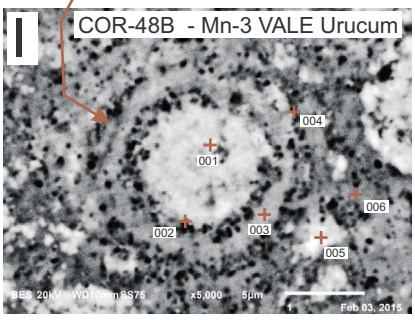

Figure	Point n°	Identification	Analyzed element (%)								
			Cryptomelane nicronodules amid amorphous matrix with Fe + Mn oxides								
			C	Free C >	Si	Al	Na	K	Mn	Fe	Ba
9E	1	Cryptomelane	5.5		<0.1	<0.1	<0.1	4.2	57.8	<0.1	1.6
	2	Cryptomelane	7.4		<0.1	<0.1	<0.1	3.8	56.1	<0.1	1.6
	3	Cryptomelane	7.3		<0.1	1.3	<0.1	3.8	53.0	<0.1	1.2
	4	Cryptomelane and carbonaceous matter	8.7		<0.1	0.9	<0.1	3.8	53.9	<0.1	<0.1
	5	Mn-rich hematite and carbonaceous matter	9.9		<0.1	<0.1	<0.1	0.5	7.7	61.6	<0.1
	6	Cryptomelane and carbonaceous matter	8.2		<0.1	<0.1	<0.1	4.0	56.4	<0.1	<0.1
	7	Cryptomelane and carbonaceous matter	10.1		<0.1	0.7	<0.1	3.9	54.1	<0.1	<0.1
	8	Cryptomelane and carbonaceous matter	9.4		<0.1	0.8	<0.1	4.2	54.5	<0.1	<0.1
	9	Cryptomelane and carbonaceous matter	9.1		<0.1	1.3	<0.1	3.1	52.8	<0.1	1.7
	10	Fe-rich cryptomelane and carbonaceous matter	8.3		<0.1	1.1	<0.1	3.0	46.7	6.6	1.7

Figure	Point n°	Identification	C	Free C >	Si	Al	Na	K	Mn	Fe	Ba
9 I	1	Fe-rich cryptomelane	4.27		<0.1	<0.1	0.1	1.64	64.58	4.51	1.67
	2	Cryptomelane/Hollandite	5.49		<0.1	<0.1	0.35	2.51	63.03	4.69	2.27
	3	Fe-rich cryptomelane	4.94		<0.1	<0.1	1.14	2.14	64.41	4.69	0.73
	4	Fe-rich cryptomelane	4.69		<0.1	<0.1	0.89	2.43	64.78	4.97	0.39
	5	Cryptomelane/Hollandite	4.77		<0.1	<0.1	0.65	2.34	63.5	5.03	2.46
	6	Fe-rich cryptomelane	4.47		<0.1	<0.1	0.99	2.21	64.65	5.64	0.35

Fig. 9. (*continued*)

5.2. REE chemistry

Regarding Ce anomalies ($=Ce_N/[(La_N + Nd_N)/2]$; Murray, 1994), the average Ce anomaly in the Urucum iron-rich rocks hosting the manganese ores is negative ($Ce_{Anomaly} < 1$), i.e., equal to 0.77 (s.d. = 0.13, n = 39). In the manganese ore, disregarding layer Mn-3 in the MMX Mine (Table 1, Fig. 15), the average Ce anomaly is 0.85 (s.d. = 0.32, n = 30).

The REE patterns for all of the Mn-1 ore layer samples, normalized to the NASC, are plotted in Fig. 16A together with the patterns for seawater and river water ($\times 10^{-7}$). The same was done in Fig. 16C for the ores from layers Mn-2 and Mn-3, in Fig. 16E for all the IFs, and in Fig. 16G for all the ferruginous arkosic rocks. Fig. 16B, D, F, and H show the contours of the REE profiles in Fig. 16A, C, E and G, respectively, which are referred to as the REE models.

The REE model for layer Mn-1 shows a small negative Ce anomaly and enrichment in REEs from Ce to Lu. The REE pattern for the Rabicho ore is the only one showing a positive Ce anomaly (=1.29) and heavy rare earth element (HREE) enrichment. Note that the Rabicho ore mineral is detrital pyrolusite; whereas, that of the São Domingo Mine consists of hollandite–cryptomelane. The Figueirinha Mine is the only location where braunite is an ore mineral, along with cryptomelane and hollandite (Table 1, Fig. 16A and B). Samples from a haulage tunnel, from "galleries 5A and 6A," and from Mn-1 of the "Urucum mines," whose sampling sites were not identified, were analyzed by Klein and Ladeira (2004), which revealed the presence of aegirine. As these samples contain braunite, they would supposedly have been taken from the Mn-1 layer in the Figueirinha Mine region (see column 4, Table 1). The average compositions of mud and hematite chert from the Rapitan Group (Halverson et al., 2011) and reworked hematite mud from the Santa Cruz iron deposit (Angerer et al., 2016), normalized to the NASC, are similar to the compositions of the iron-rich rocks hosting the massive manganese ore layers (Fig. 16F).

With the exception of layer Mn-3 from the MCR Mine (Figs. 15 and 16D), the REE models for layers Mn-2 and Mn-3 show an average Ce anomaly of 0.72 (s.d. = 0.22, n = 16), depletion in middle rare earth elements (MREEs), and enrichment in HREEs from Gd to Lu. The REE pattern for layer Mn-3 from the MCR Mine shows a positive average Ce anomaly of 1.85 (s.d. = 0.50, n = 4), and enrichment in MREEs as well as HREEs from Dy to Lu. The iron-rich rocks hosting the manganese ore layers are enriched in MREEs and HREEs from Dy to Lu (Fig. 16F). The REE model for the ferruginous and manganiferous arkosic rocks (Fig. 16H) shows an average Ce anomaly of 0.76 (s.d. = 0.07, n = 7), enrichment in MREEs, and depletion in HREEs from Tb to Lu. The average value of the Eu anomalies is 1.03 (s.d. = 0.07, n = 69), and there is no significant Eu anomalies in the manganese ores and the host iron-rich rocks (Table 1, Fig. 15).

Excluding layer Mn-2 ores from the VALE and MMX mines, the average La_N/Ce_N ratio (Table 1) of the Urucum iron and manganese ores is 1.12 (s.d. = 0.26, n = 68). The average La_N/Ce_N ratio of the Mn-2 manganese ores, with > 64% MnO, from the VALE-Urucum Mine is 1.80 (s.d. = 0.12, n = 5). In the MMX-Urucum Mine, the average ore composition is 65.7% MnO, and the average La_N/Ce_N ratio is 1.66 (s.d. = 0.11, n = 3). The La_N/Ce_N ratio of sample COR-48, taken from a zone in layer Mn-3 with numerous kremydilites, is 6.24. The manganese ores and the Fe-rich rocks hosting layers Mn-1, Mn-2, and Mn-3 do not show Eu anomalies. Only in ore from the Mn-3 layer in the MCR Mine (Fig. 15C and D) are the Eu_N and Sm_N values slightly larger than the

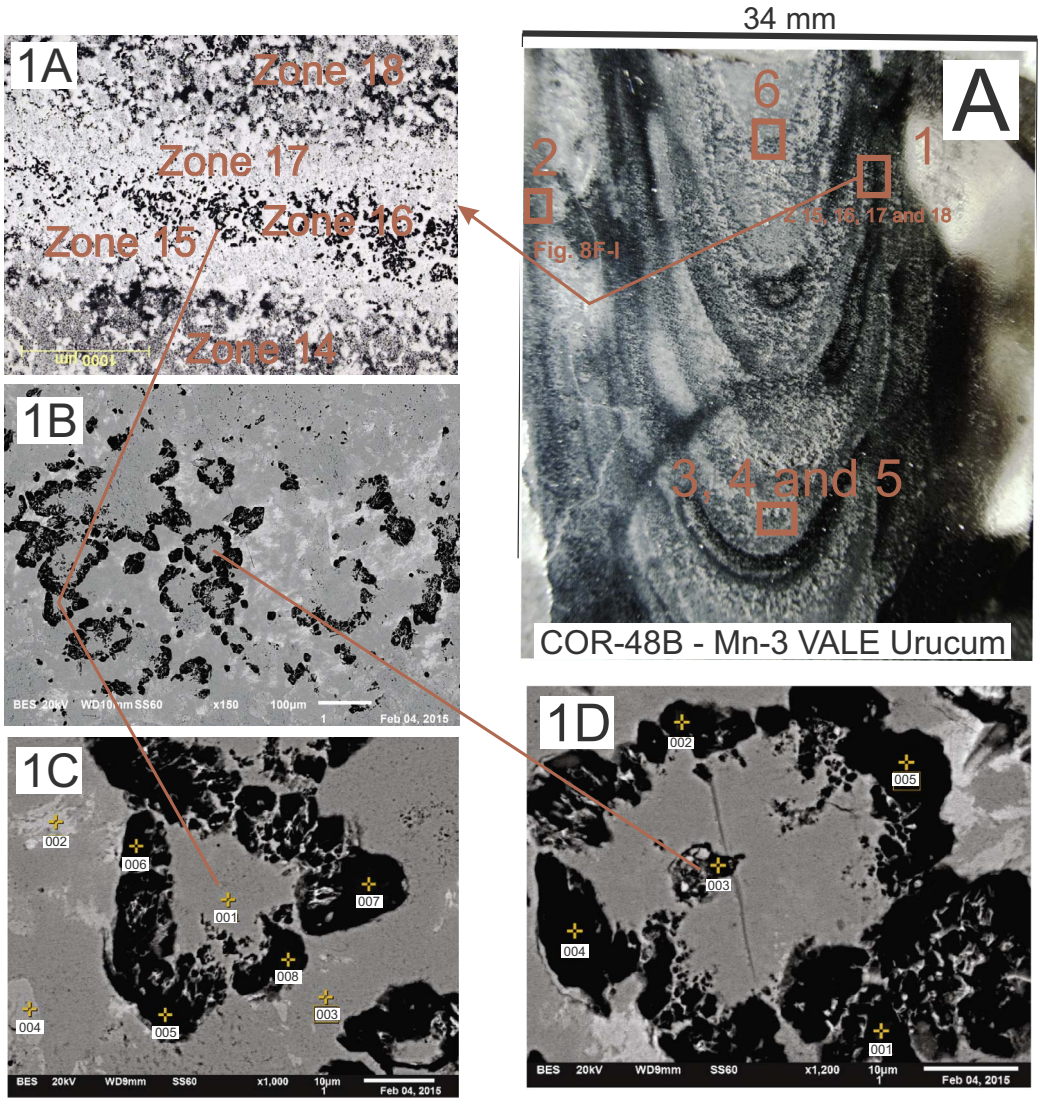

Fig. 10. Kremydilite from layer Mn-3 (sample COR-48B, from the VALE-Urucum Mine). (A) Concentric zonation in the central part of the kremydilite. In Fig. 10A, 11A and 12A, the numbered boxes denote the positions where SEM – EDS analyses were performed. (1A–D) Kremydilite zones showing the distribution of anhedral rhodochrosite crystals in roughly spherical arrangements together with carbonaceous matter, and manganese nodules (Image D, points 2 and 3). (3A–D) SEM – EDS Analyzes showing roughly cylindrical holes near clusters of rhodochrosite needles. (4A–C) Groups of wormlike objects composed of almost pure carbonaceous matter (Image 4C, points 1–6) amid micronodules whose compositions are consistent with those of hausmannite, Ba-rich hollandite (Image 4A, points 1–8), and Si + Mn-rich carbonaceous matter. (5A–E) Micrometer-scale wormlike objects (Images 5B–D) composed of Mn-rich carbonaceous matter (Images 5B–D) and surrounded by prismatic rhodochrosite microbialites amid a matrix of Mn-rich carbonaceous matter (Images 5C–E). (6A) Micronodular micrometric C-rich cryptomelane microbialites adjacent to rhodochrosite microprisms and wormlike objects.

Figure	Point nº	Identification	Analyzed element (%)								
			Carbonate crystals in roughly circular arrangements amid cryptomelane matrix								
			C	Free C >	Si	K	Mn	Mg	Ca	Ba	Sr
10.1C	1	Cryptomelane and carbonaceous mater	8.8		0.3	2.2	68.1	<0.1	<0.1	<0.1	0
	2	Sr-rich hollandite	8.4		0.2	1.3	61.0	<0.1	0.4	5.9	3.1
	3	Carbonaceous cryptomelane	8.3		<0.1	1.0	69.1	<0.1	0.2	0.7	0.2
	4	Manganite?	7.4		1.6	<0.1	67.8	<0.1	1.1	<0.1	<0.1
	5	Rhodochrosite and carbonaceous mater	**25.1**	**12,5**	0.1	0.3	56.8	<0.1	0.3	0.5	<0.1
	6	Sr-rich rhodochrosite and carbonaceous mater	**24.0**	**12,5**	2.3	0.8	51.5	<0.1	0.2	1.6	1.2
	7	Dolomite	**26.6**		<0.1	<0.1	2.1	18.5	28.7	<0.1	<0.1
	8	Dolomite	**22.0**		<0.1	<0.1	1.9	17.5	33.3	<0.1	<0.1

Figure	Point nº	Identification	C	Free C >	Si	K	Mn	Mg	Ca	Ba	Sr
10.1D	1	Mn-rich dolomite	**20.6**		<0.1	<0.1	11.1	10.3	34.0	<0.1	<0.1
	2	Si-rich carbonaceous matter	**53.4**	**52,4**	19.1	<0.1	4.4	<0.1	<0.1	<0.1	<0.1
	3	Rhodochrosite and Si-rich carbonaceous mater	**44.1**	**40,4**	15.8	<0.1	17.1	<0.1	<0.1	<0.1	<0.1
	4	Manganite and carbonaceous mater	9.2		<0.1	0.9	69.2	<0.1	<0.1	<0.1	<0.1
	5	Rhodochrosite and carbonaceous mater	**64.8**	**58,9**	<0.1	<0.1	27.1	<0.1	<0.1	<0.1	<0.1

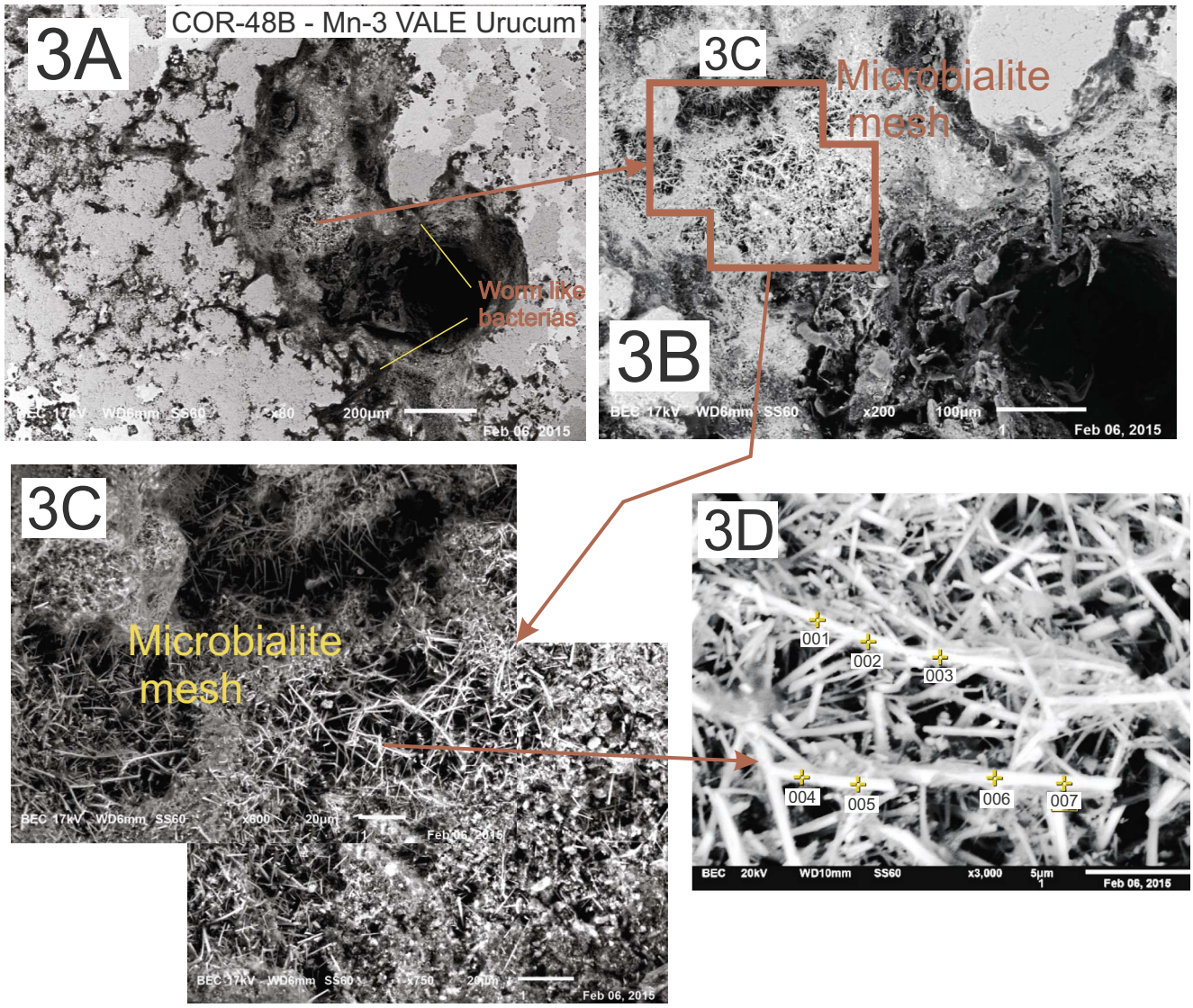

Figure	Point nº	Identification	Analyzed element (%)											
			Microbialite mesh											
			C	Free C >	Si	K	Mn	Fe	Mg	Ca	Ba	Sr	P	S
10.3 D	1	Rhodochrosite and carbonaceous matter	**16.7**	**3.4**	0.6	2.8	60.9	<0.1	<0.1	<0.1	<0.1	<0.1	<0.1	<0.1
	2	Cryptomelane and carbonaceous matter	11.4		0.9	3.0	64.4	<0.1	<0.1	<0.1	<0.1	<0.1	<0.1	<0.1
	3	Rhodochrosite and carbonaceous matter	**14.1**	**0.5**	0.8	3.1	62.2	<0.1	<0.1	<0.1	<0.1	<0.1	<0.1	<0.1
	4	Rhodochrosite and carbonaceous matter	**17.5**	**4.5**	0.8	3.2	59.5	<0.1	<0.1	<0.1	<0.1	<0.1	<0.1	<0.1
	5	Rhodochrosite and carbonaceous matter	**18.1**	**5.1**	0.8	2.8	59.5	<0.1	<0.1	<0.1	<0.1	<0.1	<0.1	<0.1
	6	Cryptomelane and carbonaceous matter	13.0		0.5	3.0	63.7	<0.1	<0.1	<0.1	<0.1	<0.1	<0.1	<0.1
	7	Cryptomelane and carbonaceous matter	11.6		0.9	2.8	64.4	<0.1	<0.1	<0.1	<0.1	<0.1	<0.1	<0.1

Fig. 10. (*continued*)

Nd_N and Gd_N values, indicating a very discrete Eu enrichment.

Negative Ce anomaly values in rocks from the Santa Cruz deposit (Angerer et al., 2016) are slightly more pronounced (average Ce anomaly = 0.61; s.d. = 0.22, n = 11). These rocks are also more depleted in light rare earth elements (LREEs) than the manganese- and iron-rich rocks from the Urucum region (Figs. 16 and 17A). REE enrichment in the podded chert–hematite BIF, podded dolomite–chert–hematite BIF, and banded dolomite–chert–hematite BIF analyzed by Angerer et al. (2016) occurs from Ce to Lu (Fig. 17A), similar to the chert hematite with ferroan carbonate (Fig. 17B) analyzed by Klein and Ladeira (2004). Negative Ce anomalies in the banded chert–hematite BIF and chemical hematite mud from the Santa Cruz deposit (Fig. 16A) are discrete (Ce anomaly = 0.82–0.90); these samples show strong enrichment in REEs from Ce to Lu.

The REE patterns for most of the ferroan carbonate and hematite chert samples from the northern Urucum region, analyzed by Klein and Ladeira (2004), are also more depleted in LREEs than for the iron-rich rocks hosting the Mn ore layers. Although the negative Ce anomalies

Figure	Point nº	Identification	C	Free C >	Si	K	Mn	Fe	Mg	Ca	Ba	Sr	P	S
10.4 A	1	Rhodochrosite and Si-rich carbonaceous matter	25.9	20.0	17.8	1.5	24.5	<0.1	<0.1	1.9	<0.1	<0.1	<0.1	<0.1
	2	Rhodochrosite and Si-rich carbonaceous matter	34.6	27.5	10.4	1.4	29.8	<0.1	<0.1	2.0	<0.1	<0.1	<0.1	<0.1
	3	Ba-rich hollandite	<0.1		<0.1	1.1	65.1	<0.1	<0.1	<0.1	13.1	<0.1	<0.1	<0.1
	4	Ba-rich hollandite	<0.1		<0.1	0.9	64.2	<0.1	<0.1	<0.1	14.3	<0.1	<0.1	<0.1
	5	Hausmannite?	7.1		<0.1	1.9	42.6	27.1	<0.1	<0.1	<0.1	<0.1	0.3	<0.1
	6	Hausmannite?	4.7		<0.1	1.8	44.0	27.6	<0.1	<0.1	<0.1	<0.1	0.2	<0.1
	7	Hausmannite?	9.3		<0.1	1.8	53.5	14.2	<0.1	0.5	<0.1	<0.1	0.2	<0.1
	8	Hausmannite?	6.3		<0.1	1.8	39.6	30.9	<0.1	<0.1	<0.1	<0.1	0.3	<0.1

Figure	Point nº	Identification	C	Free C >	Si	K	Mn	Fe	Mg	Ca	Ba	Sr	P	S
10.4C	1	Carbonaceous matter and rhodochrosite	71,9	67.6	1,2	<0.1	14,9	4,9	<0.1	<0.1	<0.1	<0.1	<0.1	<0.1
	2	Carbonaceous matter	80,5	79.8	3,9	<0.1	3,1	<0.1	<0.1	<0.1	5,0	<0.1	<0.1	0,7
	3	Carbonaceous matter and rhodochrosite	72,1	69.2	4,1	<0.1	13,2	<0.1	<0.1	<0.1	<0.1	<0.1	<0.1	0,3
	4	Carbonaceous matter and rhodochrosite	87,7	86.0	1,0	<0.1	7,9	<0.1	<0.1	<0.1	<0.1	<0.1	<0.1	<0.1
	5	Ca-rich carbonaceous matter	90,1	88.0	<0.1	<0.1	0,0	<0.1	<0.1	7,1	<0.1	<0.1	<0.1	<0.1
	6	Carbonaceous matter	91,6	90.5	0,9	<0.1	2,8	2,2	<0.1	<0.1	<0.1	<0.1	<0.1	<0.1
	7	Cryptomelane	8,8		<0.1	4,5	66,4	<0.1	<0.1	<0.1	<0.1	<0.1	<0.1	<0.1
	8	Hematite and carbonaceous matter	12,6	1.3	<0.1	<0.1	3,2	49,1	<0.1	<0.1	<0.1	<0.1	<0.1	<0.1

Fig. 10. (*continued*)

have the same order of magnitude (Ce anomaly = 0.76), the iron-rich ores with ferroan carbonate are frequently enriched in REEs from Ce to Lu (Fig. 17B). The negative Ce anomalies in the iron-rich rocks with manganoan carbonate are also in the region of 0.76, but the LREE concentrations in these rocks are lower, and the enrichments from MREEs to HREEs are less pronounced.

The REE pattern for the braunite-rich Mn-1 layer in the Figueirinha Mine (Fig. 16A) is similar to the REE pattern for the manganese Mn-1 ore containing braunite–cryptomelane–aegirine–dolomite (Fig. 16B) analyzed by Klein and Ladeira (2004), which suggests that these samples are from the same location.

6. Discussion

6.1. Geological environment and age constraints

The average La_N/Ce_N ratio of the analyzed rocks from the Urucum region is less than 1.5 (Table 1). According to Murray et al. (1990), Murray (1994), and Chen et al. (2006), ratios of less than 1.5 are typical of sediments deposited in basins located on continental margins. Two conclusions can be drawn as follows: (1) The Urucum Basin was a marginal basin; and (2) The La_N/Ce_N ratios greater than 1.5 (Murray, 1994; Chen et al., 2006) in layers Mn-2 and Mn-3 (sample COR-48, with kremydilites), and in two samples from the Upper Mn-1 layer in the Figueirinha Mine, indicate that the basin was deeper during the deposition of these units. The La_N/Ce_N ratios exceeding 1.5 in some of the Figueirinha and São Domingos ores suggest that at the beginning of basin flooding, when the Upper Mn-1 layer was deposited, the seawater was similar in composition to that when layers Mn-2 and Mn-3 were deposited. The newly flooded basin depocenter received a great quantity of clastic material. In these areas, the Upper Mn-1 layer consists of clay and carbonate (Figueirinha region; COR-07) and clastic–chemical ferruginous rocks (São Domingos region; COR-31 and 35).

Urban et al. (1992) used the stratigraphic position of the Mn-1 layer to level the stratigraphic columns constructed for the Urucum, Jacadigo, Figueirinha, São Domingos, Morro Grande, and Rabicho plateaus. On the Rabicho and Jacadigo plateaus, and in the Morro Grande, Laginha, and Tromba dos Macacos deposits (Fig. 1), located on the margins of the Urucum Basin, Mn-1 contains predominantly sandy, ferruginous clastic rocks, and the manganese layers are detrital and/or concretionary (Fig. 5); whereas, in the Figueirinha and São Domingos areas, Mn-1 is massive and clastic–chemical diagenetic or sedimentary. This variation in Mn-1 composition relative to its location within the basin suggests that Mn-1 was deposited on the basin floor, as will be discussed below. In contrast, the Mn-2 and Mn-3 layers show little lateral variation in characteristics, and they do not contain detritic ores (Fig. 7). As indicated by the similarities between layers Mn-2 and Mn-3 throughout the Urucum region, and by the constant vertical thicknesses between these layers (Fig. 5), the basin floor was already horizontal when the Mn-2 layer was deposited. Fig. 5 contains the same elements as Fig. 9 of Urban et al. (1992); however, it was prepared by leveling all the stratigraphic columns at the base of layer Mn-2. This figure roughly shows the basin morphology and the original stratigraphy of the Jacadigo Group within the Urucum Basin.

Carbonate rocks of the Corumbá Group bound the sedimentary rocks of the Jacadigo Group to the south, east, and north, which also suggests the presence of an ancient sedimentary basin in which the Jacadigo Group was deposited at great depths (Figs. 1 and 2), within the basin depocenter, and the Corumbá Group was deposited at the basin margins (Fig. 1, dashed lines). It is likely that the basin initially

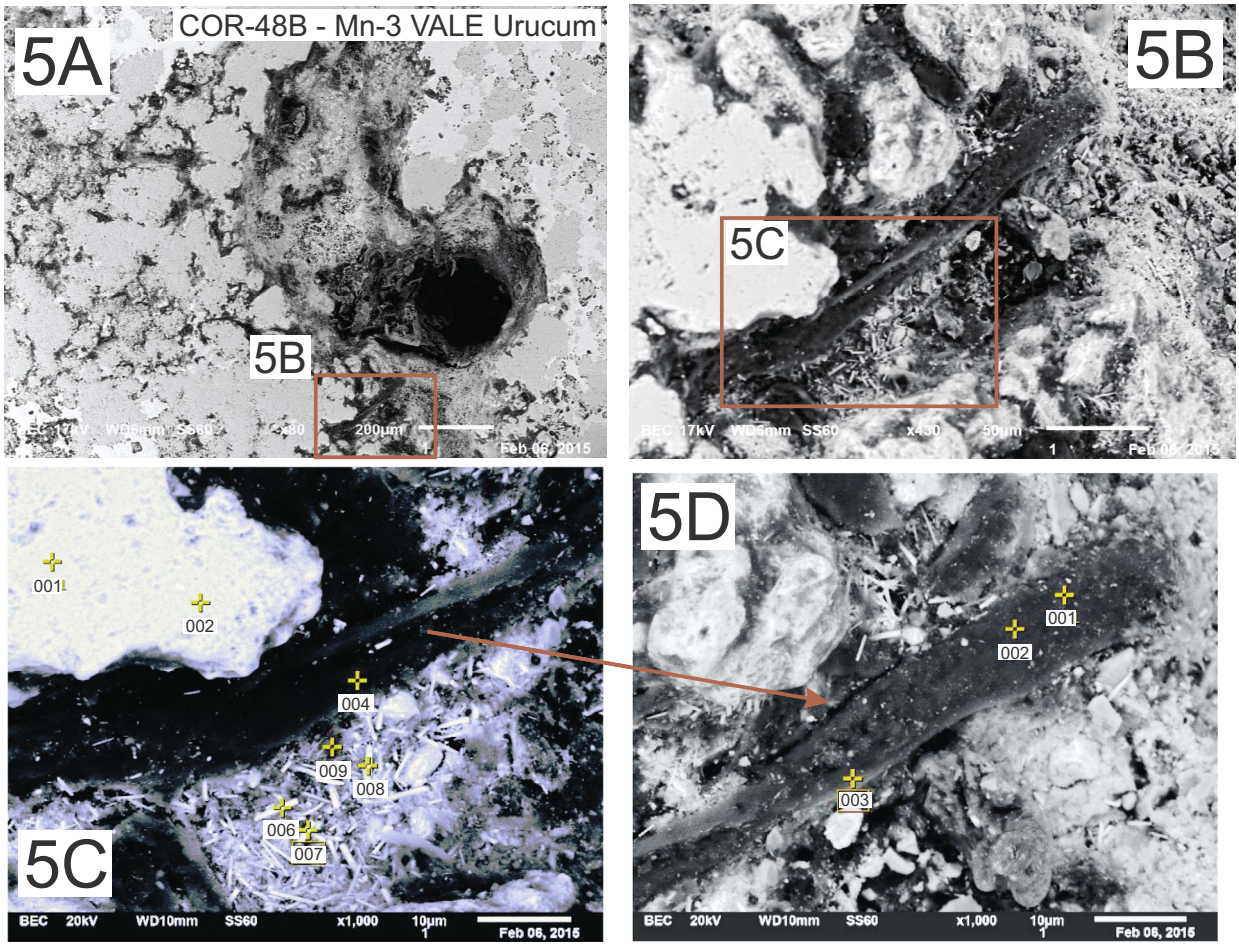

Figure	Point nº	Identification	Analyzed element (%) Prismatic microbialites								
			C	Free C >	Si	K	Mn	Fe	Mg	Ca	Ba
10.5C	1	Cryptomelane	5.4		<0.1	2.7	70.7	<0.1	<0.1	<0.1	<0.1
	2	Cryptomelane	<0.1		<0.1	3.7	74.0	<0.1	<0.1	<0.1	<0.1
	4	Carbonaceous matter and rhodochrosite	**66.5**	**61.3**	0.7	1.2	23.7	<0.1	<0.1	<0.1	<0.1
	6	Cryptomelane and carbonaceous matter	8.9		<0.1	1.0	69.6	<0.1	<0.1	<0.1	<0.1
	7	Rhodochrosite	**14.3**	**0.4**	0.4	1.4	63.5	<0.1	<0.1	<0.1	<0.1
	8	Rhodochrosite and carbonaceous matter	**21.6**	**9.2**	<0.1	2.6	56.8	<0.1	<0.1	<0.1	<0.1
	9	Rhodochrosite and carbonaceous matter	**32.8**	**22.3**	<0.1	2.3	47.9	<0.1	<0.1	<0.1	<0.1
Figure	Point nº	Identification	C	Free C >	Si	K	Mn	Fe	Mg	Ca	Ba
10.5D	1	Si-rich carbonaceous matter	**81.8**	**81.3**	7.0	<0.1	2.4	<0.1	<0.1	<0.1	<0.1
	2	Carbonaceous matter and rhodochrosite	**61.4**	**55.1**	<0.1	1.3	28.7	<0.1	<0.1	<0.1	<0.1
	3	Carbonaceous matter and rhodochrosite	**65.4**	**60.2**	1.7	<0.1	24.0	<0.1	<0.1	<0.1	<0.1

Fig. 10. (*continued*)

developed as a graben, which formed a valley where fluvial, lacustrine, and deltaic fan (fan delta) clastic sediments (Fig. 18A; modified after Freitas et al., 2011; and this work) were deposited in an arid climate, as indicated by the unweathered feldspar fragments. These sequences constitute the Urucum Formation (Fig. 2B–C, lower part). The presence of hematite fragments in the clastic–chemical rocks overlying this

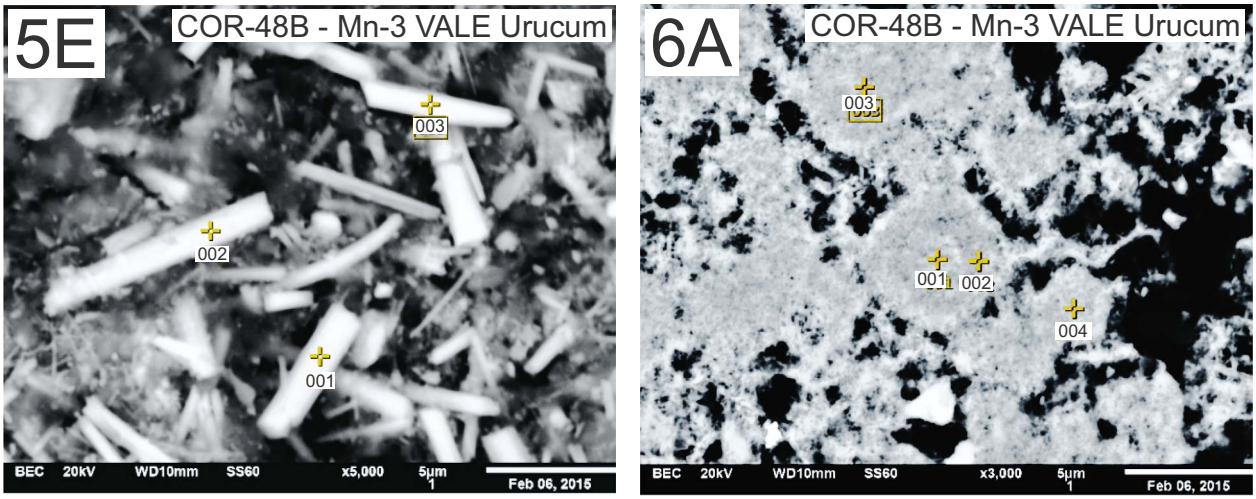

Figure	Point nº	Identification	C	Free C >	Si	K	Mn	Fe	Mg	Ca	Ba
10.5E	1	Cryptomelane and carbonaceous matter	12.9		<0.1	1.3	66.3	<0.1	<0.1	<0.1	<0.1
	2	Cryptomelane and carbonaceous matter	8.6		<0.1	0.8	70.0	<0.1	<0.1	<0.1	<0.1
	3	Rhodochrosite and carbonaceous matter	**32.1**	**21.1**	<0.1	2.3	50.4	<0.1	<0.1	<0.1	<0.1
Figure	Point nº	Identification	C	Free C >	Si	K	Mn	Fe	Mg	Ca	Ba
10.6A	1	Cryptomelane	5.0		<0.1	2.9	67.8	<0.1	<0.1	<0.1	3.1
	2	Cryptomelane and carbonaceous matter	11.5		<0.1	2.3	65.6	<0.1	<0.1	<0.1	<0.1
	3	Cryptomelane and carbonaceous matter	10.3		<0.1	2.6	66.9	<0.1	<0.1	<0.1	<0.1
	4	Rhodochrosite	**14.4**	**0.6**	<0.1	2.9	62.9	<0.1	<0.1	<0.1	<0.1

Fig. 10. (*continued*)

formation suggests erosion of a unit containing massive hematite located outside the Urucum Basin, and deposition of the resulting fragments prior to layer Mn-1.

The presence of a dolomite block containing stromatolites, below Mn-1 (Figs. 3B and 4A), and occurrences of the fossil *Corumbella werneri* in ironstones of the Santa Cruz Formation (Fig. 4B–D), located between Mn-2 and Mn-3, indicate that these units were deposited at the same time as the carbonate rocks of the Bocaina and Tamengo Formations, respectively. *Corumbella* lived during the Ediacaran and have estimated ages of cca. 550 Ma, consistent with an age of 543 Ma determined in the Tamengo Formation (Babinski et al., 2008) by dating of zircons collected from a volcanic ash layer. These data conflict with the ages of the manganese layers determined by Piacentini et al. (2013), who obtained $^{39}Ar/^{40}Ar$ ages of 587 ± 7 Ma, from cryptomelane in layers Mn-1, Mn-2, and Mn-3, and 513 ± 4 Ma, from muscovite in arkoses interlayered with the BIFs. These authors interpreted the age data as minimum ages, arguing that the argon thermo-chronological system was rejuvenated by tectonic warming and disruption between the Amazon Craton and the Rio Apa cratonic fragment. They concluded that these ages do not reflect the timing of Jacadigo Group deposition, which would be older than 590 Ma. Although the geochronological and paleontological ages appear to be inconsistent, common fossiliferous occurrences in rocks of the Santa Cruz, Bocaina, and Tamengo formations indicate that these units were coeval and were probably deposited during the latest Ediacaran and early Cambrian, more than 80 Ma and 30 Ma after the Marinoan (650–635 Ma) and Gaskiers (≈580 Ma) glaciations, respectively.

The existence of carbonate BIFs in the Santa Cruz Formation (Fig. 2; and Klein and Ladeira, 2004; Angerer et al., 2016) also suggests that these rocks and the carbonate rocks of the Corumbá Group are distinct lateral facies of coeval units. Their compositional differences may be a consequence of the sedimentary basin depth at the sites of deposition, and the stability of the solutes dissolved in the seawater in different environments.

Carbonate rocks are usually deposited in shallow and warm water, which conflicts with the interpretation of most authors that the rocks of the Santa Cruz Formation were deposited in a glacial environment. This interpretation is typically based on the presence of granite boulders that occur in the conglomeratic arkosic sandstones amid the BIFs, which are interpreted as dropstones (Urban et al., 1992; Hoffman and Schrag, 2002; Klein and Ladeira, 2004; Angerer et al., 2016). These boulders do not appear to be ice-rafted elements because they are not striated or faceted, and they do not cross-cut the underlying beds. The most likely interpretation is that they were transported into the basin by avalanches (Fig. 18E) generated during successive episodes of instability caused by the graben opening. Klein and Ladeira (2004) and Angerer et al. (2016) published $\delta^{13}C$ values ranging from −3.4 to −7.0‰ for carbonates associated with the BIFs from the Urucum and Santa Cruz deposits. Angerer et al. (2016), citing the interpretation of Kaufman and Knoll (1995), consider these $\delta^{13}C$ values to be consistent with signatures from *syn*-glacial deposits. In carbonates, negative $\delta^{13}C$ values of the same order of magnitude are also indicators of submarine hydrothermal environments (e.g., Large and Both, 1980; Kowalick et al., 1981; Okita et al., 1988; Eastoe and Nelson, 1988; Zaw and Large, 1992; MacLean and Hoy, 1991; Biondi et al., 2011); they are associated with carbonaceous matter (e.g., Hoefs and Frey, 1976; Hedges and Mann, 1979; Dean et al., 1986; Konhauser et al., 2005; Kump et al.,

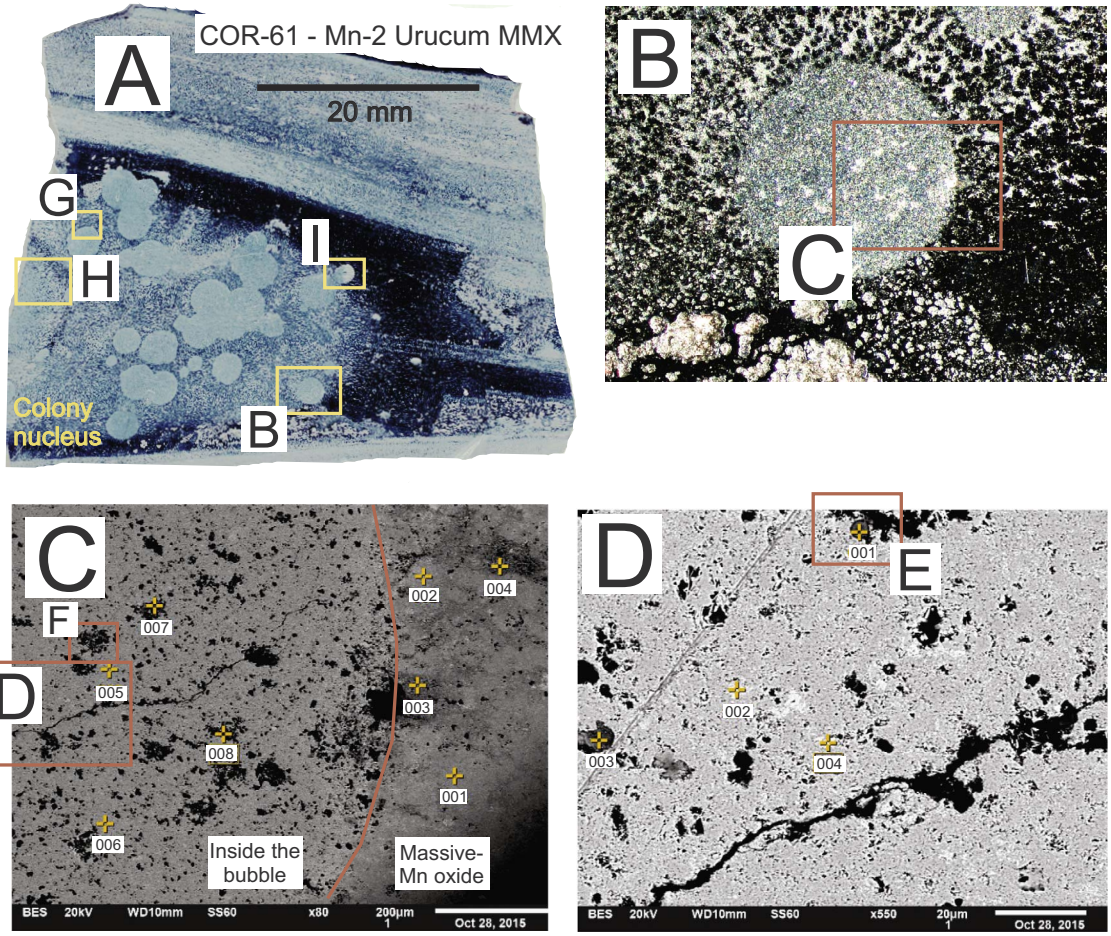

Figure	Point n°	Identification	Analyzed element (%) Inside one bubble									
			C	Free C >	Si	Al	K	Mn	Fe	Ca	Ba	P
11C	1	Cryptomelane	3.0		<0.1	<0.1	1.7	61.6	<0.1	<0.1	<0.1	<0.1
	2	Hollandite	4.0		<0.1	<0.1	3.1	54.0	<0.1	<0.1	5.9	<0.1
	3	Cryptomelane and carbonaceous matter	**13.8**	**3.9**	<0.1	0.9	1.5	45.3	<0.1	<0.1	<0.1	<0.1
	4	Cryptomelane and carbonaceous matter	9.6		<0.1	0.7	1.6	39.4	10.4	<0.1	<0.1	<0.1
	5	Hollandite	4.4		<0.1	<0.1	3.7	47.5	8.9	<0.1	3.3	<0.1
	6	Hollandite	5.4		<0.1	<0.1	3.7	48.1	7.6	<0.1	3.8	<0.1
	7	Ba-rich hollandite and carbonaceous matter	**32.8**	**23.3**	1.8	1.4	1.4	43.4	<0.1	<0.1	11.1	<0.1
	8	Bixbyite and carbonaceous matter	**36.3**	**28.4**	1.3	0.8	<0.1	12.0	24.6	<0.1	1.5	<0.1

Figure	Point n°	Identification	C	Free C >	Si	Al	K	Mn	Fe	Ca	Ba	P
11D	1	P-rich carbonaceous eosphorite and/or Mn- rich phosphatic clay?	**21.4**		<0.1	7.4	1.1	16.7	<0.1	2.4	<0.1	**6.1**
	2	Hematite and carbonaceous matter?	**12.6**		<0.1	<0.1	<0.1	6.1	50.3	<0.1	<0.1	<0.1
	3	P-rich carbonaceous eosphorite and/or Mn- rich phosphatic clay?	**14.3**		<0.1	7.3	1.4	21.9	<0.1	2.9	<0.1	**6.9**
	4	Hematite and carbonaceous matter?	**12.7**		<0.1	<0.1	<0.1	4.7	50.8	<0.1	<0.1	<0.1

Fig. 11. (A) Kremydilite core with spherical structures similar to intergranular and/or internodular gas bubbles. (B–E) SEM images and EDS analysis sequence showing the compositions of substances inside and outside the bubbles. Note that in 11C, the bubble is porous and surrounded by massive cryptomelane (± hollandite). (D, E) Pore inside the bubble infilled with substances whose compositions are consistent with those of P-rich eosphorite and/or Mn-rich phosphatic clay (?), hematite (?) and carbonaceous matter. (F) Prismatic microbialites in the matrix whose compositions are consistent with those of P-rich crandallite (?),rhodochrosite (?), Ba-rich rhodochrosite (?), and carbonaceous clay (?) (compare to Fig. 10.5C–E). (G–H) Bubble I from Fig. 11A, with massive wrap and porous micronodular core, which consists of cryptomelane ± hollandite. (I–J) The dark, right-hand part of bubble I (Image 11J) contains microcrystals with compositions compatible with rhodochrosite, which are mixed with carbonaceous matter. In the metallic, left-hand part (Image 11I), rhodochrosite was replaced by massive cryptomelane ± hollandite during diagenesis.

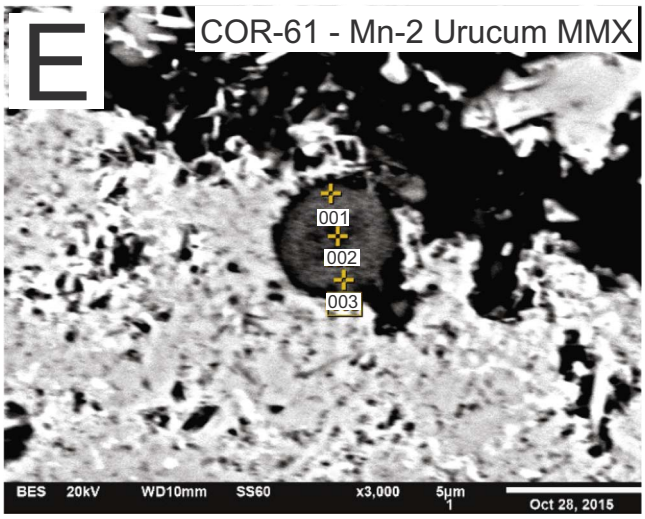

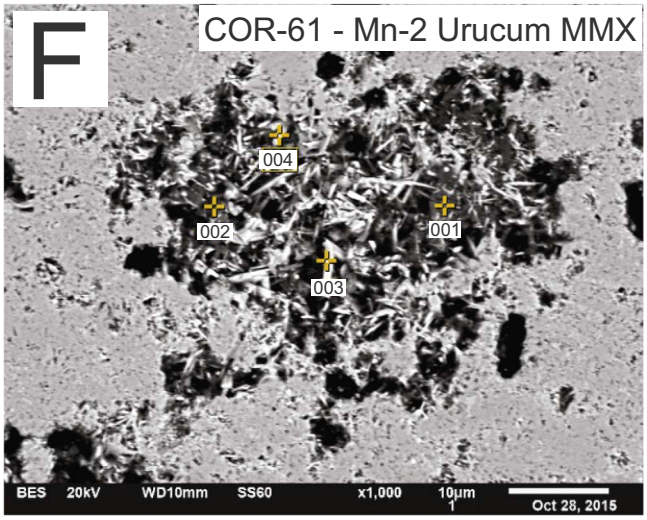

Figure	Point n°	Identification	C	Free C >	Si	Al	K	Mn	Fe	Ca	Ba	P
11E	1	P-rich eosphorite and/or Mn- rich phosphatic clay and carbonaceous matter?	**12.1**	**7.4**	<0.1	8.6	1.5	17.9	<0.1	2.6	<0.1	**7.1**
	2	P-rich eosphorite and/or Mn- rich phosphatic clay and carbonaceous matter?	**15.6**	**10.3**	<0.1	7.0	1.6	21.0	<0.1	2.4	<0.1	**6.0**

Figure	Point n°	Identification	C	Free C >	Si	Al	K	Mn	Fe	Ca	Ba	P
11F	1	P-rich, crandalite and carbonaceous matter?	**16.7**	**15.2**	<0.1	13.1	<0.1	<0.1	<0.1	5.1	1.3	**12.0**
	2	Carbonaceous clay?	**18.8**	**18.2**	14.0	13.4	<0.1	1.5	1.3	<0.1		<0.1
	3	Rhodochrosite and carbonaceous matter	**40.7**	**34.3**	1.1	0.5	0.7	22.5	7.1	<0.1	5.9	<0.1
	4	Ba-rich rhodochrosite and carbonaceous matter	**28.9**	**21.1**	0.4	<0.1	0.3	35.6	<0.1	<0.1	13.1	<0.1

Fig. 11. (*continued*)

2011; Polgári et al., 2012a,b), or they are considered as indicators of environments with organic carbon sources (e.g., Large et al., 2011; Boggs Jr., 2012). These other two interpretations of the $\delta^{13}C$ values were not considered by Angerer et al. (op. cit.), although they are equally applicable to the Urucum region. $\delta^{57}Fe$ values determined by Angerer et al. (2016) also indicate the absence of a glacial environment during deposition of the Santa Cruz Formation rocks. Based on five samples with $\delta^{57}Fe$ values between −2.62 and −0.04‰, Angerer et al. (2016) concluded that primary carbonate and associated hematite in the BIFs was mainly the product of "marine biomineralization by aerobic respiration of microbial colonies in a *warm* interglacial, shallow, saline water environment"; whereas, in the "*colder* and anoxic chert–BIF facies, biomineralization of Fe-hydroxides was also active but reduced." This indicates that the sedimentary environment was characterized by *warm*… and *colder*… *waters*; therefore, without the need for a glacial environment. In this work, and in accordance with the observations of Trompette et al. (1998) and Freitas et al. (2011), no diagnostic field evidence for the presence of glaciers during deposition of the Jacadigo Group was observed.

6.2. Chemistry of manganese ore layers and their iron-rich rocks

6.2.1. Microbially mediated vs. chemical sedimentation of major and trace chemical rock components

Fig. 14A shows several geochemical patterns. (a) Layer Mn-1 (Group B) differs from layers Mn-2 and Mn-3 (Group A) because of its higher concentrations of silica and iron. (b) The silica concentrations in layers Mn-2 and Mn-3 are very low, whereas the manganese concentrations are high. (c) The IFs above layer Mn-1 (Group C) are devoid of manganese. These three groups of rocks are geochemically distinct, which suggests that they were formed from by different genetic processes. The Mn concentration varies proportionally to K_2O (Fig. 14B) and Ba (Fig. 14C). This variation was observed for all the ores in layers Mn-1, Mn-2, and Mn-3, and is interpreted to be the result of cryptomelane transformation to hollandite, which began during diagenesis, and continued during the post-diagenetic periods, and probably occurs in at the present-day in ores that encountering meteoric water.

As shown in Fig. 15, Mn-2 and Mn-3 only consist of Mn, while their hosts contain Fe + SiO_2 and are devoid of Mn, which indicates distinct settling conditions. The presence of kremydilites (stromatolite-like

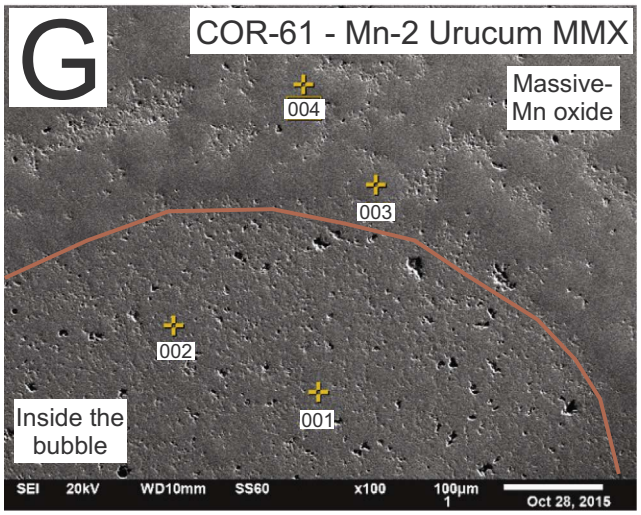

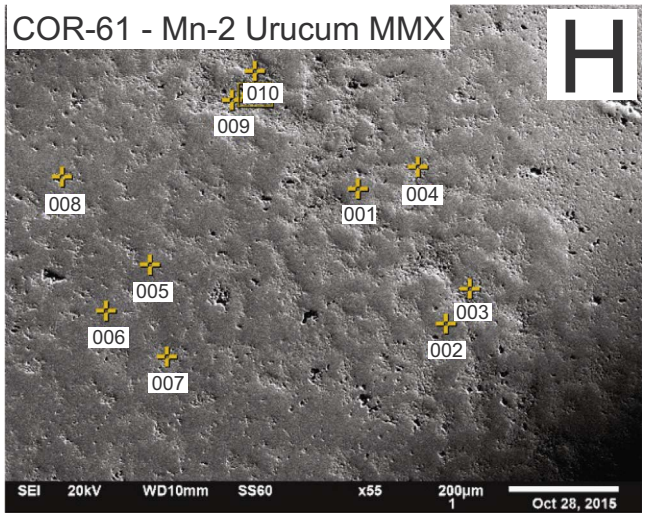

			Massive manganese oxide hosting the bubble										
			C	Free C >	Si	Al	K	Na	Mn	Fe	Ca	Ba	P
11G	1	Cryptomelane/ Hollandite	7.9		0.0	<0.1	5.2	<0.1	63.9	<0.1	<0.1	3.1	<0.1
	2	Cryptomelane/ Hollandite	5.5		0.0	<0.1	5.3	<0.1	65.3	<0.1	<0.1	3.5	<0.1
	3	Cryptomelane	5.8		1.5	<0.1	3.0	<0.1	67.6	<0.1	<0.1	0.0	<0.1
	4	Cryptomelane/ Hollandite	5.0		0.0	<0.1	3.6	<0.1	66.0	<0.1	<0.1	4.9	<0.1
Figure	Point nº	Identification	C	Free C >	Si	Al	K	Na	Mn	Fe	Ca	Ba	P
11H	1	Cryptomelane	6.4		<0.1	<0.1	3.9	<0.1	52.4	<0.1	<0.1	2.5	1.0
	2	Cryptomelane	5.8		<0.1	<0.1	1.2	<0.1	57.7	<0.1	<0.1	<0.1	<0.1
	3	Carbonaceous matter and rhodochrosite	**60.1**	**54.2**	<0.1	<0.1	0.8	<0.1	25.4	<0.1	1.0	2.1	<0.1
	4	Carbonaceous matter and hollandite	**22.0**	**14.8**	0.5	<0.1	0.8	<0.1	33.0	<0.1	<0.1	8.2	<0.1
	5	Cryptomelane	<0.1		<0.1	<0.1	1.0	<0.1	61.9	<0.1	<0.1	<0.1	<0.1
	6	Cryptomelane	<0.1		<0.1	<0.1	1.1	<0.1	60.7	<0.1	<0.1	<0.1	<0.1
	7	Hollandite	7.6		<0.1	<0.1	2.3	<0.1	46.8	<0.1	<0.1	7.9	<0.1
	8	Carbonaceous matter and hollandite	**33.9**	**25.8**	2.1	0.5	1.5	<0.1	33.3	3.9	<0.1	5.0	<0.1
	9	Hollandite and carbonaceous matter	10.0		<0.1	<0.1	0.8	<0.1	46.4	<0.1	<0.1	3.7	<0.1
	10	Hollandite and carbonaceous matter	8.3		<0.1	<0.1	0.8	<0.1	52.1	<0.1		3.7	<0.1

Fig. 11. (*continued*)

structures of Mn oxides) with biomass that is preserved in their pores, microbialites (Fig. 10.3A–D, 10.5A–E and 10.6A), globular, micronodular or spheroidal structures that show further inner spheroidal structures (Figs 8E–F, 9G–I), and enrichment in bio-essential elements P, Co, Ni and Cu (Fig. 15) are features that indicate microbial mediation during sedimentation of Mn-2 and Mn-3, which will be discussed in future chapters. Similar features from the action of microorganisms were found in Úrkut (Polgári et al. (2012a,b)). Mn-1 is different because it has no other features that suggest biogenic mediation during its formation, with the exception of the presence of bio-essential elements. The origin of the layers that comprise the Mn-1 unit will be discussed separately.

Krumbein (1983) and Ehrlich (1990) considered that the bacterial oxidation of Mn(II) to Mn (IV) and the consequent Mn (IV) sedimentation as manganohydrite could drive the oxidative segment of the global biogeochemical Mn cycle. More recently, Polgári et al. (2012a,b) and Bodor et al. (2016) confirmed the observations of Krumbein (1983) and Ehrlich (1990), determining that the most effective process of manganese precipitation in marine sedimentary environments with low temperatures (< 100 °C) is microbial. This process would be supported by the homogeneous oxidation of aqueous solutions and oxide surface catalysis, which were advocated by Morgan (2005). In this type of environment, the initiation of manganese sequestration in solution only occurs under oxidizing conditions and is probably aided by the multi-copper oxidase enzymatic process (Tebo et al., 1997; Villalobos et al., 2003, 2005, Morgan, 2005). However, according to Morgan (2005), manganese oxide precipitation is a consequence of a simple oxidation process of manganese solutions in an

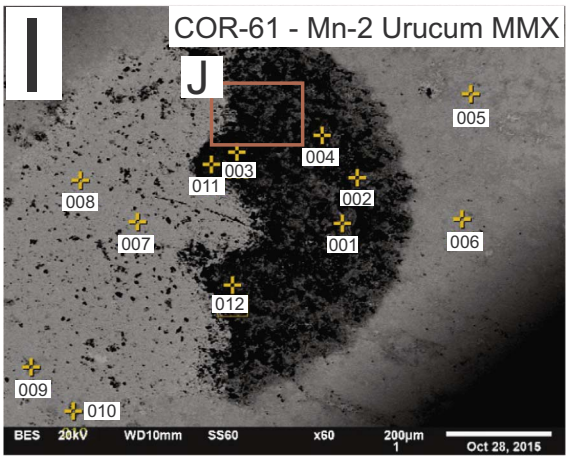

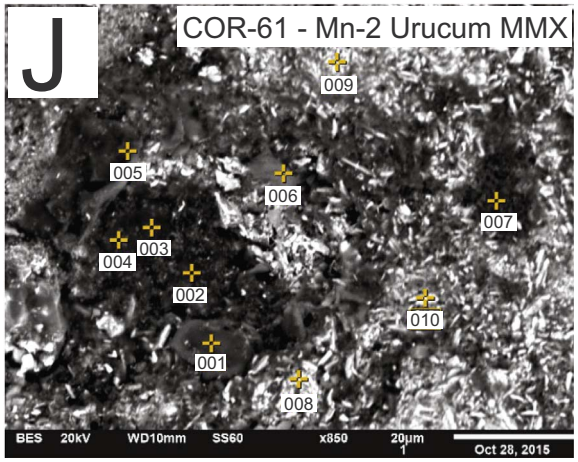

Figure	Point nº	Identification	C	Free C >	Si	Al	K	Na	Mn	Fe	Ca	Ba	P
11 I	1	Rhodochrosite and carbonaceous matter	17.8	8.1	<0.1	<0.1	<0.1	<0.1	44.2	<0.1	<0.1	<0.1	<0.1
	2	Rhodochrosite and carbonaceous matter	18.2	7.4	<0.1	<0.1	<0.1	<0.1	49.5	<0.1	<0.1	<0.1	<0.1
	3	Carbonaceous matter	69.3	68.4	2.7	<0.1	<0.1	<0.1	4.0	<0.1	<0.1	<0.1	<0.1
	4	Rhodochrosite and carbonaceous matter	43.9	37.6	0.4	<0.1	<0.1	<0.1	28.6	<0.1	<0.1	<0.1	<0.1
	5	Cryptomelane	<0.1		4.5	<0.1	0.6	<0.1	57.9	4.6	<0.1	<0.1	<0.1
	6	Cryptomelane	<0.1		<0.1	<0.1	2.5	<0.1	51.0	8.4	<0.1	<0.1	<0.1
	7	Hollandite	5.2		<0.1	<0.1	4.5	<0.1	52.5	<0.1	<0.1	3.7	<0.1
	8	Hollandite	<0.1		<0.1	<0.1	3.5	<0.1	54.9	<0.1	<0.1	7.6	<0.1
	9	Hollandite and carbonaceous matter	10.9		<0.1	<0.1	2.8	<0.1	54.8	<0.1	<0.1	2.4	<0.1
	10	Rhodochrosite and carbonaceous matter	19.4	10.1	<0.1	<0.1	1.7	<0.1	42.7	<0.1	<0.1	2.2	<0.1
	11	Rhodochrosite and carbonaceous matter	27.1	22.3	12.3	<0.1	0.6	<0.1	17.6	2.8	1.2	<0.1	<0.1
	12	Rhodochrosite and carbonaceous matter	39.4	30.7	<0.1	<0.1	0.7	<0.1	39.2	<0.1	0.6	<0.1	<0.1

Figure	Point nº	Identification	C	Free C >	Si	Al	K	Na	Mn	Fe	Ca	S	P
11 J	1	Carbonaceous matter	61.9	61.0	<0.1	<0.1	<0.1	<0.1	2.7	<0.1	0.9	0.5	1.4
	2	Carbonaceous matter	65.7	64.2	0.9	<0.1	<0.1	<0.1	6.9	<0.1	<0.1	<0.1	<0.1
	3	Carbonaceous matter	68.2	67.7	1.9	<0.1	<0.1	<0.1	2.2	<0.1	<0.1	<0.1	<0.1
	4	Carbonaceous matter	62.7	61.8	<0.1	<0.1	<0.1	<0.1	3.9	<0.1	<0.1	<0.1	<0.1
	5	Carbonaceous matter	67.6	66.1	1.5	<0.1	<0.1	<0.1	5.6	<0.1	0.9	<0.1	<0.1
	6	Carbonaceous matter	70.0	68.8	0.4	0.5	<0.1	0.5	5.7	<0.1	<0.1	<0.1	<0.1
	7	Carbonaceous matter	89.0	88.9	<0.1	<0.1	<0.1	<0.1	0.4	<0.1	<0.1	0.5	<0.1
	8	Rhodochrosite and carbonaceous matter	46.2	40.0	0.5	<0.1	<0.1	<0.1	28.4	<0.1	<0.1	<0.1	<0.1

Fig. 11. (*continued*)

oxidizing environment; Mn(II) is not oxidized to Mn(IV) without bacterial mediation. The reason for this phenomenon is the atomic structure (distribution of electrons) of Mn(II), which requires different amounts of energy for the displacement of two electrons to form Mn (IV). A substantial free energy barrier exists to a second one-electron oxidation step, which is inner-sphere path transfer, because the energy

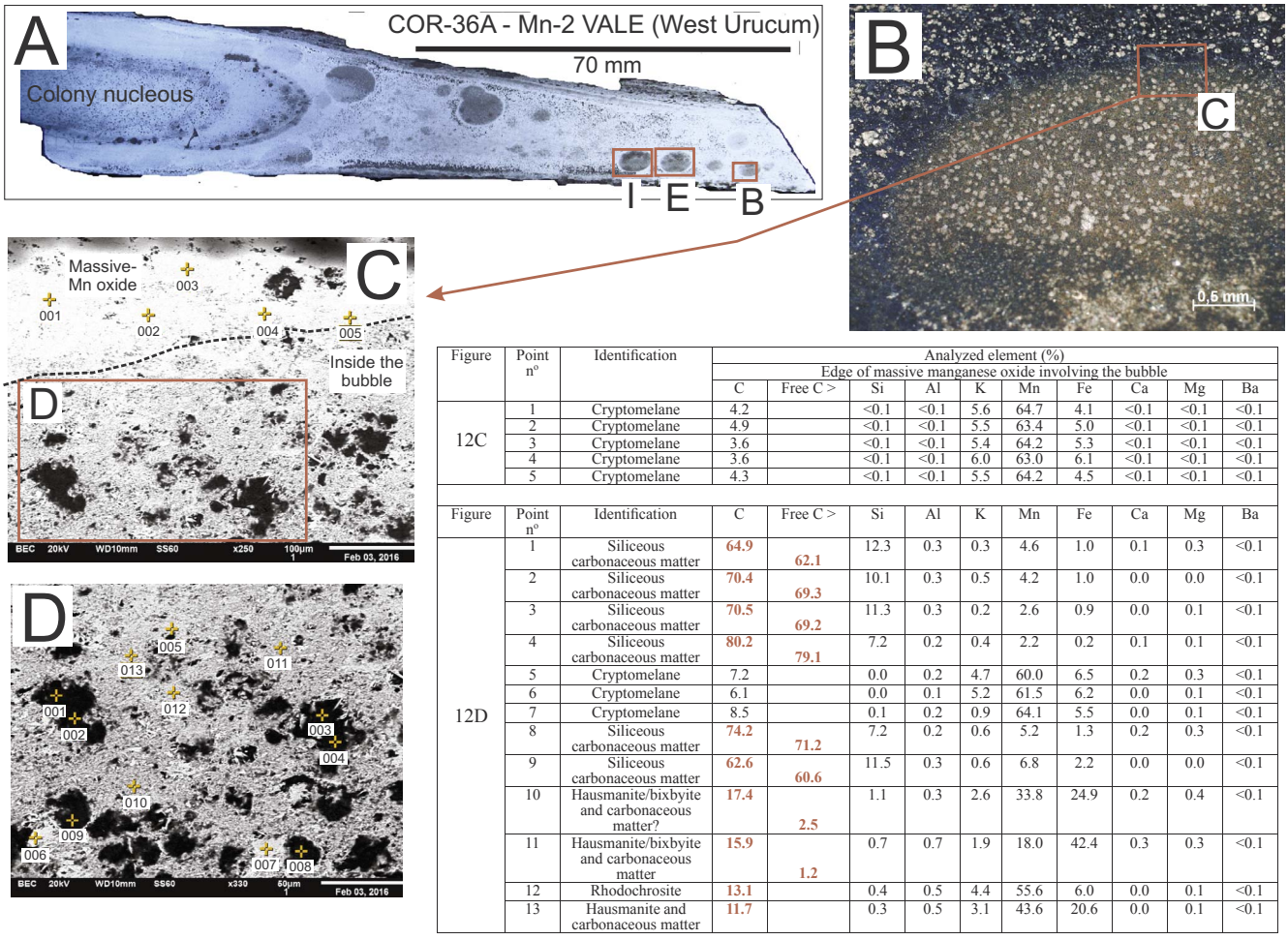

Figure	Point n°	Identification	Analyzed element (%)									
			Edge of massive manganese oxide involving the bubble									
			C	Free C >	Si	Al	K	Mn	Fe	Ca	Mg	Ba
12C	1	Cryptomelane	4.2		<0.1	<0.1	5.6	64.7	4.1	<0.1	<0.1	<0.1
	2	Cryptomelane	4.9		<0.1	<0.1	5.5	63.4	5.0	<0.1	<0.1	<0.1
	3	Cryptomelane	3.6		<0.1	<0.1	5.4	64.2	5.3	<0.1	<0.1	<0.1
	4	Cryptomelane	3.6		<0.1	<0.1	6.0	63.0	6.1	<0.1	<0.1	<0.1
	5	Cryptomelane	4.3		<0.1	<0.1	5.5	64.2	4.5	<0.1	<0.1	<0.1

Figure	Point n°	Identification	C	Free C >	Si	Al	K	Mn	Fe	Ca	Mg	Ba
12D	1	Siliceous carbonaceous matter	64.9	62.1	12.3	0.3	0.3	4.6	1.0	0.1	0.3	<0.1
	2	Siliceous carbonaceous matter	70.4	69.3	10.1	0.3	0.5	4.2	1.0	0.0	0.0	<0.1
	3	Siliceous carbonaceous matter	70.5	69.2	11.3	0.3	0.2	2.6	0.9	0.0	0.1	<0.1
	4	Siliceous carbonaceous matter	80.2	79.1	7.2	0.2	0.4	2.2	0.2	0.1	0.1	<0.1
	5	Cryptomelane	7.2		0.0	0.2	4.7	60.0	6.5	0.2	0.3	<0.1
	6	Cryptomelane	6.1		0.0	0.1	5.2	61.5	6.2	0.0	0.1	<0.1
	7	Cryptomelane	8.5		0.1	0.2	0.9	64.1	5.5	0.0	0.1	<0.1
	8	Siliceous carbonaceous matter	74.2	71.2	7.2	0.2	0.6	5.2	1.3	0.2	0.3	<0.1
	9	Siliceous carbonaceous matter	62.6	60.6	11.5	0.3	0.6	6.8	2.2	0.0	0.0	<0.1
	10	Hausmanite/bixbyite and carbonaceous matter?	17.4	2.5	1.1	0.3	2.6	33.8	24.9	0.2	0.4	<0.1
	11	Hausmanite/bixbyite and carbonaceous matter	15.9	1.2	0.7	0.7	1.9	18.0	42.4	0.3	0.3	<0.1
	12	Rhodochrosite	13.1		0.4	0.5	4.4	55.6	6.0	0.0	0.1	<0.1
	13	Hausmanite and carbonaceous matter	11.7		0.3	0.5	3.1	43.6	20.6	0.0	0.1	<0.1

Fig. 12. (A) Oblate kremydilite core with spherical structures outside the core. (B) Optical image under RL. (C, D) SEM images of parts of the internodular bubble in B (Image 11A). The bubbles are surrounded by massive cryptomelane (Images B and C). Inside the bubble (Image D) the pores (black) contain silica-rich carbonaceous matter amid reflective matrix whose composition is compatible with hausmannite/bixbyite. (E) Optical image of the bubble in E (Fig. 12A). (F–H) SEM images and EDS analyses of the inside of the bubble, which is composed of substances whose compositions are consistent with those of rhodochrosite, hausmannite, and silica-rich carbonaceous matter. (I) Optical image of the bubble in I (Fig. 12A). (J, K) SEM images and EDS analyses of the inside of the bubble in I, which is surrounded by massive cryptomelane (Images I, J), and its interior contains rhodochrosite combined with silica-rich carbonaceous matter (Images J, K).

requirement to transform Mn(III) into Mn(IV) is more than twice the amount to transform Mn(II) into Mn(III). Therefore, the energy in chemical oxidizing environments without bacterial mediation is insufficient for the complete oxidation of manganese and the precipitation of $Mn(OH)_4$ (Bargar et al., 2005; Webb et al., 2005). If microbial mediation occurred during the sedimentation of Mn-2 and Mn-3, then the environment was oxidizing. Additionally, Mn(II) oxidation is facilitated by a diverse array of microbe and fungi (Tebo et al., 1997, 2004), which suggests that this process is fundamental and ubiquitous (Webb et al., 2005). According to laboratory experiments (Moffett and Ho, 1996), oxidizing microbe can also oxidize Co, Ni, Cu and Ce (Villalobos et al., 2003; Bodeï et al., 2008) and precipitate these elements together with manganese.

The oxidation of Fe, which immediately occurs under homogeneous chemical oxidizing conditions, is a distinct process from microbially mediated suboxic Fe(II) oxidation, but both can occur simultaneously. Fe(II) oxidation is facilitated by a diverse array of microbe, but the micro-organisms' metabolisms are different. Among the four types of known microbial metabolisms that can oxidize Fe(II) to form Fe (III) oxide minerals (Konhauser, 1998), the most likely in environments such as the Urucum basin are as follows. (a) Microbial Fe(II) metabolism that is driven by light. This process is anoxic/anaerobic and neutrophilic (photoferrotroph) and is very important for the formation of BIF. (b) Metabolism that is driven by suboxic and neutrophilic Mariprofundus ferrooxidans-like Fe-oxidizing microbes, which are very widespread, but their existence during the Neoproterozoic has not been proven. Non-enzymatic reactions provide an indirect role for bacteria in the oxidation of Fe. The physical conditions (Eh, pH) change around the cells because of microbial activity, favoring the chemical oxidation of Fe.

The result of microbially mediated Fe(II) oxidation is ferrihydrite, which is rather poorly ordered and adsorbs colloidal silica. Ferrihydrite transforms to more stable Fe-oxides (hematite, goethite, etc.). These transmissions are determined by the conditions of the system (e.g., organic content) and are accompanied by silica segregation. The direct precipitation of amorphous silica requires high concentrations, more than 120–140 ppm (Baele et al., 2008), which is not usual in sedimentary environments but is common in hydrothermal settings. Amorphous silica can easily transform into more stable minerals, such as cristobalite, tridymite, and quartz (Herdianita et al., 2000). BIFs, which locally host Mn-1 and Mn-2, may have been formed by similar iron and silica sedimentation processes (Posth et al., 2008, 2013). According to these authors, the biotic nucleation of $Fe(OH)_3$ in seawater at temperatures around 15–25 °C generates an organic wrap around the hydroxide particles, which prevents silica adsorption and causes ferrihydrite precipitation and the retention of silica in solution, thereby generating ferruginous sediments with low silica concentrations. At temperatures below 15 °C, the microbial activity decreases or

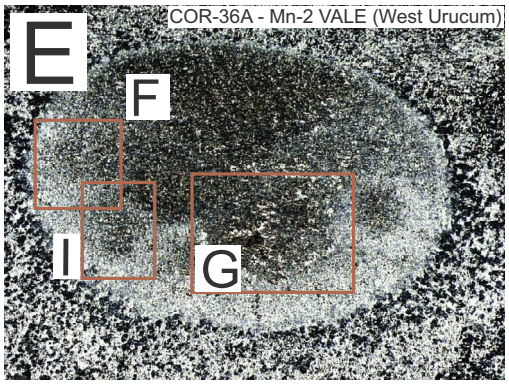

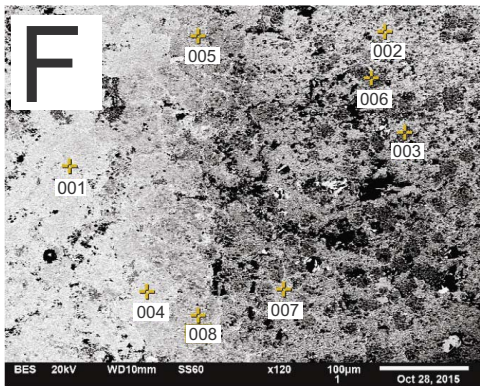

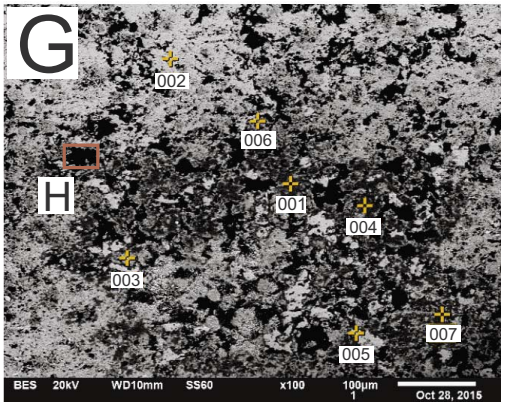

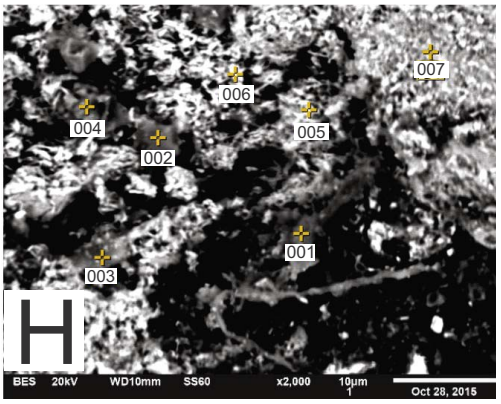

Fig. 12. (*continued*)

Figure	Point nº	Identification	C	Free C >	Si	Al	K	Mn	Fe	Ca	Mg	Ba
12F	1	Cryptomelane	7,3		<0.1	1,2	4,5	37,6	0,34	<0.1	<0.1	<0.1
	2	Rhodochrosite and carbonaceous matter	14.8	8.8	0,3	0,8	3,4	26,8	0,44	<0.1	<0.1	<0.1
	3	Rhodochrosite and carbonaceous matter	16.6	11.9	<0.1	0,9	3,4	21,2	0,33	<0.1	<0.1	<0.1
	4	Rhodochrosite and carbonaceous matter	7,8	1.9	<0.1	1,7	3,9	26,2	0,76	<0.1	<0.1	<0.1
	5	Carbonaceous matter and rhodochrosite	19,5	15.6	<0.1	0,9	2,8	16,8	1,02	<0.1	<0.1	<0.1
	6	Siliceous carbonaceous matter and hausmanite	28.8	25.0	10,8	<0.1	<0.1	5,7	11,8	<0.1	<0.1	<0.1
	7	Carbonaceous matter and hausmanite	33,9	29.9	<0.1	0,5	1,9	9,4	9,17	<0.1	<0.1	<0.1
	8	Carbonaceous matter and rhodochrosite?	29,7	26.8	1,1	0,8	2	9,9	3,33	<0.1	<0.1	<0.1

Figure	Point nº	Identification	C	Free C >	Si	Al	K	Mn	Fe	Ca	Mg	Ba
12G	1	Siliceous carbonaceous matter	45.6	43.4	6.4	0.6	0.8	6.6	2.8	0.6	<0.1	<0.1
	2	Rhodochrosite and carbonaceous matter	13.8	7.8	<0.1	0.8	3.4	27.3	<0.1	<0.1	<0.1	<0.1
	3	Rhodochrosite and carbonaceous matter	32.6	27.1	<0.1	1.1	3.4	25.0	<0.1	<0.1	<0.1	<0.1
	4	Siliceous carbonaceous matter	47.1	46.8	9.2	0.5	<0.1	1.3	<0.1	<0.1	<0.1	<0.1
	5	Rhodochrosite and carbonaceous matter	13.2	7.5	<0.1	<0.1	<0.1	26.1	<0.1	<0.1	<0.1	<0.1
	6	Siliceous carbonaceous matter	65.5	65.2	4.8	0.3	<0.1	1.5	<0.1	<0.1	<0.1	<0.1
	7	Siliceous carbonaceous matter	50.1	49.5	4.7	<0.1	<0.1	2.6	<0.1	<0.1	<0.1	<0.1

Figure	Point nº	Identification	C	Free C >	Si	Al	K	Mn	Fe	Ca	Mg	Ba
12H	1	Rhodochrosite and carbonaceous matter	33.7	30.4	2.3	0.6	1.8	15.1	<0.1	<0.1	<0.1	<0.1
	2	Hausmanite and carbonaceous matter	23.9	19.0	1.4	1.1	1.4	15.1	7.3	<0.1	<0.1	<0.1
	3	Rhodochrosite and siliceous carbonaceous matter	35.6	32.6	6.1	<0.1	0.9	10.6	3.4	<0.1	<0.1	<0.1
	4	Hausmanite and carbonaceous matter	16.3	10.1	2.0	0.7	2.3	19.2	9.5	<0.1	<0.1	<0.1
	5	Rhodochrosite and hausmanite carbonaceous matter	29.2	23.9	1.6	0.8	2.3	18.5	5.9	<0.1	<0.1	<0.1
	6	Byxbyite and carbonaceous matter	17.2	10.4	1.4	0.9	1.6	15.5	15.9	<0.1	<0.1	<0.1
	7	Rhodochrosite and carbonaceous matter	40.5		<0.1	0.6	1.6	11.5	<0.1	<0.1	<0.1	<0.1

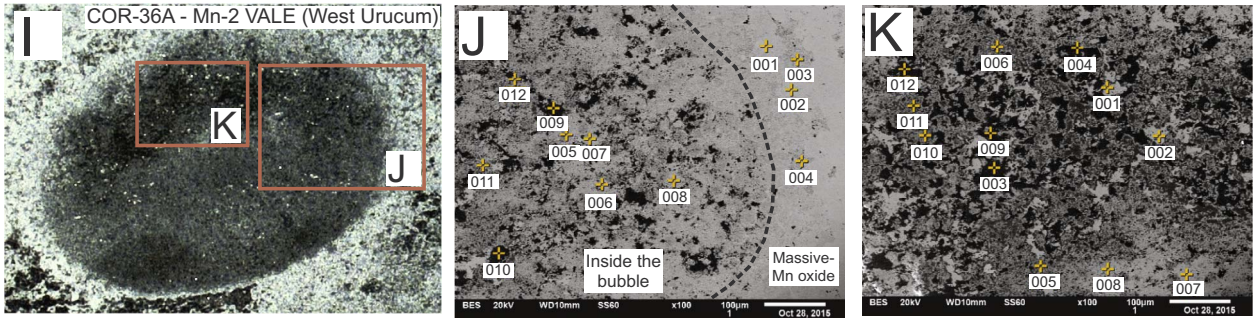

Figure	Point nº	Identification	C	Free C >	Si	Al	K	Mn	Fe	Ca	Mg	Ba
12 J	1	Rhodochrosite and carbonaceous matter	12.6	6.2	<0.1	0.9	3.8	29.2	<0.1	<0.1	<0.1	<0.1
	2	Rhodochrosite and carbonaceous matter	12.4	6.7	<0.1	1.2	3.5	25.9	<0.1	<0.1	<0.1	<0.1
	3	Hausmanite and carbonaceous matter	20.3	16.1	0.8	0.6	1.6	10.9	8.3	<0.1	<0.1	<0.1
	4	Rhodochrosite?	22.2		<0.1	0.8	2.2	15.9	<0.1	<0.1	<0.1	<0.1
	5	Carbonaceous matter and rhodochrosite	35.5	18.7	2.7	0.8	1.8	10.1	<0.1	<0.1	<0.1	<0.1
	6	Carbonaceous matter and rhodochrosite	27.1		1.3	0.9	2.2	9.8	<0.1	<0.1	<0.1	<0.1
	7	Carbonaceous matter and rhodochrosite	32.1	33.3	1.2	0.6	0.9	3.8	<0.1	<0.1	<0.1	<0.1
	8	Carbonaceous matter and rhodochrosite	31.2	25.0	0.5	<0.1	1.2	6.9	<0.1	<0.1	<0.1	<0.1
	9	Siliceous carbonaceous matter	55.7	31.3	7.7	<0.1	<0.1	<0.1	<0.1	<0.1	<0.1	<0.1
	10	Siliceous carbonaceous matter	49.9	29.7	7.7	<0.1	<0.1	<0.1	<0.1	<0.1	<0.1	<0.1
	11	Siliceous carbonaceous matter	57.3	55.7	5.5	<0.1	<0.1	<0.1	<0.1	<0.1	<0.1	<0.1
	12	Siliceous carbonaceous matter Siliceous carbonaceous matter	35.7	49.9	6.37	<0.1	1.14	5.4	3.02	<0.1	<0.1	<0.1

Figure	Point nº	Identification	C	Free C >	Si	Al	K	Mn	Fe	Ca	Mg	Ba
12K	1	Rhodochrosite and carbonaceous matter	8.7	0.9	<0.1	<0.1	<0.1	35.7	<0.1	<0.1	<0.1	<0.1
	2	Rhodochrosite and carbonaceous matter	16.4	10.1	<0.1	<0.1	<0.1	28.7	<0.1	<0.1	<0.1	<0.1
	3	Siliceous carbonaceous matter	54.4	54.4	14.0	<0.1	<0.1	<0.1	<0.1	<0.1	<0.1	<0.1
	4	Carbonaceous matter and rhodochrosite	30.1	27.3	3.9	0.6	1.9	12.6	<0.1	<0.1	<0.1	<0.1
	5	Carbonaceous matter and rhodochrosite	35.1	32.9	4.6	0.5	1.0	7.0	3.3	<0.1	<0.1	<0.1
	6	Carbonaceous matter and rhodochrosite	33.6	31.9	3.8	0.8	1.6	7.6	<0.1	<0.1	<0.1	<0.1
	7	Carbonaceous matter and rhodochrosite	25.4	23.0	1.2	<0.1	1.0	5.4	5.5	<0.1	<0.1	<0.1
	8	Carbonaceous matter and rhodochrosite	23.1	21.7	1.1	0.7	1.5	6.5	<0.1	<0.1	<0.1	<0.1
	9	Siliceous carbonaceous matter	56.0	56.0	8.2	<0.1	<0.1	<0.1	<0.1	<0.1	<0.1	<0.1
	10	Siliceous carbonaceous matter	39.1	37.7	5.4	0.6	0.7	4.8	1.5	<0.1	<0.1	<0.1
	11	Carbonaceous matter and rhodochrosite	29.9	27.5	2.6	<0.1	1.6	9.5	1.6	<0.1	<0.1	<0.1
	12	Rhodochrosite and carbonaceous matter	16.6	13.4	1.48	0.97	2.63	14.8		<0.1	<0.1	<0.1

Fig. 12. (*continued*)

disappears, allowing the nucleation of ferrihydrites with absorbed silica and/or the direct precipitation of only silica. This relationship is less evident in the iron-rich rocks in layer Mn-1, in which the total SiO_2 is the sum of the silica in the jaspilite, quartz, and other silicates.

Phosphate is essential to life, particularly in the production of DNA, RNA, and ATP (adenosine triphosphate) and as a constituent of cellular

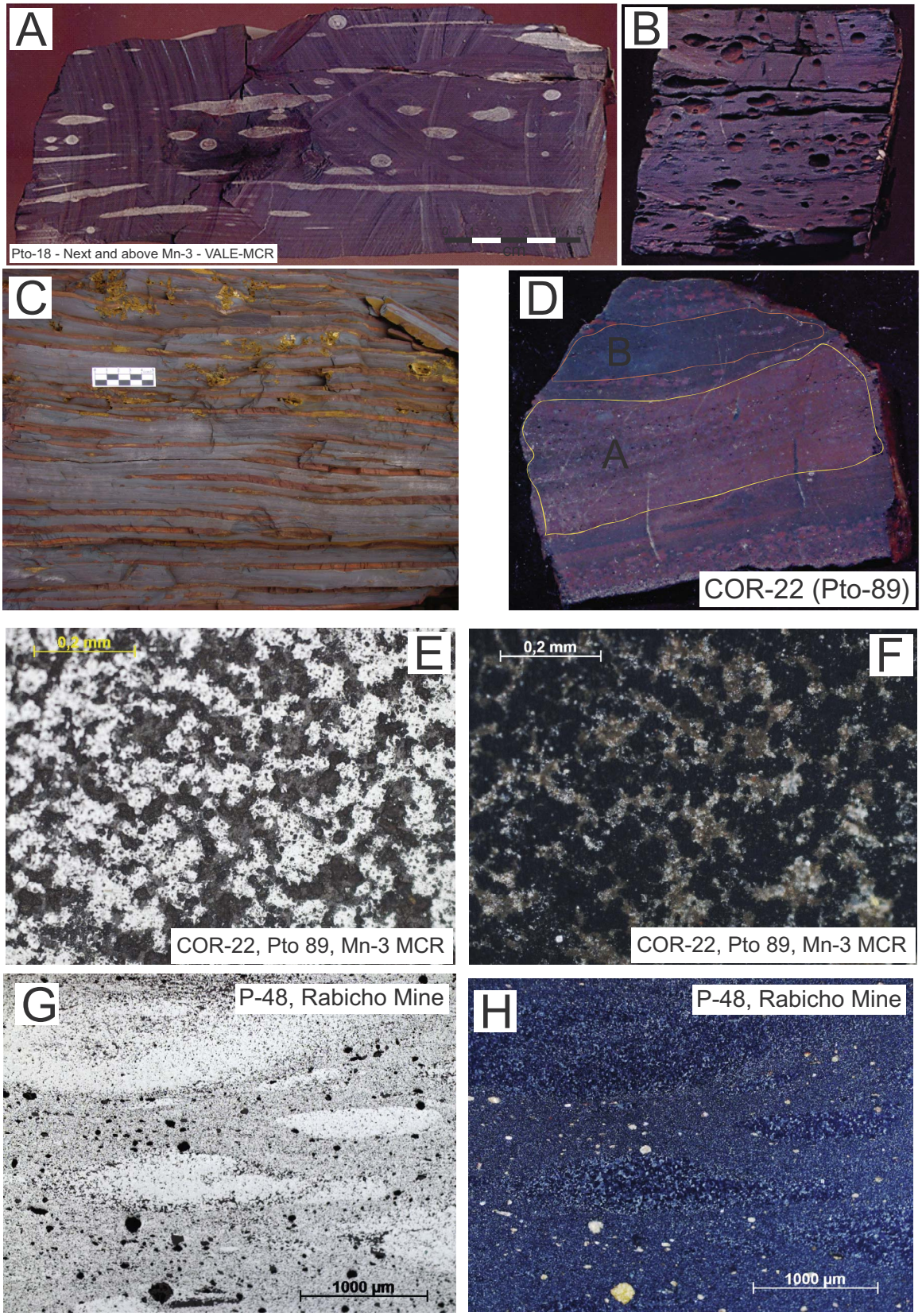

Fig. 13. Iron-rich rocks hosting massive Mn ore layers in the Urucum region. (A) Ferruginous jaspillite with silica nodules and microlenses. (B) Most common type of iron ore (silica-leached jaspilite and IFs) in the Urucum region. (C) Most common BIF in the Urucum region. (D) Sample from the transition zone between the jaspilite and layer Mn-2 or Mn-3. (E, F) Photomicrographs of ferruginous chert with recrystallized hematite and quartz. In E, the reflective portions are hematite, and the dark portions are quartz (RL, //N). F shows the same image, under RL, xN. (G–H) Photomicrographs of detritic iron ore from the Rabicho deposit, with microcrystalline hematite matrix and massive hematite lenses (RL; G with //N, and H with xN).

membranes, and a lack of phosphate constrains microbial activity (Bjerrum and Canfield, 2002). Therefore, the highest P_2O_5 concentrations should occur in rocks whose origins involved significant biogenic activity. The phosphorous concentrations (Fig. 15) produced a grouping of manganese ores, similar to that from produced by the concentrations of Mn and Si. Thus, the high phosphate contents, the geological and chemical features that indicate biogenesis, and the necessarily biogenic conditions for the oxidation of Mn(II) to Mn (IV) indicate the biotic sedimentation of the Mn-2 and Mn-3 ore layers in an oxidizing environment. The absence of these features in IFs that host Mn-2 and Mn-3, suggests that homogeneous chemical oxidation and ferrihydrite sedimentation prevailed, which immediately happens. With the exception of the iron-rich rocks that host layer Mn-3 in the MCR Mine, all the iron-rich units above layer Mn-1 may have been abiotic if deposited during episodes of no tectonic activity. When hosted by BIFs or silica-rich IFs, ferrihydrites nucleation may have been driven by microbes in suboxic environments below the oxyline after episodes of flooding and hydrothermalism.

According to Moffett and Ho (1996) and Jiao et al. (2005), cobalt is involved in Fe(II) and Mn(II) oxidation through phototrophic oxidizing bacteria. In addition to biogenic participation, the Co concentrations in Mn-1 must also have been influenced by the sorption of Co to Mn (hydr) oxides and clay minerals, which explains the higher Co concentrations in the clayey portions of Mn-1. The clay mineral content decreases from Mn-1 to Mn-2 and Mn-3, so the Co concentrations proportionally decrease (Fig. 15). The presence of high Ni and Cu concentrations only in the detrital Mn ores of layer Mn-1 in the Rabicho Mine (Fig. 15) makes establishing a genetic correlation difficult, which would suggest that the ancient Mn ores formed before the opening of the basin.

We can draw some additional conclusions by combining the information in Figs. 14 and 15 and the discussion regarding the Mn(II) and Fe(II) oxidation from microorganisms. (a) Layers Mn-2 and Mn-3, which contain high P and Co concentrations and very little silica, were generated by biotic processes in an oxidizing environment. (b) Mn-1's phosphate, cobalt, and nickel (and Cu?) concentrations were influenced by the presence of clastic apatite and clay minerals, but the very high concentrations of P and Ni in the host IFs suggest that some additional processes were important in the formation of these rocks, which will be discussed in the chapter that discusses Mn-1's genesis. (c) The IFs above layer Mn-1, which have low silica concentrations and are devoid of phosphorous, cobalt, and manganese, were probably generated mainly by abiotic processes. When silica and bio-essential elements were present, as was the case for the BIFs, sedimentation occurred with biogenic mediation in a suboxic environment. The IFs that host layer Mn-3 in the MCR Mine are exceptions. Their high phosphorous content indicates that biotic processes may have been active during sedimentation (Fig. 15). (d) During diagenesis, cryptomelane was and continues to be transformed into hollandite because of weathering.

6.2.2. Rare earth elements (REE) chemistry

Debris from turbidite flows and wind may alter the original REE composition of chemical sediments, especially when this debris originates from the erosion of granitic rocks with apatite and allanite. The manganese ores from Urucum do not have alumina ore minerals, so the Al_2O_3 contents are good indicators of the presence of silicates. In geological environments such as Urucum, silicates are mostly clay minerals and fragments of feldspar, which are potential REE carriers. Table 1 shows that only rocks from the Mn-1 unit contained significant Al_2O_3 contents (greater than 1.0%), and Fig. 14D indicates that the alumina minerals did not influence the distribution of REEs, which will be discussed below. The microbial sedimentation of manganohydrites may also oxidize and precipitate Ce (Moffett and Ho, 1996). This information imposes caution on the interpretation of the REE models of Mn-2 and Mn-3 (Fig. 16C–D) and BIFs (Fig. 17A–B), rocks that were probably deposited under the influence of microbes, but are less important in the case of the massive IFs (without clay minerals) that host Mn-2 and Mn-3 (Figs. 7 and 16E–F). The sedimentation of Mn-1 (Fig. 16A–B) was predominantly clast-chemical with subordinate influence from microbes, so we can also discuss the geochemistry of the REEs of this layer.

The similarities between the REE model for the IFs (Fig. 16E–F) and that of the arkosic iron-rich rocks that host the manganese ore layers (Fig. 16G–H) and the differences between these models and those for layers Mn-2 and Mn-3 (Fig. 16C–D) complicate the discussion of the origin of these rocks. Although the IFs' convex MREE patterns are similar to those of sediments from hydrothermal fluids that are emitted from vents along modern mid-ocean ridges (Michard et al., 1983; Michard, 1989; German and Elderfield, 1990a,b; German et al., 1995), a hypothesis should be considered in which the Urucum mineralizing fluids originated from hydrothermal vents, and microbial mediation during Mn-2 and Mn-3's sedimentation may have influenced the REE patterns of these layers.

In the Urucum region, the most likely possibility is that the seawater composition during periods of tectonic activity was influenced by submarine exhalations from vents at the base of the Chiquitos–Tucavaca aulacogen (Schobbenhaus et al., 1981; Litherland et al., 1989; Alvarenga and Trompette, 1994; Trompette et al., 1998; Angerer et al., 2016; D'el-Rey Silva et al., 2016). This phenomenon would have mainly occurred in the Urucum Basin region, where the aulacogen overlaps the Paraguay Fold Belt, possibly forming a region of crustal weakness. These vents were likely located below the Santa Cruz Formation in the Urucum region of Brazil and below rocks from the Boqui Group in Bolivia, and the hydrothermal fluids likely acquired similar REE distribution patterns to those of basement granites that were crossed by the vent-feeding channels. The feldspars in the arkosic sediments at the base of these units make them compositionally similar to basement granites, so their REE patterns may also be similar. Therefore, with the exception of the Mn-rich ore layers, the sediment REE patterns were inherited from hydrothermal fluids that were emitted from vents on the floor of the Urucum Basin, which subsequently mixed with seawater (Fig. 18B–E and H–I). Another possibility to consider is that partial Ce^{4+} to Ce^{3+} reduction occurred at the top of the mud layer on the floor of the Urucum Basin, just below the oxycline (Fig. 18G), increasing the relative solubility, so the Ce concentration in the water increased from the dissolution of Mn–Fe hydroxides (Bau et al., 1997). In deeper anoxic zones, the progressive dissolution of hydroxide particles fractionated REEs through the selective dissolution of LREEs over HREEs, ultimately generating a nearly flat dissolved REE pattern (Fig. 16B and D) with a discrete Ce anomaly (Bau et al., 1997).

The absence of significant Eu anomalies in the manganese ores and the host iron-rich rocks (Fig. 16) indicates that low-temperature ($< 150\,^{\circ}C$) hydrothermal fluids fertilized the seawater with metals (Dymek and Klein, 1988; Danielson et al., 1992; Bau and Möller, 1993; Bau and Dulski, 1996, 1999; Ohmoto et al., 2006; Bolhar and Van Kranendonk, 2007; Planavsky et al., 2010). Graf et al. (1994) interpreted the absence of Eu anomalies in the rocks from the Santa Cruz Formation as a consequence of fluids interacting with rocks that displayed negative Eu anomalies, such as the basement granites. However, analyses in more recent works (Redes et al., 2015) showed that the basement granites have a positive Eu (normalized to the NASC) anomaly averaging 1.25, slightly larger than 1.04 (s.d. = 0.07; n = 80), which is the average value of the Eu anomalies of the Urucum manganiferous and ferruginous rocks (Table 1). According to the deep exhalative alteration hypothesis of Kimberley (1989), the fluids that are responsible for ironstone deposition can access several segments of the crust along continental margins. A range of REE signatures is possible depending on the exact crustal volume along the circulation path, and different fluid–rock interactions may attenuate the anomaly values of the basement granites, resulting in slightly lower positive anomalies. Another possibility is that the very small Eu enrichment was a consequence of the introduction of hydrothermal fluids from deep seawater into the Urucum Basin (Dardenne, 1998). Both factors likely influenced

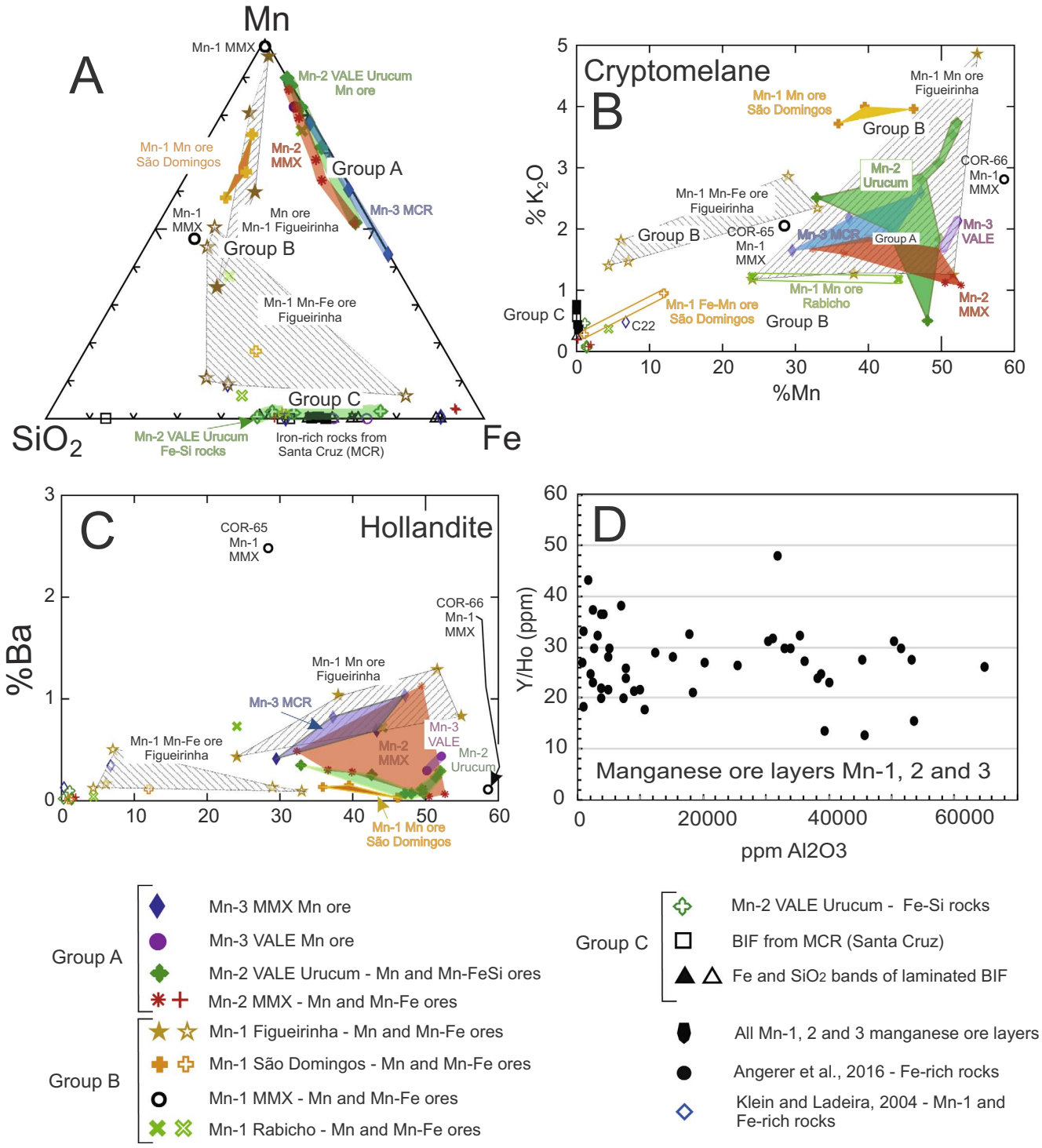

Fig. 14. Chemical compositions of manganese ores and related iron-rich rocks from the Urucum region. (A) SiO_2–Mn–$Fe_{(Total)}$ ternary diagram. (B) Mn vs. K_2O diagram for distinguishing rocks based on their cryptomelane concentrations. (C) Mn vs. Ba diagram for distinguishing rocks based on their hollandite concentrations. (D) Al_2O_3 vs. Y/Ho diagram for manganese ore layers.

the absence of an Eu anomaly, as shown in Fig. 16.

Based on these data, Mn-2 and Mn-3 were generated by microorganism-rich water that was brought by floods, and the REE patterns were a consequence of this origin. Modifications in the REE patterns from microbial mediation were probably less important during the sedimentation of Mn-1 and the IFs that host Mn-1, Mn-2 and Mn-3 because microbial activity did not exist or was only slightly active during these periods. The REE patterns of these layers were controlled by homogeneous oxidation, the intensity of the hydrothermalism and the depth variation of the Urucum basin.

In general, the Ce/Ce* values exceeded 1.15 where biogenic mediation may have influenced the precipitation of REEs. The exceptions were the REE patterns of layers Mn-1 from the Rabicho Mine and Mn-3 from the MCR Mine, which differed from all the others and yielded positive Ce anomalies (Figs. 15 and 16B–D). Layer Mn-1 from the Rabicho Mine showed clear enrichment in HREEs, whereas Mn-3 layer from the MCR Mine was depleted in HREEs. These differences were probably a consequence of the reworked clastic sedimentation of the

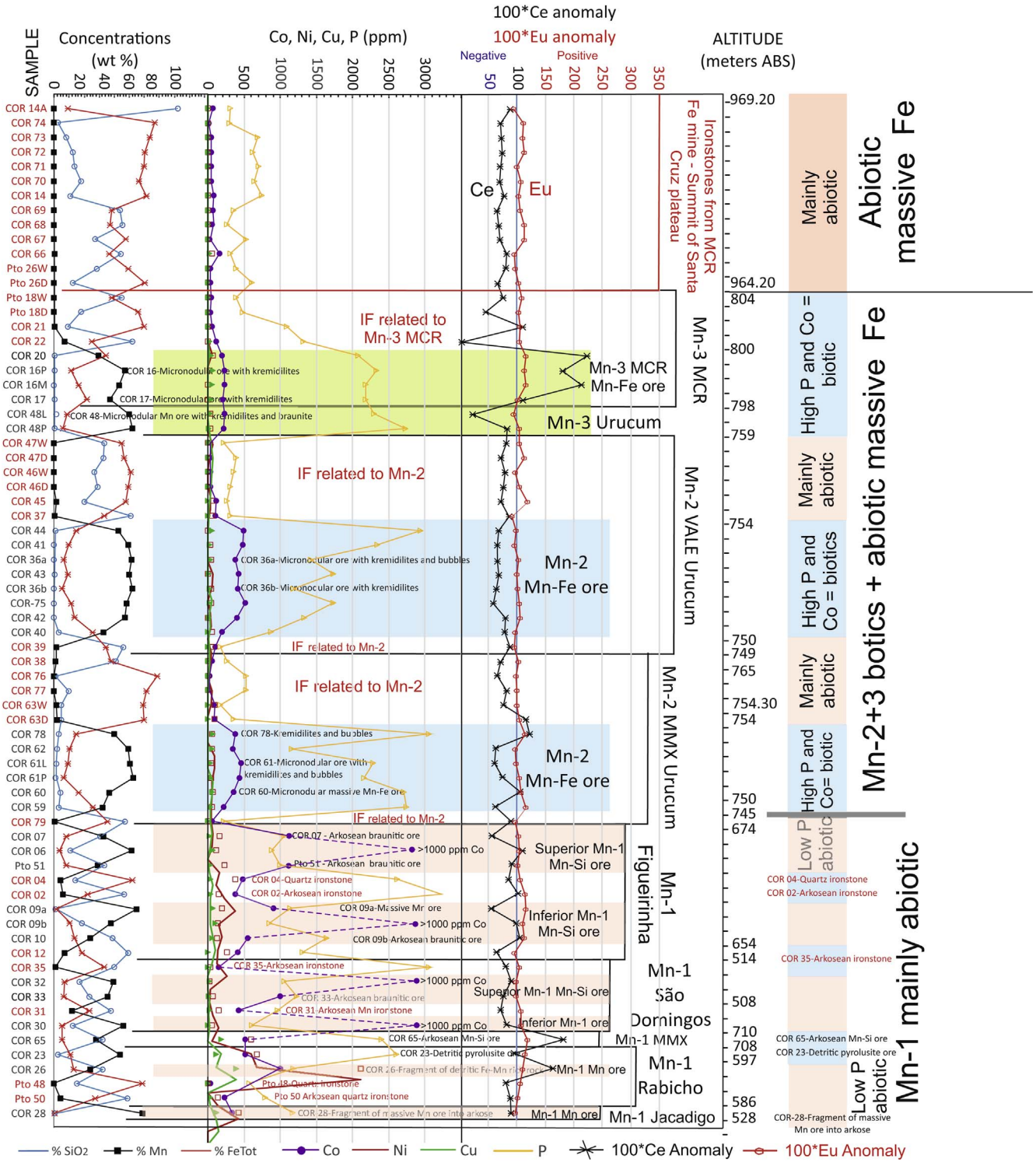

Fig. 15. Variations in SiO_2, Mn, Fe_{Total}, Cu, Co, Ni, and P concentrations and Ce and Eu anomalies in the various Mn ore layers and their Fe-rich host rocks in the Urucum mines, and in ironstone from the MCR Mine, arranged according to their stratigraphic positions. Values under the heading *Altitude* are the elevations of the base and top of each rock horizon. The two right-hand columns show interpretations of the genesis of the ore layers. See explanations in the text.

manganese oxides from the Rabicho mine and the hydrothermal proximal origin of layer Mn-3 from the MCR, which will be discussed below.

6.3. Genesis of Mn-1

Periods of tectonic instability likely caused several episodes of collapse at the bottom of the Urucum Graben, deepening and widening the river valley (Fig. 18A). All these periods of tectonic activity caused avalanches and flows of fine debris towards the bottom of the graben. As the Urucum graben opened and deepened, it was first flooded to a great depth with iron- and manganese-rich, cold and reduced seawater that was enriched in CO_2 (Fig. 18B). The direct contact of this seawater with the red beds of the Urucum Formation caused rapid heating, strong homogeneous water oxidation and the death of microorganisms.

This inundation caused the infiltration of seawater that was rich in iron, manganese, dead microorganisms and silica directly into pore

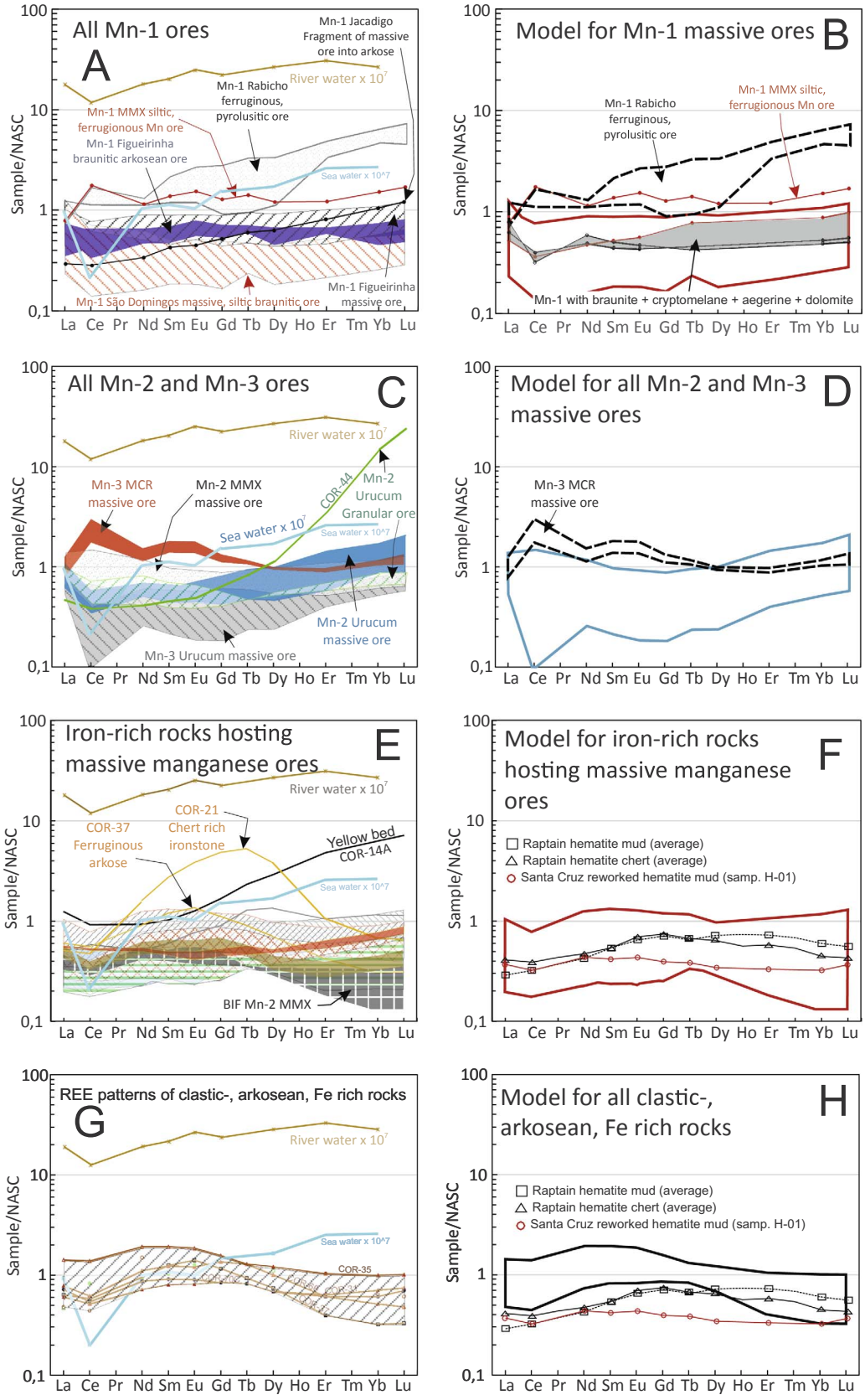

Fig. 16. REE patterns for the Urucum manganese ore layers and their iron-rich host layers. (A, C, E, G) REE patterns for all samples from each layer. (B, D, F, H). Contour plots of all REE patterns, which are referred to as the REE models for the various rock types. The sample collection sites and the rock type are indicated within each figure. Data taken from Klein and Ladeira (2004), for Mn-1 samples containing braunite cryptomelane + aegirine + dolomite, has been inserted in Fig. 16B. Data from Halverson et al. (2011), showing the average compositions of mud and chert from the Rapitan Group (Canada) and iron-rich rocks (Angerer et al., 2016) from the Santa Cruz deposit (Urucum), has been inserted in Fig. 16F. River water data from Gromet et al. (1984). All of the data were normalized using the NASC (North American Shale Composite) of Gromet et al. (1984).

spaces in the permeable, oxidizing continental sediments of the Urucum Formation. According to Morgan (2005), iron oxidation requires less energy than manganese, so iron, which was chemically homogeneous, oxidized first, thereby filling the pore spaces and fractures and cementing clastic rocks with iron oxides (Figs. 2D–E, 6H–K and 18C–D). The oxidized seawater, which was depleted in iron and enriched in manganese, precipitated Mn-oxide mineral (cryptomelane + bixbyite + hausmannite ± hollandite after diagenesis) and,

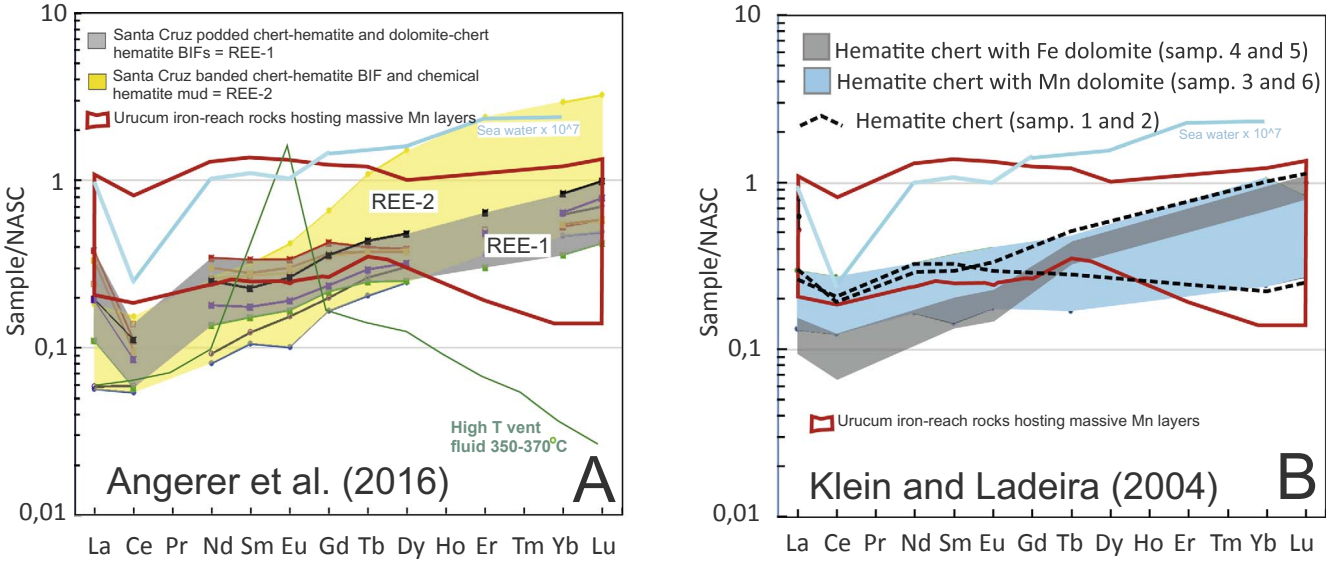

Fig. 17. Comparison of the REE model for the iron-rich rocks hosting the massive manganese ore layers in the Urucum region (this work), with (A) the Santa Cruz deposit iron ore (modified from Angerer et al., 2016) and high-temperature vent fluids (Bau and Dulski, 1999); (B) the compositions of hematite chert devoid of carbonate and hematite chert with manganoan and ferroan carbonates (Klein and Ladeira, 2004).

locally, siderite and rhodochrosite in the clastic rock pores, preserving the sedimentary structures (Fig. 6D) and forming the Lower Mn-1 ore layer. If this sedimentation phase was mediated by microbes, the Mn oxides probably precipitated under aerobic conditions, where microbial Mn(II) enzymatic oxidation resulted in the fine-grained accumulation of Mn oxides (cycle I, of Polgári et al., 2012a), which later transformed to Ca-rhodochrosite via bacterially mediated processes during suboxic early diagenesis (cycle II). After pore saturation, manganese hydroxides continued to precipitate on the basin floor with the simultaneous deposition of clay and rock fragments by turbidity flows, forming the Upper Mn-1 ore layer, which is characterized by banded manganese- and iron-rich rocks (Fig. 6B) and amygdalites (Fig. 6C). The simultaneous sedimentation of manganese, iron, REE and dead microorganisms, transferred bio-essential elements to the mud on the floor of the Urucum basin, as indicated by the very high concentrations of bio-essential elements and negative Ce anomalies in the Mn-1 unit (Fig. 16A–B and E–F) and related iron-rich rocks (Ruhlin and Owen, 1986; Derry and Jacobsen, 1990; Sholkovits et al., 1994; Dubinin, 2004). Thus, the ferruginous sandstones and the Lower Mn-1 layer are clastic–chemical diagenetic rocks, in which evidence of biogenic mediation was erased by the rapid homogeneous oxidation of Fe and Mn and diagenesis. These rocks were deposited on the basin floor along the inundation front between the marine and continental phreatic waters and extended laterally as the inundation advanced into the basin. The Upper Mn-1 manganese layer is clastic–chemical, with clastic illite and kaolinite forming from the oxidation and sedimentation of original Mn (II) in the water after the filling of the pore spaces in the Urucum Formation's sediments, which were mixed with clay minerals and quartz grains from turbidity currents.

The breaking and displacement of basement blocks generated conduits, which allowed the rise of heated aqueous fluids and beginning hydrothermalism (Fig. 18B–E) on the basin floor, as indicated by the hydrothermal alteration of the granite near the faults (Fig. 1) and ferruginous chert infilling fractures in the granite and sedimentary rocks in the Urucum Formation. The vents emitted silica-, iron- and manganese-rich fluids, causing the saturation of the water, while avalanches and fragment flows did not cease, allowing the displacement of basement-rock blocks to the bottom of the basin, turbidite flows and the mixing of the water with clay minerals from the basement (Fig. 18E). This environment favored the clastic-chemical sedimentation of laminated, clayed, and manganese- and iron-rich sediments (Fig. 6A–C), forming the Mn-1 Unit (Figs. 2 and 5), which covers the basin floor (Figs. 3 and 18C–D) throughout the Urucum region.

During the formation of Mn-1, rapid and strong homogeneous oxidation in seawater prevailed over other processes that could destabilize and precipitate substances. Evidence of microbe mediation during Mn (and Fe?) sedimentation was probably hindered by the strong iron, silica, and manganese enrichment in the seawater from the hydrothermalism, the increase in temperature, and the rapid oxidation in the water. Therefore, the high concentrations and the distributions of Mn, Fe, P, Co, Ni, and Cu in Mn-1 and their host IFs were a consequence of the simultaneous action of three processes. (a) The death and sedimentation of large quantities of microorganisms, which were selectively enriched with P, Co, Ni and Cu, occurred because of changes in the environment, especially water saturation and heating from hydrothermal activity. The distribution of the bio-essential elements was likely a consequence of different microorganisms carrying Co and Cu when the Mn-rich layer was deposited and P and Ni when the host IFs were deposited, adding to the rapid annihilation of these micro-organisms. (b) Clastic apatite and clay minerals were released by the weathering and erosion of basement rocks outside the basin. (c) Water saturation with hydrothermal Mn, Fe, and SiO_2 occurred. These processes were different from those that formed Mn-2 and Mn-3 because these actions did not induce the formation of kremydilites and caused strong enrichment in Co (+ Cu) in the Mn-1 layer of clayey Mn ore and P + Ni in the host massive iron formations (Fig. 15).

The chemical precipitation of silica, iron, and manganese in the basin depocenter formed the Santa Cruz Formation, while the microbial-mediated precipitation of carbonates formed limestone at the basin margins, including peritidal stromatolites, which are currently located at the base of the Bocaina Formation (Figs. 1and 18B–E). These rocks filled a basin that was open to the west and comprised local estuarine environments. This configuration remained stable long enough for the basement and limestone with stromatolite blocks to be displaced from the littoral regions, transported to the floor of the graben, and incorporated into marine sands and conglomerates that overlie the pre-existing continental sediments (Figs. 3B, 4A, and 18B). Subsequently, some *Corumbella werneri* died and settled amid the IFs in the Santa Cruz Formation during the deposition of the Tamengo Formation (Fig. 18F).

The sudden homogeneous oxidation and consequent sedimentation of Fe and Mn, which occurred when seawater contacted the fluvial and lacustrine oxidizing sediments from the Urucum Formation, would have

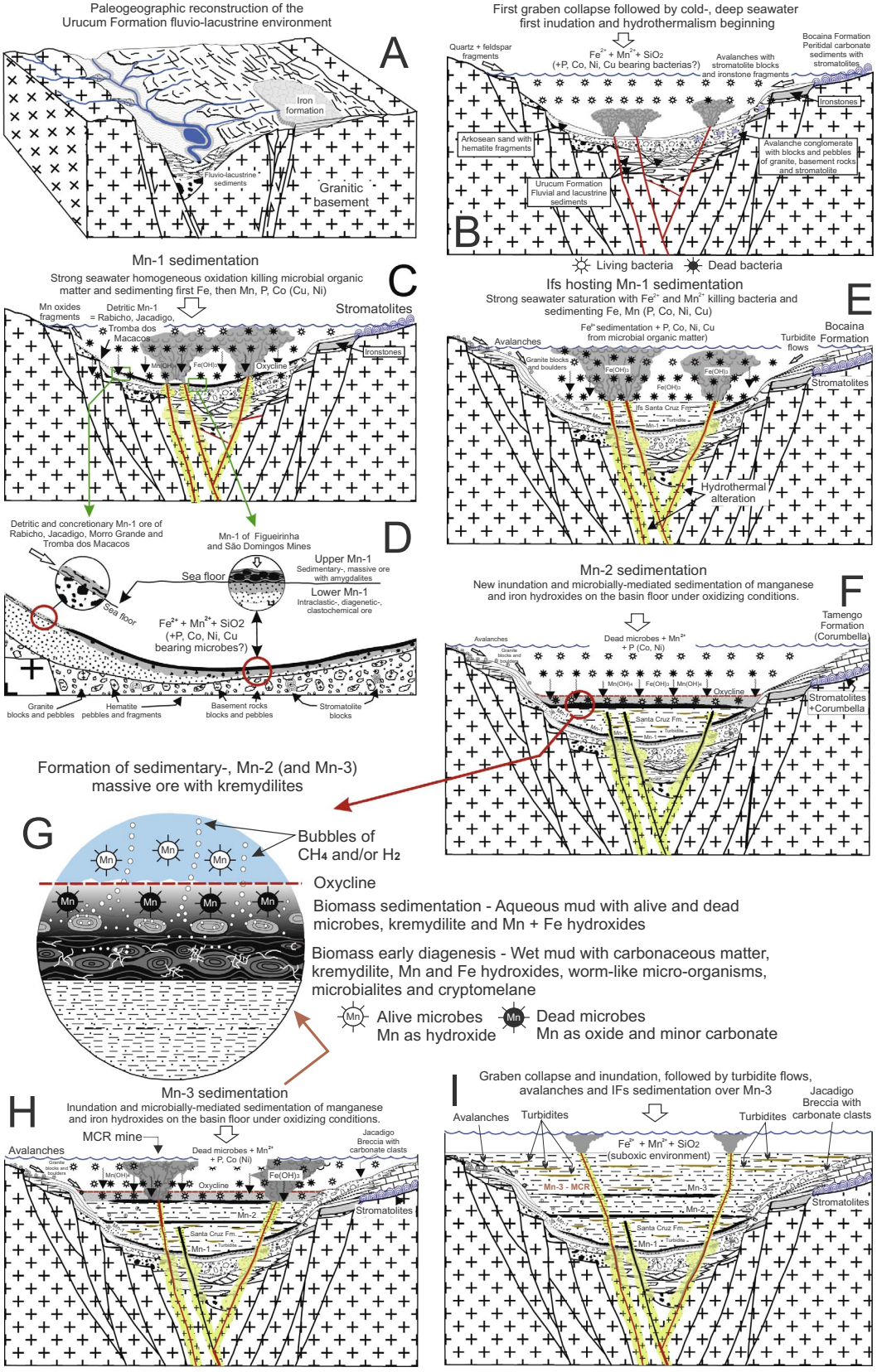

Fig. 18. Cartoons showing the sequence of geological events that generated the manganese ore layers Mn-1, Mn-2, and Mn-3, and their host IFs. The figure annotations provide details about the processes and depositional environments.

been the only process that could precipitate the volume of manganese oxides that are contained in the Mn-1 layer across the basin floor (Fig. 3A and 18C–D). The Upper Mn-1 layers in the Figueirinha and São Domingos mines, which contain amygdalites, were probably deposited in the basin depocenter (Fig. 1), where amygdalites formed from hydrodynamic flux. Differential compaction and diagenesis generated wavy contacts and concentrated the sedimentary manganese oxides and, probably, minor Mn-carbonates. Simultaneously, thin layers of detrital manganese and iron oxides that were derived from the erosion of iron manganiferous units that predated the graben opening were deposited on the basin slopes over the continental sediments (Urucum Fm.), which were cemented by iron hydroxides. The detrital ore that was cemented by Mn oxides (currently diagenetic cryptomelane) constitutes detritic Mn-1 layers in the Laginha, Rabicho, Morro Grande, and Jacadigo mines (Figs. 5, 6G–K, and 18C–D). The REE pattern of this ore type, which is distinct from those of the other Mn ores in the Urucum region, was likely inherited from the detritic source of manganese oxides (Fig. 13G–H). The discrete enrichment in HREEs in the Mn-1 ores other than Rabicho may have been the result of capture by Mn $(OH)_4$ flakes and clay minerals. Therefore, the Upper Mn-1 ores must have been silica-rich argillic muds that contained $Mn(OH)_4$, were slightly more enriched in HREEs than LREEs, and contained little Ce. These silica-rich mud-cemented clasts generated a sedimentary clastic–chemical Mn ore with negative Ce anomalies and discrete enrichment in HREEs (Fig. 16A–B).

Braunite can occur in banded sedimentary ores, as in the Neyriz ophiolite (Fars Province, southwestern Iran), where this rock was probably a biogeochemically mediated early diagenetic product (Rajabzadeh et al., 2017), and in the Hotazel Formation, where this rock was a braunite mud (Gutzmer and Beukes, 1996). In the Urucum region, braunite only occurs within the Mn-1 layer in the Figueirinha Mine, and the grain geometry, which is angular and dimensionally variant, and the random distribution indicate that these rocks are clasts. This rock may have been derived from the erosion of the basement rocks and was transported from within the Urucum graben, probably as a braunite sandy mud. During diagenesis, the detrital braunite formed intergrowths with cryptomelane and/or hollandite.

Concretionary ores (Figs. 5 and 6E–F) formed after the Urucum graben was flooded, as water began to infiltrate the conglomerates and continental sandstones on the basin floor, and manganese oxides were dissolved and re-precipitated in fractures and open spaces. Following basin inversion and continuing to the present, meteoric water continued to dissolve the manganese oxides, transport them downward and laterally, and precipitate them as oxides and hydroxides that infilled fractures and cemented the matrix of the sandstones and conglomerates, as can be observed in the Rabicho and Jacadigo mine galleries (Fig. 6E–F).

6.4. Genesis of Mn-2, Mn-3 and kremydilites

At the end of a flood cycle before Mn-2's sedimentation, microbially mediated oxidation of Fe(II) to Fe (III) and the formation of ferrihydrites occurred, which adsorbed colloidal silica and were deposited simultaneously with the arrival of turbiditic fluxes, forming ferrous-siliceous mud. The onset of diagenesis began the transformation of ferrihydrites to more stable Fe-oxides (hematite, goethite, etc.). Silica was exsolved from ferrihydrites. At the end of diagenesis, these sediments became IF layers of Fe-rich siltstones, hematite chert and massive layers of hematite with chert lenses (Fig. 8C–D and 13D), on which the Mn-2 layer of massive manganese settled (Fig. 7B, D, F; 18F). Later, Mn-3 also formed after the sedimentation of ferro-siliceous muds under identical conditions to Mn-2 (Figs. 7A, C, E; 18H).

Layers Mn-2 and Mn-3 formed in "offshore" (=greater depth) environments during periods of tectonic quiescence (Fig. 18F), when fine, clastic quartz fragments and chemical sedimentation ceased at the end of a flood cycle. During the formation of Mn-2 and Mn-3 (Fig. 18F–H), the basin was flooded with microbe-, manganese-, iron-, and CO_2-rich cold and reduced seawater. Within the shallow Urucum basin, water was heated and became oxidizing, as indicated by the presence of diagenetic Mn carbonate in the ores (Fig. 10.1A–D) and the negative Ce anomalies (Fig. 16C–F) in manganese- and iron-rich rocks (Ruhlin and Owen, 1986; Derry and Jacobsen, 1990; Sholkovits et al., 1994; Dubinin, 2004). Biogenically mediated oxidation of Mn(II) to Mn (IV) occurred, followed by the precipitation of manganohydrites under oxidizing conditions. Some chemically oxidized iron and very little silica were likely deposited together (Fig. 18F–H). The sedimentation of Mn-2 was interrupted because of an increase in tectonic activity and, consequently, iron-siliceous hydrothermalism, which covered the basin floor with arkosic mud and conglomerates from turbidite flows and avalanches. These events disturbed the water in the Urucum basin, changing the oxygen supply, which became suboxic, and allowing the sedimentation of ferruginous arkosic muds and conglomerates with a ferruginous arkosic matrix (Fig. 7B, D and F). The same types of events with identical products occurred during Mn-3's sedimentation (Figs. 7A, C and E, and 18H–I). This record suggests that the Mn-rich water originated outside the basin and entered the Urucum Basin in two phases (represented by layers Mn-2 and Mn-3) when tectonism and the emission of iron and silica from vents on the basin floor ceased.

The positive Ce anomaly in layer Mn-3, which was observed only at the MCR Mine, could be explained by the local presence of a vent (Fig. 18H), which emitted oxidized iron- and manganese-rich high-temperature fluids, whose hydroxides captured and deposited Ce^{4+} and Eu^{4+} (Ruhlin and Owen, 1986; Owen and Olivarez, 1988; Derry and Jacobsen, 1990; Sholkovits et al., 1994; German et al., 1995; Dubinin, 2004; Chen et al., 2006). This hypothesis explains why layer Mn-3 in the VALE and MCR mines, which was deposited simultaneously in these two locations, yielded distinct Ce anomalies.

The floodwater contained high concentrations of Mn(II) and microorganisms, and life flourished within the basin, allowing the sedimentation of biomass (=free carbon; Figs. 9–12 and 18G) and precipitation of manganese and iron hydroxides. The right-hand, dark gray part of a gas bubble shown in Fig. 11I–J, and the kremydilite micropore-filling materials (Figs. 11C–F, I–K, and 12E–D) likely preserved the original composition of the sediment that formed layers Mn-2 and Mn-3. The original biomass contained a significant amount of carbonaceous matter (Figs. 9D, 10.1C–D, 10.3D, 10.4A–C, 10.5C–E, 10.6A, 11C–J, and 12C–K), which is likely consisted of P- and Co-rich dead chemolithotrophic organism residues, and a low silica content (related to ferrihydrite sedimentation) (Figs. 15 and 18F–H). This reason, together with geometry, internal zonality, the presence of nodular micro-structures, and carbonate microbialites, explains why the kremydilites were interpreted as bacterial colonies that lived in the aqueous mud, in locations that were affected by solar and/or ultraviolet (UV) radiation (Fig. 18G). The chemolithotrophic organisms that formed the kremydilites lived in Neoproterozoic anoxic environments (Cloud, 1973; Drever, 1974; Schopf, 1974; Konhauser et al., 2005, 2007) and used Fe (II) and Mn(II) in their biosynthesis by fixing CO_2, removing oxygen and producing ATP to conserve energy. Thus, the environment was reducing, containing high CO_2 concentrations and likely located near or below the oxycline. The presence of kremydilites confirms that their higher concentrations in layers Mn-2 and Mn-3 are related to biologic activity, although phosphate and cobalt have strong affinities to hydroxides.

Microbes can also oxidize Fe(II) to Fe(III) and Mn(II) to Mn(IV), even under anoxic conditions, converting Fe(II) to $Fe(OH)_3$ (Konhauser et al., 2005) and Mn(II) to $Mn(OH)_4$. Fe(II) and Mn(II) serve as the electron donors for these organisms, which convert CO_2 into biomass by using solar energy (Kappler et al., 2005). According to Konhauser et al. (2005), the general reaction between Fe(II) and CO_2 to generate iron hydroxide and carbonaceous matter (biomass), which is represented by CH_2O, is

$$4Fe^{2+} + CO_2 + 11H_2O \rightarrow \langle CH_2O\rangle + 4Fe(OH)_3 + 8H^+ \quad (1)$$

By analogy,

$$3Mn^{2+} + CO_2 + 11H_2O \rightarrow \langle CH_2O\rangle + 3Mn(OH)_4 + 8H^+ \quad (2)$$

By analogy with Posth et al. (2013), water, methane (CH_4), and hydrogen (H_2) gas could be released by dehydration and coupled redox reactions, including biomass oxidation and Mn^{4+} reduction, according to the following general reaction:

$$Mn(OH)_4 + \langle CH_2O\rangle \rightarrow Mn^{4+}O_2, Mn^{2+}O, Mn^{2+}Mn_2^{4+}O_5, Mn_2^{2+}CO_3, C, H_2O, CH_4, H_2 \quad (3)$$

This series of reactions produced the internodular and intergranular bubbles of methane and hydrogen that are found inside (Fig. 11A) and near (Fig. 12A) the kremydilites, facilitating the preservation of carbonaceous matter inside the bubbles. When these bubbles left the reductive mud, moving toward the basin floor surface and passing the oxycline, they entered an oxidizing environment, which generated a massive wrap of manganese oxide (Fig. 11C, G, and I; and 11B, I, and J) from superficial tension because of the oxygen concentration around the bubble.

The presence of internodular gas bubbles inside and outside the kremydilites indicates that these rocks were highly porous and permeable structures, within which gas bubbles could form and migrate out (Fig. 18G). The bubbles that are now observed in the rocks did not reach the basin floor and were preserved during diagenesis. Moving outward from the kremydilite core, each subsequent zone corresponds to a period of Mn-oxide micronodule nucleation, carbonate precipitation, and kremydilite growth. This zonation was probably caused by cyclic changes in the CO_2 concentration in the submarine mud because of discontinuous layer burial and the oscillation of the oxycline position between the top and inside of the mud layer (Fig. 10A and 10.1A–D), similar to the process that generates stromatolites. The formation of micronodules and kremydilites probably ceased rapidly because of disappearance of microorganisms when tectonic activity recommenced and the vents were reactivated. These microorganisms were likely poisoned by the high concentrations of Fe and silica in the hydrothermal fluids that were emitted from the vents.

Incubated manganese and iron reacted with formaldehyde and likely produced the micro-clusters of manganese, iron and calcium–-magnesium carbonate crystals (Fig. 10.1A–D). Many bacteria can couple Ca–Mn reduction with organic matter mineralization to produce energy for growth (Myers and Nealson, 1988; Lovley, 1991; Nealson and Myers, 1992; Nealson and Saffarini, 1994; Meister et al., 2009). The driving force for this Mn–Ca carbonate precipitation is a rise in alkalinity, and the metabolic reactions that are known to be involved in this process are as follows:

Dissimilatory Mn reduction:

$$2MnO_2 + \langle CH_2O\rangle + 3CO_2 + H_2O \rightarrow 2Mn^{2+} + 4HXO_3^- \quad (4)$$

Anoxic precipitation of Mn–Ca carbonates:

$$xMn^{2+} + (1-x)Ca^{2-} + 2HCO_3^- \rightarrow (Mn_xCa_{1-x})CO_3 + CO_2 + H_2O \quad (5)$$

Anoxic precipitation of Mn–Fe–Mg–Ca carbonates:

$$4(Mn,Fe,Mg,Ca)(OH)_3 + \langle CH_2O\rangle \rightarrow (Mn,Fe,Mg,Ca)CO_3 + 3(Fe,Mg,Ca)^{2-} + 6OH^- + 4H_2O \quad (6)$$

The wormlike objects (Fig. 10.4B–C and 10.5B–D) were likely microorganisms that inhabited the carbonaceous mud at the beginning of diagenesis, when sediments were wet and soft but consistent enough through which worms could dig holes (Fig. 10.3A–B). The carbonate mesh structure (Fig. 10.3B–D), prismatic crystallites (Fig. 10.5E), and micrometric nodules (Figs. 8H–I and 10.6A) were microbialites or organominerals (Dupraz et al., 2009), and the cylindrical holes (Fig. 10.3A–B) are likely tubes that were formed by the wormlike microorganisms as they moved within the mud and kremydilites. The absence of nodules and iron kremydilites in the jaspilites, similar to the Mn ore layers, indicates that the formation of micronodules and kremydilites was a unique process that only occurred in the Mn-ore sediments. Therefore, the millimeter-scale manganese micronodules in layers Mn-2 and Mn-3 (Figs. 8E–F, 9, and 10) did not nucleate in seawater but instead within the biomass from hydroxides contained therein. Thus, the microorganisms consumed iron and manganese hydroxides, separated the manganese and iron, and excreted solely manganese hydroxides, generating cryptomelane microbialites. The microbialites subsequently coalesced, forming pure, massive cryptomelane micronodules (Fig. 7E–F and 8A–G) that are devoid of hematite (Fig. 9D and H), resulting in layers of massive manganese oxides ± manganese carbonates (Fig. 10A and 10.1A). The microorganisms then converted manganese and iron hydroxides into cryptomelane and hematite, respectively, although we cannot estimate the importance of this contribution. Seemingly, the manganese micronodule nucleation process occurred simultaneously with the crystallization of manganese carbonate (Fig. 10.1A–D, 11F–J, and 12J), hausmannite, bixbyite, and subordinate amounts of Al and Mn phosphate (eosphorite and crandallite), with the phosphorus being derived from organic residue in biomass. The concentration of oxides may have increased during late diagenesis if the mud on the basin floor gradually became oxidized because of the backflow of water from the basin and consequent lowering of the oxycline to a position below the surface of the mud layer. During the late stages of diagenesis, the majority of the original organic matter was likely destroyed and replaced by cryptomelane, as seen in the left-hand, light-gray component of the bubble in Fig. 11I. With the onset of diagenesis, the cryptomelane began to recrystallize as hollandite (Fig. 14B–C). Following tectonic inversion and the exhumation of the layers that contained manganese oxides, new hollandite formed via cryptomelane weathering.

6.5. Iron-rich rocks hosting the manganese ore layers

The REE of the seawater from which the iron-rich host rocks were deposited was seemingly influenced by low-temperature hydrothermal exhalations from vents that cross-cut the granite basement. Solutions of HREEs in seawater are more stable than those of LREEs, and the solubility of HREEs increases with temperature (Ruhlin and Owen, 1986). These characteristics explain why HREEs tended to remain in solution and the sediments became depleted in HREEs, as in the ferruginous arkosic rocks (Fig. 16H). The slight HREE enrichment in the REE patterns of layers Mn-2 and Mn-3 and the IFs was also likely to be a consequence of decreasing basin water temperature because of an inflow of large volumes of colder water from the open sea.

Klein and Ladeira (2004) and Angerer et al. (2016) studied the IFs at the Urucum and Santa Cruz deposits and observed similar REE distribution patterns to those of the iron-rich rocks that host the manganese ore layers. The REE fractionation pattern and REE abundance in “hematite chert” and “hematite mud” from the Santa Cruz deposit (REE-3, Angerer et al., 2016) are very similar to those of the iron-rich rocks that host Mn-2 and Mn-3 (Fig. 16F) and the ferruginous and/or manganiferous arkosic rocks from the Urucum region (Fig. 16H). These rocks are also very similar to “hematitic muds and silts” in the Rapitan IF (Halverson et al., 2011). The features of the REE patterns in all these rocks are bulged, flat, and slightly convex, with very discrete negative Ce anomalies and slight MREE enrichment. The REE abundances are relatively consistent, with REE_N between 0.1 and 1.0, and do not show positive Eu anomalies. The “chemical hematite muds” of Angerer et al. (2016) are similar to the grain-ironstones from these same mines (Fig. 3). Thus, the carbonate-poor IFs that were studied by Klein and Ladeira (2004) and Angerer et al. (2016) are the same rocks that host the manganese ore layers Mn-2 and Mn-3.

As described above, cloudy water from turbidite flows with sand, silt and clay added to the saturation of hydrothermal silica and iron,

rendered the environment suboxic, and must have caused the disappearance or at least a strong reduction in the population of microorganisms. This process generated IFs with high concentrations of phosphate and cobalt in Mn-1 (Fig. 15) from dead microbes (Fig. 18E). The iron and silica in these units were probably derived from fluids that were emitted by hydrothermal vents on the floor of the Urucum Basin, which subsequently mixed with seawater from cold upwelling currents, as indicated by the Y/Ho ratios (Fig. 14D).

The IFs that host Mn-2 and Mn-3 formed from the simultaneous precipitation of mainly hydrothermal $Fe(OH)_3$ and fine clasts (essentially quartz), which were mixed with a small amount of clastic illite and kaolinite from turbidites. These units are interspersed with channels that are filled by clastic rocks with ferruginous matrix from turbidity currents and avalanches, which occurred simultaneously with the hydrothermal and minor microbially mediated ferrihydrite sedimentation (Fig. 7). The grain sizes of the clastic–chemical ironstones vary from clayey to coarse-sandstone turbidites and chaotic conglomerates, containing small to enormous rounded and/or broken, irregularly shaped granite blocks (lonestones) within an arkosic ferruginous matrix, which indicates submarine-avalanche deposition (Fig. 16E–H) simultaneously with the precipitation of $Fe(OH)_3$. The tectonic activity that induced the formation of these clastic rocks ceased during the sedimentation of the manganese layers, as indicated by the absence of clasts in the ores. The succession of layers suggests that periods of tectonic stability, during which Mn-2 and Mn-3 were deposited under oxidizing conditions, existed between periods of instability, when ferruginous turbidites and avalanches deposited sandstones and conglomerates with ferruginous matrix in a suboxic environment (Fig. 2).

The “podded hematite chert” and “dolomite–chert hematite BIF” (REE-1, Fig. 17A), as described by Angerer et al. (2016), are structurally similar to the “hematite chert with Fe and Mn dolomite” that was described by Klein and Ladeira (2004) and the massive peloidal jaspilite and banded BIFs in the VALE and MCR mines (Figs. 3 and 13B–C), which are located in the upper half of the Urucum and Santa Cruz plateaus. All these carbonate rock types are located stratigraphically above the Mn-3 ore layer and were never observed hosting the manganese ore layers. The REE distribution patterns (Fig. 17A–B) in these rocks are different from those of the other IFs from the Urucum region. Their REE distribution patterns show more pronounced negative Ce anomalies and are continuously enriched in REEs from Ce to Lu, similar to the seawater, although their REE concentrations are approximately 10^6 times higher (Fig. 17A and B). This difference cannot be explained by detritus because no covariance exists in the Y/Ho ratios with Al_2O_3 in the Mn ores (Fig. 14D), and the contribution from detrital sources in the Mn ore layers and Fe-rich rocks is considered insignificant. However, the magnitudes of the negative Ce anomalies in the sediment also depend on the degree to which the water is oxidizing, the distance between the vents, the deposition location, and the magnitude of dissolution by Mn–Fe-hydroxides (Bau et al., 1997). Most REEs that originate from seawater and vents will be deposited near the vents by the settling of hydroxide particles (Ruhlin and Owen, 1986; Owen and Olivarez, 1988; Derry and Jacobsen, 1990; Sholkovits et al., 1994; German et al., 1995; Dubinin, 2004; Chen et al., 2006). If the vents are located in reducing water and this water is displaced by ocean currents, the remaining Ce in solution can oxidize and precipitate in locations far from the vents and next to the oxycline depth, thereby generating sediments with small negative anomalies because of the low amount of available Ce. The negative $\delta^{13}C$ values that were observed by Angerer et al. (2016) in carbonate BIFs from the Santa Cruz deposit, which were interpreted to be of biotic origin, may have been related to a hydrothermal origin for these rocks (e.g., Large and Both, 1980; Kowalick et al., 1981; Eastoe and Nelson, 1988; Zaw and Large 1992; MacLean and Hoy, 1991; Biondi et al., 2011) or the presence of carbonaceous matter (e.g., Hoefs and Frey, 1976; Hedges and Mann, 1979; Dean et al., 1986; Konhauser et al., 2005; Kump et al., 2011; Polgári et al., 2012a,b). Therefore, the explanation for the differences between the REE patterns in these rocks and those of the IFs that host the manganese ore layers may be related to the different origins of the starting seawater solutions from which the rocks were deposited and microbially mediated selective-enrichment mechanisms.

6.6. Comparison with deposits similar to Urucum

The Úrkút (Hungary) black shale-hosted Mn carbonate deposits and cherty, Fe-rich Mn oxide mineralized rocks are Toarcian in age (183–174 Ma). The entire deposit contains 32 Mt of Mn carbonate rocks, averaging from 13% (Mn carbonate “ore”) to 27% (gray Mn carbonate “ore”) Mn, and 26 Gt of Fe, averaging from 7.4% (black shale) to 21.7% (cherty Fe–Mn oxide “ore”) Fe (Polgári et al., 2012a,b).

In Úrkút, spherules (similar to the nodules in Mn-2 and Mn-3), oval, tubular, and filamentous morphologies were observed and interpreted to be cellular materials that are enriched in bio-essential elements. These spherules show an inner texture of yet smaller spherules, and Mn oxides fill the pore spaces between these spherules, forming similar structures to those in Fig. 9F–H. These spherules and surrounding areas consist of goethite, hollandite, pyrolusite, cryptomelane, todorokite, manganite, quartz, and carbonaceous materials. Similar to Urucum, Polgári et al., 2012a,b considered that an exhalative hydrothermal source of metals may have contributed to the formation of the deposit at Úrkút via an Fe–Mn oxide chimney system along fractures, providing metals from deep-seated sources. Small structures, which were approximately 10 mm in diameter and identical to columnar stromatolites in carbonate, were described as microbial stromatolite-like structures of Mn oxide. Such structures were considered by Polgári et al. (2012b) to be one of the best pieces of evidence for the role of microorganisms in the genesis of the Úrkút deposit. These biomats formed at the sediment-water interface under dysoxic and neutral pH conditions by enzymatic Fe(II) oxidizing processes, which may have developed on a daily to weekly growth cycle (Polgári et al., 2012a). Evidence for microbial activity in different ore types and accompanying rocks in the Úrkút Mn deposit also includes (a) brown chert with micro-chimneys that contain mineralized bacteria in the Úrkút manganese deposit, (b) mineralized filamentous bacteria in the main Mn carbonate ore bed, and (c) mineralized bacterial filaments that consist of cryptomelane.

According to Polgári et al. (2012b), these features and the $\delta^{13}C$ values, which range between +3‰ and −16‰ in the Mn carbonates, support microbially mediated reactions, and more specifically, microbial metabolic processes. Geothermally produced hydrothermal fluids were the likely source of the metals in the Úrkút deposits. These fluids formed authigenic Mn minerals under suboxic diagenetic conditions that were related to a large Fe–Mn oxide chimney system with fluid-flow micro-channels. Stromatolite-like, filamentous and coccoid microstructures that consist of Fe-Mn-oxides (ferrihydrite, goethite, manganite, pyrolusite, hollandite, birnessite, hausmannite) and silica occur in the micritic marlstone host rock among common calcite bio-debris (microfossils and Echinozoa fragments) and rare detrital clasts (quartz, feldspar). Metal-bearing fluids infiltered the unconsolidated micritic limemarl. Fe-oxide enrichment likely occurred through iron-oxidizing microbes under suboxic, neutrophilic conditions, while Mn oxide likely formed by active surface catalysis. At the sediment/water interface, FeMn-oxide stromatolite mounds (chimneys) formed in rift zones from the discharge of fluids with elevated temperature (Molnár et al., 2017). The Fe–Mn oxides in these chimneys contain significant amounts of amorphous carbon of variable composition and distribution, which is consistent with a microbial origin. During the development of the Mn oxide ore, the first product of microbial Mn(II) oxidation was probably an amorphous bio-oxide that was similar to δ-MnO_2. The high Mg content of the black shale-hosted Mn carbonate deposits was first considered to have resulted from a magmatic, volcanic source, an idea that was later abandoned in favor of a microbial origin (Polgári et al., 2012a,b).

Úrkút resembles Urucum in the following aspects: (a) bacterial

mediation that concentrated manganese in rocks; (b) submarine hydrothermal exhalations as the source of Mn and Fe; (c) the presence of carbonaceous matter in mineralized rocks; (d) the high contents of organometals; (e) the presence of biotic structures, termed spherules, equivalent to the micronodules in the Urucum deposit; and (f) the presence of stromatolite-like structures. All the other main characteristics of Úrkút are distinct from Urucum: (a) Úrkút formed at 183–174 Ma; the much younger age of the Úrkút rocks facilitated the preservation of the original features, including mineralized filamentous microbes in the Mn carbonate ore bed; (b) no BIFs and IFs occur at Úrkút, and massive cherty Fe-Mn-oxide ore occurs only locally (at Csárdahegy) as primary ore below the main ore zone (Molnár et al. 2017), which consists of massive carbonate rocks with Mn and Fe carbonates, metalliferous black shales, and clays with Fe and Mn; (c) at Úrkút, the first product of microbial Mn(II) oxidation was an amorphous bio-oxide similar to δ-MnO_2; (d) the main ore of the Úrkút deposit is an early diagenetic rhodochrosite, while early diagenetic rhodochrosite is very rare in Urucum; a two-step microbially mediated ore-formation process (oxic, neutrophylic autotrophic Mn-oxidizing metabolism followed by suboxic-anoxic heterotrophic Mn-reduction; Polgári et al., 2012a) occurred in Úrkút, but the main mass of the Mn ore in Urucum remained oxic; only cycle 1 occurred and the rock did not transform to rhodochrosite despite the considerable amount of organic matter; thus, the heterotrophic Mn-reducing bacteria from cycle 2 did not become dominant; one possible interpretation can be that Urucum remained more oxic than Úrkút via diagenesis, which is supported by the host IFs; and (e) at Úrkút, the stability of Mn oxides increased as the pH and Mn (II) concentration increased; at Urucum, the concentration of oxides was initiated by bacterially mediated hydroxide precipitation, continued from the action of wormlike microorganisms during early diagenesis, and was likely completed as mud on the basin floor gradually became oxidized.

The Kalahari manganese field in South Africa contains an estimated approximately 8 Bt of Mn resources (Cairncross and Beukes, 2013), with Mn contents between 20% and 48%. This field occurs within the Hotazel Formation in the uppermost Archean to Paleoproterozoic (2.65–2.05 Ga) Transvaal Supergroup and comprises three laminated Mn-ore units that are interbedded with iron formations (Tsikos et al., 2003; Cairncross and Beukes, 2013). The lowermost of the three manganiferous units is the most important, containing 44–48% Mn.

Gutzmer and Beukes (1996) considered that the sedimentation and early diagenesis of the Hotazel Formation, which consists of interbedded iron formations and braunite lutite, was followed by low-grade metamorphism and associated stratabound metasomatism. The braunite lutite, which has a sedimentary origin and comprises 97% of the total ore reserve, consists of braunite, hematite, and kutnohorite, with abundant early diagenetic kutnohorite and manganoan calcite that form laminae and diagenetic Mn–calcite ovoids. Fluid flow during late diagenesis or lower greenschist-facies metamorphism led to the stratabound metasomatic oxidation of Mn-bearing carbonates to hausmannite and Mn-poor calcite.

Three structurally controlled hydrothermal alteration events, which are referred to as Wessels, Mamatwan, and Smartt, followed this metamorphism. The Wessels alteration event was the oldest, and virtually all the high-grade ore (> 42% Mn) formed during this event through the alteration of carbonate-rich low-grade Mamatwan-type ore (braunite lutite). Normal faults and fractures apparently served as conduits for hydrothermal fluids where they penetrated laterally into the manganese-ore beds, replacing manganese ore with hematite (Gutzmer and Beukes, 1995). Cryptomelane and pyrolusite are the predominant products of surficial weathering (Tsikos et al., 2003). All these conclusions based on thermo-dynamic studies (Miyano and Beukes, 1987) indicate that the primary paragenesis of the rocks from the Hotazel Formation precipitated from fluids with temperatures between 300°C and 400°C (Miyano and Beukes, 1987; Gutzmer and Beukes, 1995; Beukes et al., 1995).

In the southern Kalahari manganese field, the iron formations contain quartz, magnetite, and carbonate (calcite and ankerite) as the chief mineral constituents and exhibit comparable mineralogy and bulk chemical and isotopic signatures to other Paleoproterozoic iron formations around the world (Tsikos and Moore, 1997). Values of $\delta^{13}C = -18$ to -4‰ vs. PDB and $\delta^{18}O = 12$–20‰ vs. SMOW for the carbonate in the iron formations indicate diagenetic processes that involved the oxidation of organic carbon and Fe^{3+} reduction of sedimentary precursors. Values of $\delta^{13}C = -12$ to -8‰ and $\delta^{18}O = 14$–22‰ for the interbedded manganiferous units are interpreted to reflect similar processes, with Mn^{4+} acting as the sole electron acceptor (Tsikos et al., 2003).

The deposition of the 2.2–2.3-Ga Hotazel Formation was initially explained by Beukes (1983) as transgressive–regressive events relative to the deposition site. Beukes (1983) suggested a distant submarine volcanic source for the iron, manganese, and silica. The manganese formation, which was probably originally a mixed precipitate of carbonates and oxides, represented the more distal sedimentary facies compared to the more proximal iron formations. The braunite, hematite, and matrix carbonates are thought to have formed during very early diagenesis, soon followed by the kutnohorite and Mn–calcite in the ovoids and laminae. These ideas were reconsidered, and Beukes and Gutzmer (2008) stated that chemolithoautotrophic iron-oxidizing bacteria may have played an important role in the precipitation of ferric oxyhydroxides and acted as a source of primary organic matter in deep-water environments under micro-aerobic conditions. Within the basin fill, even shallow-shelf embayments were invaded by circulating hydrothermal plume water, from which ferric oxyhydroxides could be precipitated in oxygenated environments with high primary organic-carbon productivity and, thus, iron reduction to form hematite-poor siderite- and magnetite-rich clastic-textured iron formations. Although no explicit reference has been made to the biogenic origin of the manganese layers that are interbedded with the BIFs, these authors likely considered that this origin for the manganese is also valid.

The Kalahari manganese field comprises much larger and older (2.2–2.3 Ga) manganese deposits than Urucum. The origin of this metal, the distant submarine volcanic source of iron, manganese, and silica, and the sedimentation process that was proposed by Beukes (1983), which consisted of transgressive–regressive events relative to the site of deposition site, are generally similar to those for Urucum.

The major differences are as follows: (a) the original sediment was a carbonate-braunite lutite that consisted of braunite, hematite, and kutnohorite, with abundant early diagenetic kutnohorite and manganoan calcite forming laminae and diagenetic Mn–calcite ovoids; (b) no similar structures to kremydilites or amygdalites were described in the rocks from the Hotazel Formation; and (c) three structurally controlled hydrothermal alteration events transformed the original braunite to todorokite and manganomelane and destroyed carbonate. Cryptomelane and pyrolusite are the predominant products of surficial weathering.

7. Conclusions

1. When the Urucum basin was filled with sediments, chemical, microbial, and clastic sedimentation occurred, sometimes together and other times with one predominating over the others.
2. The matrix of the arkosic rocks stratigraphically below layer Mn-1 consists of hematite and jasper. Therefore, contrary to what was initially believed (Park et al., 1951), at least two periods of iron precipitation predated layer Mn-1: (1) the formation of hematite rock outside the Urucum Basin region, thereby providing the source of the hematite fragments in the arkosic conglomerates and arkoses; and (2) the precipitation of the hematite and chert, forming the ferruginous arkose matrix stratigraphically below the Lower Mn-1 layer.
3. Many seawater influx episodes flooded the Urucum Basin: (a) when

the Mn-1 layer in the Figueirinha and São Domingos mines and the host IFs were deposited (Fig. 18B–E); (b) when layer Mn-2 precipitated (Fig. 18F); (c) when layer Mn-3 precipitated (Fig. 18H); and (d) possibly when the IFs adjacent to and above layer Mn-3 were deposited (Fig. 18I). All these flood events probably generated environments with water that was rich in Mn(II) and CO_2. The negative Ce anomalies and convex MREE patterns of the IFs and arkosic sediments indicate that these sediments inherited the REE signature of the basement rocks. Layers Mn-2 and Mn-3 do not show this pattern, so the basin was flooded with microorganisms and Mn(II)-rich, deep seawater that originated from outside the basin and that the hydrothermal flow within the basin had ceased during their sedimentation. Simultaneously, biotic-mediated limestone and carbonate rocks precipitated in the shallow littoral zones around the basin, forming the Bocaina Formation with intertidal stromatolite colonies and, later, the Tamengo Formation.

4. Several tectonic events caused the deepening and opening of the Urucum graben. The inundation that first flooded the Urucum Basin occurred when the valley was deep and filled with fluvial and lacustrine sediments. The valley was flooded gradually but completely, creating a basin that comprised a depocenter region, where vents opened and hydrothermalism began and shallow, wide margins were formed. Along the inundation front on the graben floor, seawater that contained Fe(II), Mn(II), CO_2, SiO_2, and more than one phosphorous-, Co^{2+}-, Ni^{2+}-, and Cu^{2+}-bearing microbial type infiltrated the fluvial sediments of the Urucum, filling the pores of the fluvial sediments and cementing them with iron hydroxides that were enriched in P, Co, Ni, and Cu. The homogeneous oxidation was rapid and strong, hiding the evidence of biogenic mediation and not allowing the growth of kremydilites. This water, which was depleted in iron and enriched in manganese, seeped into the pores of rocks above those that were saturated with iron hydroxide, precipitated manganese hydroxides and, locally, iron and manganese carbonates, and mixed with freshwater to produce the Lower Mn-1 ore layer, which contains clastic–chemical diagenetic ore. The excess manganese that remained in solution was deposited in the basin depocenter, forming the Upper Mn-1 ore layer, which is also enriched in P, Co, Ni, and Cu, in the Figueirinha and São Domingos mines, simultaneously with the influx of clay and silt that were deposited by turbidity currents.
5. Each time the bottom of the Urucum graben collapsed, the hydrothermal emissions and turbidite flows increased, making the water turbid and producing high concentrations of silica and Fe(II). The basin became deeper and stratified, with cloud-oxidized water near the surface and sub-oxidized below the oxycline. These flooding episodes reduced the ocean water supply, with microorganisms facilitating microbial Fe(II) anoxic/anaerobic and neutrophilic (photomanganotroph) metabolism that was driven by UV radiation, thus causing the biogenic-mediated oxidation of Fe(II), forming ferrihydrites above the oxycline (Fig. 18E), and producing chemical, abiotic Fe precipitation from water saturation. The sedimentation of clay-rich ferrihydrites without chemical silica covered the basin floor before the manganese sedimentation, forming Fe-rich muds below the massive manganese layers. After diagenesis, this ferruginous mud was transformed into massive, laminated IFs and ferruginous siltstones, on which Mn-2 and Mn-3 were deposited (Fig. 7).
6. The Mn-2 and Mn-3 layers, which only contain manganese, settled during quiescence between episodes of collapse within the Urucum graben, when the hydrothermal emissions ceased. The sedimentation of manganese was mediated by microorganisms when the water layer was shallow and devoid of hydrothermal Fe(II) and silica and when the environment became oxidizing, which hindered the sedimentation of iron and silica. The biomass was a suboxic-anoxic mud that formed with residues of chemolithotrophic bacteria, and the Fe(II) within the water of this mud precipitated as ferrihydrites. Thus, layers Mn-2 and Mn-3 were originally biomass muds that consisted of manganese, few iron hydroxides and carbonate.
7. Each massive Mn-2 and Mn-3 manganese layer formed over at least four stages:
   a. The Urucum Basin was flooded by water that was abundant in chemoautotrophic microbes, which transformed Mn(II) to $Mn(OH)_4$ under oxidizing conditions and formed microorganism colonies that grew in oblate, concentric structures, thereby forming kremydilites. Under suboxic conditions, Mn (and minor Mg) carbonate was formed, Fe(II) was transformed into $Fe(OH)_3$ and CH_4 and H_2 were generated inside the kremydilites below the oxycline (Fig. 18G) forming internodular and/or intergranular bubbles that subsequently left the structures and migrated laterally and upward through the porous sediment that was saturated with seawater. Residues of these bacteria generated a biomass layer, which contained carbonates and was permeated by water that was saturated in $Mn(OH)_4$ + $Fe(OH)_4$, on the basin floor (carbonate mud that contained little SiO_2 and abundant carbon, Fe, Mn, P, and Co). The biotic nucleation of these hydroxides prevented silica precipitation. The presence of carbonate crystals and carbonate micro-structures (micro-needles, mesh-structures and micro-nodules) in the current pores of kremydilites suggests that originally kremydilites may have been composed mainly of carbonate, practically all of them replaced by oxides during diagenesis.
   b. During early diagenesis, wormlike microorganisms inhabited the biomass. These organisms separated $Mn(OH)_4$ from $Fe(OH)_4$, excreted rhodochrosite microbialites, and crystallized Mn–Fe carbonates as roughly rounded microstructures. The microbialite coalescence generated millimeter-scale cryptomelane ± hollandite micronodules. Seemingly, the manganese micronodule nucleation process occurred simultaneously with the crystallization of rhodochrosite, hausmannite, bixbyite, and subordinate amounts of Al and Mn phosphates (eosphorite and crandallite).
   c. The micronodules coalesced, forming massive cryptomelane micronodule layers with minor hematite and resulting in layers of massive manganese oxides ± minor hematite and manganese carbonates.
   d. Early diagenesis expelled most of the water and oxidized the remaining $Mn(OH)_4$, converting it to cryptomelane ± bixbyite ± hausmannite and thereby generating massive cryptomelane ore. Late diagenesis began with the abiotic substitution of biomass with manganese oxide (± Fe oxide?) and the transformation of cryptomelane to hollandite.
8. The sedimentation of Mn-2 and Mn-3 was interrupted by sandy turbiditic flows and avalanches. These events allowed the sedimentation of ferruginous arkosic muds and conglomerates with a ferruginous arkosic matrix.
9. BIF and IF sedimentation, which occurred simultaneously with the precipitation of carbonate rocks at the edge of the basin, was interrupted only by the deposition of layers Mn-2 and Mn-3 and continued until the tectonic inversion that caused the inversion of the basin.
10. The chemical Mn- and Fe-rich sedimentary rocks that formed the Santa Cruz Formation were probably deposited at approximately 543 Ma, during the Ediacaran–Cambrian transition, approximately 90 Ma after the end of the Cryogenian and Marinoan glaciations and 37 Ma after the Gaskiers glacial period. Therefore, iron and manganese were precipitated without the influence of glaciations.

Acknowledgements

We thank Cia VALE Urucum for providing access to their mines of Urucum region (MS) and the important logistical assistance given

during every time. The first author thank, particularly, to Geologist José Braga Neto, from Cia VALE, for the attention and the assistance provided during all field works. This research did not receive any specific grant from funding agencies in the public, commercial, or not-for-profit sectors.

References

Almeida, F.F.M., 1946, Origem dos minérios de ferro e manganês de Urucum (Corumbá, Estado do Mato Grosso): Boletim da Divisão de Geologia e Mineralogia do Departamento Nacional da Produção Mineral (DNPM, Rio de Janeiro), 119, p. 58.

Alvarenga, C.J.S., Trompete, R., 1994. A Faixa Paraguai e sua compartimentação estratigráfica e tectônicca. XXXVIII Congresso Brasileiro de Geologia (Camboriu). Boletim de Resumos Expandidos, pp. 229–230.

Angerer, T., Hagemann, S.G., Walde, D.H.G., Halverson, G.P., Boyce, A.J., 2016. Multiple metal source in glaciomarine facies of the Neoproterozoic Jacadigo iron formation in the "Santa Cruz deposit", Corumbá, Brazil. Precambr. Res. 275, 369–393.

Babinski, M., Boggiani, P.C., Fanning, C.M., Fairchild, T.R., Simon, C.M., Sial, A.N., 2008. U–Pb SHRIMP geochronology and isotope chemostratigraphy (C, O, S) of the Tamengo formation, Southern Paraguay Belt, Brazil: South American Symposyum on Isotope Geology, 6th, San Carlos de Bariloche (Argentina), p. 160.

Baele, J.M., Bouvain, F., De Jong, J., Matielli, N., Papier, S., Prat, A., 2008. Iron microbial mats in modern and Phanerozoic environments. Proceedings of SPIE – The International Society for Optical Engineering, 7097, 70970N-70970N-12. doi: 10.1117/12.801597.

Bargar, J.R., Tebo, B.M., Bergmann, U., Webb, S.M., Glatzel, P., Chiu, V.Q., Villalobos, M., 2005. Biotic and abiotic products of Mn(II) oxidation by spores of the marine Bacillus sp. strain SG-1. Am. Mineral. 90, 143–154.

Bau, M., Dulski, P., 1996. Distribution of yttrium and rare-earth elements in the Pengeand Kuruman iron-formations, Transvaal Supergroup, South Africa. Precambr. Res. 79 (1–2), 37–55.

Bau, M., Dulski, P., 1999. Camparing yttrium and rare earths in hydrothermal fluids from the Mid-Atlantic Ridge: implications for Y and REE behavior during near-vent mixing and for the Y/Ho ratio of Proterozoic seawater. Chem. Geol. 155 (1–2), 77–90.

Bau, M., Möller, P., 1993. Rare earth element systematics of the chemically precipitated component in early precambrian iron formations and the evolution of the terrestrial atmosphere-hydrosphere-lithosphere system. Geochim. Cosmochim. Acta 57 (10), 2239–2249.

Bau, M., Möller, P., Dulski, P., 1997. Yttrium and lanthanides in eastern Mediter-ranean seawater and their fractionation during redox-cycling. Mar. Chem. 56 (1), 123–131.

Bengtson, S., 2002. Origins and early evolution of predation. Paleontol. Soc. Papers 8, 289–317.

Beukes, N.J., 1983. Paleoenvironmental setting of iron formations in the depositional basin of the Transvaal Supergroup, South Africa. In: Trendall, A.F., Morris, R.C., (eds.), Iron Formations: Facts and Problems, Elsevier, Amsterdam, pp. 131–209.

Beukes, N.J., Burger, A.M., Gutzmer, J., 1995. Fault-controlled hydrothermal alteration of Palaeoproterozoic manganese ore in Wessels mine, Kalahari manganese field. South Afr. J. Geol. 98, 430–451.

Beukes, N.J., Gutzmer, J., 2008. Origin and Paleoenvironmental Significance of Major Iron Formations at the Archean-Paleoproterozoic Boundary: SEG Reviews, vol. 15, pp. 5–47. Chapter 1, Society of Economic Geologists.

Beurlen, K., Sommer, F.W., 1957. Observações estratigráficas e paleontológicas sobre o calcário Corumbá: Boletim da Divisão de Geologia e Mineralogia. Departamento Nacional da Produção Mineral 168, 1–35.

Biondi, J.C., Santos, R.V., Cury, L.F., 2011. The paleoproterozoic aripuanã Zn–Pb–Ag (Au, Cu) volcanogenic massive sulfide deposit, Mato Grosso, Brazil: geology, geochemistry of alteration, carbon and oxygen isotope modeling and implications for genesis. Econ. Geol. 108, 781–811.

Bjerrum, C.J., Canfield, D.E., 2002. Ocean productivity before about 1.9 Gyr ago limited by phosphorous adsorption onto iron oxides. Nature 717, 159–162.

Bodeï, S., Manceau, A., Geoffroy, N., Baronnet, A., Buatier, M., 2008. Formation of todorokite from vernadite in Ni-rich hemipelagic sediments. Geochim. Cosmochim. Acta 71 (23), 5698–5716.

Bodor, S., Polgári, M., Szentpétery, I., Földessy, J., 2016. Microbially mediated iron ore formation, Silicic Superunit, Rudabánya, Hungary. Ore Geol. Rev. 72 (P1), 391–401.

Boggs Jr., S., 2012. Principles of Sedimentology and Stratigraphy, 5th Ed. Pearson Education Limited, Essex, England, pp. 553.

Bolhar, R., Van Kranendonk, M.J., 2007. A non-marine depositional setting for the northern Fortescue Group, Pilbara Craton, inferred from trace element geochemistry of stromatolitic carbonates. Precambr. Res. 155 (3–4), 229–250.

Boggiani, P.C., Gaucher, C., Sial, A.N., Babinski, M., Simon, C.M., Riccomini, C., Ferreira, V.P., Fairchild, T.R., 2010. Chemostratigraphy of the Tamengo Formation (Corumbá Group, Brazil) – a contribution to the calibration of the Ediacarancarbon-isotope curve. Precambr. Res. 182, 382–401.

Cairncross, B., Beukes, N.J., 2013. The Kalahari Manganese Field. Struik Nature, Cape Town, South Africa, pp. 383.

Chen, D., Qing, H., Yan, X., Li, H., 2006. Hydrothermal venting and basin evolution (Devonian, China) – Constraints from rare earth element geochemistry of chert. Sed. Geol. 183, 203–216.

Cloud, P.E., 1973. Paleoecological significance of the banded iron formation. Econ. Geol. 68, 1135–1143.

Costa M.L., Fernandez, O.J.C., Ribeiro, P.A., Silva, N.C., Poellmann, H., 2005. Contribuições mineralógicas e geoquímicas sobre a origem do minério de manganês do Morro do Urucum (Corumbá, Brasil): Simpósio Brasileiro de Metalogenia, 1th, Gramado (RS, Brasil), Abstracts, CDROM.

Dardenne, M.A., 1998. Modelo hidrotermal exalativo para os depósitos de Fe-Mn da região de corumbá, Mato Grosso do Sul: Congresso Brasileiro de Geologia, 40th, São Paulo, Brasil, Abstracts, p. 158.

Danielson, A., Möller, P., Dulski, P., 1992. The europium anomalies in banded iron formations and the thermal history of the oceanic crust. Chem. Geol. 97 (1–2), 89–100.

Dean, W.E., Arthur, M.A., Claypool, G.E., 1986. Depletion of ^{13}C in cretaceous marine organic matter: source, diagenetic, or environmental signal? Mar. Geol. 70 (1–2), 119–157. http://dx.doi.org/10.1016/0025-3227(86)90092-7.

D'el-Rey Silva, L.J.H., Walde, D.H.G., Saldanha, D.O., 2016. The Neoproterozoic-Cambrian Paraguay Belt, central Brazil: Part I—New structural data and a new approach on the regional implications. Tectonophysics 676, 20–41.

Derry, L.A., Jacobsen, S.B., 1990. The chemical evolution of Precambrian seawater – Evidence from REEs in banded iron formations. Geochim. Cosmochim. Acta 54, 2965–2977.

Door, J.V.N., 1945. Manganese and iron deposits fo Morro do Urucum, Mato Grosso, Brazil. U. S. Geol. Surv. Bull. 946A, 47.

Drever, J.I., 1974. Geochemical model for the origin of Precambrian banded iron formations. Geol. Soc. Am. Bull. 85, 1099–1106.

Dubinin, A.V., 2004. Geochemistry of rare earth elements. Lithol. Min. Resour. 39, 289–307.

Dulski, P., 1994. Interferences of oxide, hydroxide and chloride analyte species in the determination of rare earth elements in geological samples by inductively coupled plasma mass spectrometry. Fresenius J. Anal. Chem. 350, 194–203.

Dupraz, S., Parmentier, M., Ménez, B., Guyot, F., 2009. Experimental and numerical modeling of bacterially induced pH increase and calcite precipitation in saline aquifers. Chem. Geol. 265, 44–53.

Dymek, R.F., Klein, C., 1988. Chemistry, petrology and origin of banded iron-formation lithologies from the 3800 MA Isua supracrustal belt, West Greenland. Precambr. Res. 39 (4), 247–302.

Eastoe, C.J., Nelson, S.E., 1988. A Permian kuroko-type hydrothermal system – Afterthought-Ingot area, Shasta county, California – Lateral and vertical sections and geochemical evolution. Econ. Geol. 83, 588–603.

Ehrlich, H.L., 1990. Geomicrobiology, second ed., M. Dekker, New York, N.Y., p. 719.

Evans, R., 1894. The geology of Mato Grosso, particularly the region drained by upper Paraguay. Geol. Soc. Lond. Q. J. 50, 85–104.

Freitas, B.T., Warren, L.V., Boggiani, P.C., Paes de Almeida, R., Piacentini, T., 2011. Tectono-sedimentary evolution of the Neoproterozoic BIF-bearing Jacadigo Group, SW Brazil. Sediment. Geol. 238, 48–70.

Gaucher, C., Boggiani, P.C., Sprechmann, P., Sial, P., Fairchild, T.R., 2003. Integrated correlation on Vendian to Cambrian Arroyo del Soldado and Corumbá Groups, Bolivia and Brazil – Paleogeographic, paleoclimatic and paleobiologic implications. Precambr. Res. 120, 241–278.

German, C.R., Elderfield, H., 1990a. Application of the Ce anomaly as a paleoredox indicator – The ground rules. Paleoceanography 5, 823–833.

German, C.R., Elderfield, H., 1990b. Rare earth elements in the NW Indian Ocean. Geochim. Cosmochim. Acta 54, 1929–1940.

German, C.R., Masuzawa, T., Greaves, M.J., Elderfield, H., Edmond, J.M., 1995. Dissolved rare earth elements in the Southern Ocean – Cerium oxidation and the influence of hydrography. Geochim. Cosmochim. Acta 59, 1551–1558.

Germs, G.J.B., 1972. New shelly fossil from Nama Group, South West Africa. Am. J. Sci. 272, 752–761.

Graf, J.L., O'Connor, E.A., Leeuwen, P.V., 1994. Rare earth element evidence of origin and depositional environment of late Proterozoic ironstone beds and manganese ore deposits, SW Brazil and SE Bolivia. J. South Am. Earth Sci. 7, 115–133.

Grant, S.W.F., 1990. Shell structure and distribution of Cloudina, a potential index fossil for the terminal Proterozoic. Am. J. Sci. 290, 261–294.

Gromet, L.P., Dymek, R.F., Haskin, L.A., Korotev, R.L., 1984. The "North American shale composite": its compilation, major and trace element characteristics. Geochim. Cosmochim. Acta 48, 2469–2482.

Grotzinzer, J.P., Bowring, S.A., Saylor, B.Z., Kaufman, A.J., 1995. Biostratigraphic and geochronology constraints on early animal evolution. Science 270, 598–604.

Gutzmer, J., Beukes, N.J., 1995. Fault-controlled metasomatic alteration of early oterozoic sedimentary manganese ores in the Kalahari manganese field, South Africa. Econ. Geol. 90, 823–844.

Gutzmer, J., Beukes, N.J., 1996. Mineral paragenesis of the Kalahari manganese field, South Africa. Ore Geol. Rev. 11, 405–428.

Halverson, G.P., Poitrasson, F., Hoffman, P.F., Kirby, L.J.K., 2011. Fe isotope and trace element geochemistry of the Neoproterozoic syn-glacial Rapitan iron formation. Earth Planet. Sci. Lett. 309 (1–2), 100–112.

Hahn, G., Hahn, R., Leonardos, O.H., Pflug, H.D., Walde, D.H.G., 1982. Körperlich erhaltene Scyphozoen-Reste aus dem Jungpräkambrium Brasiliens. Geol. Paleontol. (Marburg) 16, 1–18.

Haralyi, N.L.E., 1972. Novos dados sobre a geologia da região de Corumbá (MT): Congresso da Sociedade Brasileira de Geociências, 26th, Rio de Janeiro, Abstracts, p. 101.

Haralyi, N.L.E., Wald, D.H.G., 1986. Os minerais de ferro e manganês da região de Urucum, Mato Grosso do Sul. In: In: Schobenhaus, C., Coelho, C.E.S. (Eds.), Principais Depósitos Minerais do Brasil, vol. 2. Departamento Nacional da Produção Mineral, Brasilia, Brazil, pp. 127–144.

Hasui, Y., Almeida, F.F.M., 1970. Geocronologia do Centro-Oeste brasileiro. Boletim Soc. Bras. Geol. (São Paulo) 19 (1), 5–26.

Hedges, J.I., Mann, D.C., 1979. The lignin geochemistry of marine sediments from the southern Washington coast. Geochim. Cosmochim. Acta 43, 1809–1818.

Herdianita, N.R., Browne, P.R.L., Rodgers, K.A., Campbell, K.A., 2000. Mineralogical and

textural changes accompanying ageing of silica sinter. Miner. Deposita 35, 48–62.
Hoefs, J., Frey, M., 1976. The isotopic composition of carbonaceous matter in a metamorphic profile from the Swiss Alp. Geochim. Cosmochim. Acta 40, 945–951.
Hofmann, H.J., Mountjoy, E.W., 2001. Namacalathus-Cloudina assemblage in Neoproterozoic Miette Group (Byng Formation), British Columbia – Canada oldest shelly fossil. Geology 29 (12), 1091–1094.
Hoffman, P.F., Schrag, D.P., 2002. The snowball Earth hypothesis – Testing the limits of global change. Terra Nova 14, 129–155.
Jarvis, K.E., Gray, A.L., McCurdy, E., 1989. Avoidance of spectral interference on europium in inductively coupled plasma mass spectrometry by sensitive measurement of the doubly charged ion. J. Anal. Atmos. Spectrom. 4, 743–747. http://dx.doi.org/10.1039/JA9890400743.
Jiao, Y., Kappler, A., Croal, L.R., Newman, D.K., 2005. Isolation and characterization of a genetically tractable photoautotrophic Fe(II)-oxidizing bacterium, *Rhodopseudomonas palustris* strain TIE-1. Appl. Environ. Microbiol. 71, 4487–4496.
Kappler, A., Pasquero, C., Konhauser, K.O., Newman, D.K., 2005. Deposition of banded iron formations by phototrophic Fe(II)-oxidizing bacteria. Geology 33, 865–868.
Kaufman, A.J., Knoll, A.H., 1995. Neoproterozoic variations in the C-isotopic composition of seawater: stratigraphic and biogeochemical implications. Precambr. Res. 73, 27–49.
Kimberley, M.M., 1989. Exhalative origins of iron formations. Ore Geol. Rev. 5, 13–145.
Klein, C., Ladeira, E.A., 2004. Geochemistry and mineralogy of Neoproterozoic banded iron-formations and some selected, siliceous manganese formations form the Urucum district, Mato Grosso do Sul, Brazil. Econ. Geol. 99, 1233–1244.
Konhauser, K.O., 1998. Diveristy of bacterial iron mineralization. Earth Sci. Rev. 43, 91–121.
Konhauser, K.O., Newman, D.K., Kappler, A., 2005. The potential significance of microbial Fe(III) reduction during deposition of Precambrian banded iron formations. Geomicrobiology 3, 167–177.
Konhauser, K.O., Amskold, L., Lalonde, S.V., Posth, N.R., Kappler, A., Anbar, A., 2007. Decoupling photochemical Fe(II) oxidation from shallow-water deposition. Earth Planet. Sci. Lett. 258, 87–100.
Kowalick, J., Rye, R.O., Sawkins, F.J., 1981. Stable-isotope study of the Buchans, Newfoundland, polymetallic deposits. Geol. Soc. Canada Spec. Paper 22, 229–254.
Krumbein, W.E., 1983. Stromatolites — the challenge of a term in space and time. Precambr. Res. 20 (2–4), 493–531.
Kump, L.R., Junium, C., Arthur, M.A., Brasier, A., 2011. Isotopic evidence for massive oxidation of organic matter following the great oxidation event. Science 334 (6063), 23.
Large, R.R., Both, R.A., 1980. The volcanogenic ores at Mount Chalmers, Eastern Queensland. Econ. Geol. 75, 992–1009.
Large, R.R., Bull, S.W., Maslennikov, V.V., 2011. A carbonaceous sedimentary source-rock model for carlin-type and orogenic gold deposits. Econ. Geol. 106, 331–358.
van Leeuwen, P., Graaf, J.L., 1987. The Urucum-Mutum iron and manganese deposits, Mato Grosso do Sul, Brazil, and Santa Cruz, Bolivia. Part 1-The region's potential as an economic source of iron and manganese. Geol. Mijnbouw 65, 317–325.
Leonardos, O.H., Walde, D.H.G., 1982. Sobre a estratigrafia e a gênese dos depósitos de manganês a luz do vulcanismo Jacadigo: Congresso da Sociedade Brasileira de Geociências, 27th, Salvador, Abstracts, p. 203.
Litherland, M., et al., 1989. The Proterozoic of Eastern Bolivia and its relationship to the Andean mobile belt. Precambr. Res. 43 (3), 157–174.
Lovley, D.R., 1991. Dissimilatory Fe(III) and Mn(IV) reduction. Microbiol. Rev. 55 (2), 259–287.
MacLean, W.H., Hoy, L.D., 1991. Geochemistry of hydrothermally altered rocks of the Horne Mine, Quebec. Econ. Geol. 86, 506–528.
Meister, P., Bernasconi, S.M., Aiello, I.W., Vasconcelos, C.G., Mckenzie, J.A., 2009. Depth and controls of Ca-rhodochrosite precipitation in bioturbated sediments of the Eastern Equatorial Pacific, ODP Leg 201, Site 1226 and DSDP Leg 68, Site 503. Sedimentology 56, 1552–1568.
Michard, A., 1989. Rare earth elements systematics in hydrothermal fluids. Geochin. Cosmochim. Acta 53 (3), 745–750.
Michard, A., Albarede, F., Michard, G., Minster, J.F., Charlou, J.L., 1983. Rare-earth elements and uranium in high-temperature solutions from East Pacific Rise hydrothermal vent field (13 N). Nature 303, 795–797.
Miyano, T., Beukes, N.J., 1987. Physicochemical environments for the formation of quartz-free manganese oxide ores from the Early Proterozoic Hotazel Formation, Kalahari manganese field, South Africa. Econ. Geol. 82, 706–718.
Moffett, J.W., Ho, J., 1996. Oxidation of cobalt and manganese in seawater via a common microbially catalyzed pathway. Geochim. Cosmochim. Acta 60 (18), 3415–3424.
Molnár, Z., Polgári, M., Hein, J.R., Józsa, S., Fekete, J., Gyollai, I., Fintor, K., Bíró, L., Szabó, M., Rapi, S., Forgó, P., Vigh, T., 2017. Fe–Mn oxide indications in the feeder and mound zone of the Jurassic Mn-carbonate ore deposit, Úrkút, Hungary. Ore Geol. Rev. 86, 839–855.
Morgan, J.J., 2005. Kinetics of reaction between O_2 and Mn(II) species in aqueous solutions. Geochim. Cosmochim. Acta 69 (1), 35–48.
Murray, R.W., 1994. Chemical criteria to identify the depositional environment of chert – general principles and applications. Sed. Geol. 90, 213–232.
Murray, R.W., Buchholtz ten Brink, M., Jones, D.L., Gearlach, D.C., Price Russ III, G., 1990. Rare earth elements as indicators of different marine environments in chert and shale. Geology 18 (3), 268–271.
Myers, R.C., Nealson, R.K.H., 1988. Bacterial manganese reduction and growth with manganese oxide as the sole electron acceptor. Science 240, 1319–1321.
Nealson, K.H., Myers, C.R., 1992. Microbial reduction of manganese and iron – New approaches to carbon cycling. Appl. Environ. Microbiol. 58, 439–443.
Nealson, K.H., Saffarini, D., 1994. Iron and manganese in anaerobic respiration – Environmental significance, physiology and regulation. Annu. Rev. Microbiol. 48, 311–343.
O'Connor, E.A., Walde, D.H.G., 1985. Recognition of an Eocambrian orogenic cycle in SW Brazil and Bolivia: Zbl. Geol. Paläontol. 1, 1441–1456.
Ohmoto, H., et al., 2006. Chemical and biological evolution of early Earth: constraints from banded iron-formations. In: Kesler, S., Ohmoto, H. (Eds.), Evolution of the Atmosphere, Hydrosphere, and Biosphere on Early Earth: Constraints from Ore Deposits, vol. 196, Geological Society America Memoires, pp. 291–331.
Okita, P.M., Maynard, J.B., Spiker, E.C., Force, E.R., 1988. Isotopic evidence for organic matter oxidation by manganese reduction in the formation of stratiform manganese carbonate ore. Geochim. Cosmochim. Acta 52, 2679–2685.
Owen, R.M., Olivarez, A.M., 1988. Geochemistry of rare earth elements in Pacific hydrothermal sediments. Mar. Chem. 25, 183–196.
Park Jr., C.F., Dorr II., J.V.N., Guild, P.W., Barbosa, A.L.M., 1951. Notes on the manganese ores of Brazil. Econ. Geol. 46, 1–22.
Piacentini, T., Vasconcelos, P.M., Farley, K.A., 2013. $^{40}Ar/^{39}Ar$ constraints on the age and thermal history of the Urucum Neoproterozoic banded-iron formation, Brazil. Precambr. Res. 228, 48–62.
Planavsky, N., et al., 2010. Rare earth element and yttrium compositions of archean and paleoproterozoic Fe formations revisited: new perspectives on the significance and mechanisms of deposition. Geochim. Cosmochim. Acta 74 (22), 6387–6405.
Polgári, M., Hein, J.R., Tóth, A.L., Pál-Molnar, E., Vigh, T., Biró, L., Fintor, K., 2012a. Microbial action formed Jurassic Mn-carbonate ore deposit in only a few hundred years (Ùrkut, Hungary). Geology 40, 903–906.
Polgári, M., Hein, J.R., Vigh, T., Szabó-Drubina, M.M., Fórizs, I., Bíró, L., Müller, A., Tóth, A.L., 2012b. Microbial processes and the origin of the Úrkút manganes deposit, Hungary. Rev. 47, 87–109.
Posth, N.R., Hegler, F., Konhauser, K.O., Kappler, A., 2008. Alternating Si and Fe deposition caused by temperature fluctuations in Precambrian oceans. Nat. Geosci. 1, 703–708.
Posth, N.R., Köhler, I., Swanner, E.D., Schröder, Wellmann, E., Binder, B., Konhauser, K.O., Neumann, U., Berthold, C., Nowak, M., Kappler, A., 2013. Simulating Precambrian banded iron formation diagenesis. Chem. Geol. 362, 66–73.
Putzer, H., 1958. Die Kryptomelan- und Jaspelit-Lagerstätten von Corumbá im Staate Mato Grosso, Brasilien: Erzmet all, 11, 527–538.
Rajabzadeh, M.A., Haddad, F., Polgári, M., Fintor, K., Walter, H., Molnár, Z., Gyollai, I., 2017. Investigation on the role of microorganisms in manganese mineralization from Abadeh-Tashk area, Fars Province, southwestern Iran by using petrographic and geochemical data. Ore Geol. Rev. 80, 229–249.
Redes, L.A., Sousa, M.Z.A.D., Ruiz, A.S., Lafon, J.M., 2015. Petrogenesis and U-Pb and Sm-Nd geochronology of the Taquaral granite: record of an Orosirian continental magmatic arc in the region of Corumbá – MS. Braz. J. Geol. 45 (3), 431–451.
Ruhlin, D.E., Owen, R.M., 1986. The rare earth element geochemistry of hydrothermal sediments from the East Pacific Rise – Examination of a seawater scavenging mechanism. Geochim. Cosmochim. Acta 50, 393–400.
Schneider, G., 1984. Zur Mineralogie and Lagerstättenbildung der Mangan- und Eisenerzvorkommen de Urucum Distriktes (Mato Grosso, Brasilien): Frankfurter Geowiss. Arb. Serie C 1, (Frankfurt), p. 205.
Schobbenhaus, C., Campos, D.A., Derze, G.R., Asmus, H.E., 1981. Mapa geológico do Brasil e da área oceânica adjacente incluindo depósitos minerais. Escala1/2.500.000. Departamento Nacional da Producão Mineral (D.N.P.M.), Brasilia.
Schopf, T.J.M., 1974. Permo-Triassic extinction – Relation to sea-floor spreading. J. Geol. 82, 129–183.
Schreck, P., 1984. Geochemische Klassifikation und Petrogenese der Manganerze des Urucum Distriktes bei Corumbá (Mato Grosso do Sul, Brasilien): Frankfurter Geowiss. Arb. Serie C 1, (Frankfurt), p. 206.
Sholkovits, E.R., Landing, W.M., Lewis, B.L., 1994. Ocean particle chemistry – the fraction of rare earth elements between suspended particles and seawater. Geochim. Cosmochim. Acta 58 (6), 1567–1579.
Tebo, B.M., Ghiorse, W.C., Van Waasbergen, I.G., Siering, P.L., Caspi, R., 1997. Bacterially mediated mineral formation: insights into manganese (II) oxidation from molecular genetic and biochemical studies. In: In: Banfield, J.F., Nealson, K.H. (Eds.), Geomicrobiology: Interactions Between Microbes and Minerals, vol. 35. Reviews in Mineralogy, Mineralogical Society of America, Washington, D.C., pp. 448.
Tebo, B.M., Bargar, J.R., Clement, B., Dick, G., Murray, K.J., Parker, D., Verity, R., Webb, S., 2004. Manganese biooxide: properties and mechanisms of formation. Ann. Rev. Earth Planet. Sci. 32, 287–328.
Trompette, R., Alvarenga, C.J.S., Walde, D.H.G., 1998. Geological evolution of the Neoproterozoic Corumbá graben system (Brazil) – Depositional context of the stratified Fe and Mn of the Jacadigo Group. J. S. Am. Earth Sci. 11, 587–597.
Tsikos, H., Moore, J.M., 1997. Petrography and geochemistry of the Paleoproterozoic Hotazel iron formation, Kalahari Manganese Field, South Africa: implications for Precambrian manganese metallogenesis. Econ. Geol. 92, 87–97.
Tsikos, H., Beukes, N.J., Moore, J.M., Harris, C., 2003. Deposition, diagenesis, and secondary enrichment of metals in the Paleoproterozoic Hotazel Iron Formation, Kalahari Manganese Field, South Africa. Econ. Geol. 98, 1449–1462.
Urban, H., Stribrny, B., Lippolt, H., 1992. Iron and manganese deposits of the Urucum district, Mato Grosso do Sul, Brazil. Econ. Geol. 87, 1375–1392.
Villalobos, M., Toner, B., Bargar, J., Sposito, G., 2003. Characterization of the manganese oxide produced by Pseudomonas putida MnB1. Geochim. Cosmochim. Acta 67, 2649–2662.
Zaine, M.F., Fairchild, T.R., 1985. Comparison of *Aulophycus luacinoi*, Beurlen & Sommer, from Ladario (MS) and the genus Cloudina, Germs, Ediacaran of Namibia. Anais da Academia Brasileira de Ciências 57, 130.
Zaw, K., Large, R.R., 1992. The precious metal-rich South Hercules mineralization, western Tasmania: a possible sea-floor replacement volcanic-hosted massive sulfide deposit. Econ. Geol. 87, 931–952.

Walde, D.H.G., 1981. Die Mangan- und Eisenvorkommen von Urucum, Mato Grosso, Brasilien: Erste Ergebnisse und ein weiteres Program, Zbl. Geol. Paläontol. 1, 505–513.

Walde, D.H.G., 1988. Das proterozoische Paraguay-Araguaia Orogen in West-Brasilien, Ausgehend von Untersuchungen im Raum Corumbá: Habilitationsscrift, Albert Ludwigs Universität, Freiburg, p. 122 (unpublished).

Walde, D.H.G., Gierth, E., Leonardos, O.H., 1981. Stratigraph and mineralogy of the manganese ores of Urucum, Mato Grosso, Brazil. Geol. Rundschau 70, 1077–1085.

Walde, D., Hagemann, S.G., 2007. The Neoproterozoic Urucum/Mutún Fe and Mn deposits in W-Brazil/SE-Bolivia: assessment of ore deposit models. Z. dt. Ges. Geowiss 158 (1), 45–55.

Webb, S., Dick, G.J., Bargar, J.R., Tebo, B.M., 2005. Evidence for the presence of Mn (III) intermediates in the bacterial oxidation of Mn(II). Microbiology 102, 5558–5563.